Non-gaussian spin states of ultracold dysprosium atoms

Alexandre Evrard

PSL
UNIVERSITÉ PARIS

THÈSE DE DOCTORAT
DE L'UNIVERSITÉ PSL

Préparée à l'École Normale Supérieure

Non-Gaussian Spin States of Ultracold Dysprosium Atoms

Soutenue par
Alexandre EVRARD
Le 29 septembre 2020

Ecole doctorale n° 564
Physique en Île-de-France

Spécialité
Physique Atomique et Moléculaire Optique

Composition du jury :

Christophe MORA Université Paris-Diderot	*Président*
Monika SCHLEIER-SMITH Stanford University	*Rapporteur*
Christoph WESTBROOK Laboratoire Charles Fabry de l'Institut d'Optique	*Rapporteur*
Sylvain NASCIMBENE École Normale Supérieure	*Directeur de thèse*

ENS | PSL

Laboratoire Kastler Brossel
Physique quantique et applications

COLLÈGE DE FRANCE
1530

Remerciements

C'est une page qui se tourne après trois ans et demi (n'oublions pas le stage de M2 !) passés dans ce cadre privilégié qu'est le Collège de France. Je me considère comme extrêmement chanceux d'avoir pu travailler dans ce lieu prestigieux, sous la direction d'excellents chercheurs et en compagnie de collègues formidables.

Je tiens tout d'abord à remercier Jean de m'avoir accueilli au sein de son équipe. Je me souviens à quel point j'étais impressionné, ayant déjà auparavant assisté à ton cours au Collège de France, au moment de mon 'entretien d'embauche' dans ton bureau en présence de Sylvain, Jérôme et Fabrice.

Sylvain, je pense que tu es le directeur que tout thésard rêverait d'avoir. Toujours disponible pour répondre aux questions, à la fois très clairvoyant au niveau de la physique et d'une grande humilité. Même si ton sens de l'humour ne se dévoile que peu au labo, je garde de très bons souvenirs de nos interactions en dehors du travail et en particulier de notre partie épique de babyfoot aux Houches !

Merci Raphael pour ton dynamisme et le temps passé au labo. Ton expérience sur les aspects techniques et tes réponses à mes questions m'ont toujours été d'une grande utilité. Ça a toujours été un plaisir de discuter musique avec toi en salle de manip. Bonne chance pour ton futur de chercheur. Je ne te souhaite pas bon courage car je sais que tu n'en manques pas.

J'ai toujours été frappé par la bonne ambiance qu'il y avait dans le groupe par rapport aux échos que j'ai pu avoir sur d'autres équipes. Je pense que cela tient autant aux bons moments passés ensemble le midi, à la pause café, à la pause croissants et aux verres bus ensemble, qu'à la bonne humeur de chacun.

Je commencerai par remercier Thomas, qui m'a tout appris ou presque sur la manip, le plus souvent en écoutant Pink Floyd, comme il se doit. Queen c'est bien aussi. Par contre Kraftwerk c'est mort. Je garde de très bons souvenirs du temps passé ensemble au labo. Thanks Vasiliy for the good time spent together. Tanish c'est maintenant toi le thésard senior, c'est dingue comme ça passe vite ... Ça a été un honneur d'aligner le transverse cooling avec toi. Salut Aurélien ! Je tiens à saluer ta bonne humeur permanente et je suis rassuré de savoir que le salut de la manip repose sur toi. Enfin je te souhaite bonne chance J-B, les gros changements sur la manip prévus dans un futur proche sont assez excitants vus de l'extérieur mais ne seront probablement pas si simples à mettre en place !

Merci Merlin pour les cafés, quelle que soit la tasse utilisée, selon l'humeur. Tu peux continuer à utiliser la cafetière pendant les quelques mois qu'il te reste, cafetière dont je fais d'ailleurs don aux futurs thésards qui comme nous n'aiment

pas la cafetière moka. Sauront-ils presser le café suffisamment lentement pour éviter les fuites ? Seul l'avenir le dira. Bravo Bertrand pour ton titre de docteur ! Tu l'as amplement mérité. Ça a toujours été insolite d'avoir un homonyme dans le groupe.

Bon courage Alexis pour la fin de thèse. Ta capacité à répondre aux questions du Trivial Pursuit est tout simplement bluffante ! Du courage c'est surtout à Rémy qu'il va en falloir, mais je ne doute pas que tu t'en sortiras. C'est également à toi que revient la tâche de perpétuer la tradition, que dis-je, le culte du sandwich libanais. Manel tu en étais le prophète mais les choses n'ont plus été les mêmes après ton départ. Nul doute que Rémy saura maintenir la coutume. Longue vie à Manel II le grand.

Merci beaucoup Edouard pour l'ambiance que tu as su insuffler au groupe. Faire de la bière du vendredi une habitude aura été une très bonne chose. Un big merci à Brice pour sa joie de vivre communicative et sa générosité de tous les instants. Merci à Chloé qui a apporté du sang neuf dans le groupe, j'ai hâte de voir si tu réussiras à avoir un jury de thèse entièrement féminin. Quant à Guillaume je ne doute pas que tu es déjà très bien intégré à ton équipe et j'attends avec impatience le moment où tu trouveras le courage (ou la témérité) de défier Jérôme à la course à pied.

Grâce à vous tous notre étage a toujours été un lieu chaleureux et agréable à vivre, et avec ses murs d'un blanc uniforme et froid, c'était pas gagné !

Merci à toutes les personnes avec qui j'ai pu écumer les salles d'escalade parisiennes. Merci au groupe des 'alpinistes' pour m'avoir trainé en extérieur, purée d'purée ! Merci à Cyril pour son humour et son enthousiasme. Je remercie tout particulièrement Tim pour avoir toujours été égal à lui-même. Ça fait déjà six ans qu'on se marre à propos des mêmes trucs ! Thank you dude.

Merci au groupe de potes du lycée, collège et même avant pour certains ! Il faut qu'on se fasse une petite belote d'urgence ! Et je parle vraiment du jeu de carte.

Merci à Daphné et Nicolas pour leur présence et leur soutien dans les bons moments comme dans les moins bons. Vous m'avez beaucoup apporté et je pense pouvoir dire que sans vous je ne serais pas le même.

Enfin un très grand merci à mes parents à qui je dois énormément. Votre fierté signifie beaucoup pour moi.

Bonne lecture à celles et ceux qui ne s'arrêteront à la fin de cette page !

Alex

Abstract

This thesis manuscript presents experiments realized with ultracold atomic gases of dysprosium. This chemical element has specific properties such as a large spin $J = 8$ and tunable light-spin couplings originating from significant tensor light-shift contributions close to resonance.

An overview of the experimental setup is given, from the magneto-optical trap with a Doppler temperature limit on the order of a few μK to the last stage of evaporative cooling. In particular we present the in-trap Doppler cooling step showing the effect of the tensor light-shift on the atom trapping. Details on the use of spatial modulation to tune the shape of an optical dipole trap are also given.

In the second part we detail the manipulation of spin states obtained from ultracold atomic clouds. Light-induced spin squeezing is realized and used to prepare squeezed and 'oversqueezed' states as well as Schrödinger cat states. The magnetic sensitivity of these states is characterized using Ramsey spectroscopy. We provide a reconstruction of the Husimi function of the different states deduced from population measurements along various directions. These measurements also allow us to compute the purity of the prepared states.

While spin squeezing initially induces an increase of metrological gain, we observe a strong contrast reduction of the Ramsey oscillations for oversqueezed states obtained from the squeezing evolution at longer times. We introduce the Hellinger distance between two states which can be used to generalize the notion of metrological gain. The sensitivity is measured using this method and we show that it saturates the Cramér-Rao bound. The Husimi and Wigner functions of an oversqueezed state are experimentally measured and constitute to some extent a visualization of the Majorana stellar representation of a spin J as a sum of $2J$ spins 1/2. Finally this analogy is used to study a system of 16 interacting indistinguishable spins 1/2.

In the third part we present a proposal of a project that was not realized experimentally but could be performed in the future on our setup. It consists in measuring pairwise entanglement of spin states from photon absorption measurements, showing the intrinsic difference between multipartite entanglement and reduced pairwise entanglement.

We also introduce two projects that can be viewed as the addition of spatial degrees of freedom to light-induced spin squeezing. The first one consists in the realization of a system analogous to the Landau Hamiltonian of a charged particle in a magnetic field, with one spatial dimension and one synthetic dimension using the internal state of the atoms. The second project uses two spatial dimensions and exhibits an artificial magnetic field originating from position-dependent light-shifts.

Résumé

Ce manuscrit de thèse est consacré à des expériences réalisées à partir de gaz d'atomes de dysprosium ultrafroids. Cet élément chimique possède des propriétés physiques particulières comme un grand moment angulaire $J = 8$ ou bien une composante tensorielle du déplacement lumineux significative à proximité de résonance.

Nous donnons tout d'abord un aperçu du dispositif expérimental, depuis l'étape de piégeage magnéto-optique jusqu'au refroidissement par évaporation. La modulation spatiale permettant de contrôler la forme d'un piège optique est détaillée, ainsi que le rôle du déplacement lumineux tensoriel dans l'étape de refroidissement Doppler dans un piège optique.

La seconde partie est dédiée à la préparation d'états de spin à partir de nuages froids. La partie tensorielle du déplacement lumineux est utilisée pour préparer des états comprimés et 'surcomprimés' ainsi que des états chats de Schrödinger. La sensibilité magnétique de ces états est mesurée à l'aide de séquences de Ramsey et permet de calculer le gain métrologique. La fonction de Husimi est reconstruite expérimentalement à partir de mesures de population dans différentes directions, ce qui permet aussi de déterminer la pureté des états préparés.

Les états comprimés ont effectivement une sensibilité accrue, mais on observe pour les états surcomprimés une forte diminution du contraste des oscillations de Ramsey. L'utilisation de la distance de Hellinger permet de quantifier la différence entre deux états proches et ainsi donner une nouvelle définition du gain métrologique. Dans ce contexte la limite de Cramér-Rao est atteinte et la sensibilité des états surcomprimés est supérieure à celle des états comprimés. Les fonctions de Husimi et Wigner pour un état surcomprimé rendent visible la représentation stellaire de Majorana qui consiste à représenter l'état d'un spin J par $2J$ points sur la sphère, équivalents à des spins 1/2. Cette analogie nous permet de réaliser un système de 16 spins 1/2 indistinguables en interaction.

Dans une troisième partie nous nous intéressons à un projet qui n'a pas été réalisé en pratique. L'idée est de mesurer l'intrication de paire pour les états d'un spin J à l'aide de probabilités d'absorption de photons. La différence de nature entre l'intrication multipartite et l'intrication de paire est ainsi rendue manifeste.

En conclusion sont présentés deux projets qui consistent en l'ajout de degrés de libertés externes à la dynamique des degrés de liberté internes. Dans le premier cas est réalisé un système analogue à l'Hamiltonien de Landau pour une particule chargée dans un champ magnétique, avec une dimension d'espace et une dimension synthétique. Dans le second cas, deux dimensions d'espace sont utilisées et la présence d'un déplacement lumineux dépendant de la position réalise un champ magnétique artificiel.

Contents

Acronyms

MOT	Magneto-Optical Trap
AOM	Acousto-Optic modulator
ODT	Optical Dipole Trap
cODT	crossed Optical Dipole Trap
BEC	Bose-Einstein Condensate
PSD	Phase Space Density
CSS	Coherent Spin State
SQL	Standard Quantum Limit
OAT	One-Axis Twisting
LMGm	Lipkin-Meshov-Glick model
RWA	Rotating Wave Approximation

Introduction

Cold atoms physics

The term *quantum* mechanics was introduced for the first time in 1924 by M. Born [1], this word being based on the notion of 'quanta' invented by M. Planck in 1900 [2]. This theory based on a limited set of (sometimes counter-intuitive) assumptions proved to be very powerful at describing the interactions between atoms and electromagnetic fields at the microscopic level. Over the course of the 20th century, new discoveries were accompanied by technical advances such as the first maser in 1953 [3] and then the development of lasers which has been of extreme importance in technological breakthroughs.

In particular, the advent of laser led to the development of the cold atom community which has had a major impact in the scientific community. This field of research was recognized with the Nobel prize of Physics attributed to S. Chu, C. Cohen-Tannoudji and W. Phillips in 1997 for the development of methods to cool and trap atoms with laser light. It was soon followed by the observation of the first gaseous Bose-Einstein condensate [4, 5] in 1995 which led to the attribution of the 2001 Physics Nobel prize to E. Cornell, C. Wieman and W. Ketterle in 2001.

These developments opened the door for high-precision quantum metrology, notably frequency/time sensing with atomic clocks. The uncertainty achieved with these devices went down from a value of 10^{-10} in the 1960s based on a hyperfine transition of cesium to 2×10^{-18} for the most recent optical clocks [6], developed in the group of J. Ye.

Secondly, the ability to trap and cool atoms, as well as the high degree of precision and control of these systems allowed for a new approach to understanding complicated systems : *quantum simulation*, an idea attributed to Richard Feynman [7]. It consists in experimentally realizing a theoretical model that cannot be solved analytically or numerically in order to get an insight of the physical effects at play. It is especially useful in the case of many-body interacting systems where classical computers cannot keep up with the high degree of complexity. Cold atoms prove to be a convenient toolbox to realize such systems thanks to a variety of tunable parameters [8]. In particular the physics of the BEC-BCS crossover involving interacting fermions in the unitary regime was successfully studied with cold atoms [9, 10]. A key goal in condensed-matter physics is the understanding of the physics of high-T_c superconductors and whether or not it is well described by the Fermi-Hubbard model [11]. The experimental study of this model and its phase diagram with cold atoms [12] constitutes a step in this direction. In a general way artificial gauge fields are a powerful tool to realize theoretical models of condensed-matter physics with cold atoms [13], especially for systems where topological properties are

expected [14].

Thirdly a general goal in cold atoms is the realization of exotic phases of matter that are not necessarily found in any 'natural' system, with striking features such as supersolidity, which is precisely one of the focus of ultracold dysprosium experiments as mentioned in the following section.

Dysprosium experiments

The first historical realizations of atom trapping and cooling were performed with alkali elements, as their electronic structure is relatively simple, with one electron on the outer shell, leading to exploitable cycling transitions. In particular rubidium is the most commonly used atomic species in cold atoms experiments due to its convenience in terms of the wavelengths used and favorable atom-atom interactions.

Lanthanides have attracted the interest of the community in recent years because of their more complex electronic structure, leading to interesting atom-light couplings and for most of them large atomic magnetic moment. Erbium was first laser-cooled in 2008 by the team of J. McClelland (NIST Gaithersburg) [15] and dysprosium in 2010 by the team of B. Lev (Stanford) [16]. This triggered the creation of several dysprosium experiments such as in the groups of T. Pfau (Stuttgart) [17] and G. Modugno (Pisa) [18], the dysprosium-potassium and erbium-dysprosium experiments in the groups of R. Grimm and F. Ferlaino (Innsbuck) [19, 20], as well as ours (S. Nascimbene, Paris) [21]. This recent trend towards building cold atoms dysprosium experiments was referred to as “dysprosium is the new rubidium” by R. Grimm during a seminar, since it could become a common standard in the future in the same way rubidium is.

Other groups mainly focused on the study of dipole-dipole interactions in quantum gases [22], leading to striking features such as the observation of the Rosensweig instability and the formation of stable quantum droplets [23], with a quantum liquid behaviour [24]. The roton minimum was also observed [25] in systems exhibiting supersolid behaviour [26–28]. On the other hand our team was more interested in the phenomena related to the large spin of dysprosium, such as the preparation of non-gaussian spin states using light-induced quadratic spin couplings. We also took advantage of the large number of internal states to realize a synthetic Hall system analogous to the Landau Hamiltonian of a charged particle in a magnetic field, one dimension of space being simulated by the internal state of the atom.

In this manuscript we are interested in non-classical spin states prepared with ultracold atoms of dysprosium and we study their magnetic field sensitivity. Our goal is not to realize a practical sensor in terms of size, interrogation time, working range, etc. but rather to demonstrate the intrinsic metrological interest of such spin states, which could potentially be used in other situations. As for real magnetic sensors, the most successful systems do not come from the field of cold atoms but rather solid-state physics. Devices such as SQUIDs [29] based on Josephson junctions are well-known and the less common SERF technique exhibits a sensitivity below 1 $\mathrm{fT}/\sqrt{\mathrm{Hz}}$ [30].

Chronology and publications

The experiment I worked on during my PhD is a machine designed to produce cold atomic clouds of Dysprosium and during three years I worked on several projects using these clouds to address quite a wide range of physical phenomena. The experiment was already functional when I joined the team in October 2017 even though cooling down to quantum degeneracy had not been achieved yet. The main project at this time was the realization of Schrödinger-cat states using non-linear light-spin couplings as it did not require Bose-Einstein condensates but only cold thermal clouds. We were working with ^{164}Dy at that time. In 2018 we implemented in-trap Doppler cooling techniques to pursue the goal of quantum degeneracy. We also changed isotope for ^{162}Dy and were able to produce a Bose-Einstein condensate in July 2018.

We continued to use non-linear spin couplings to produce oversqueezed states and studied their magnetic field sensitivity in October 2018, followed by the study of the Lipkin-Meshkov-Glick model in March 2019. The focus of the team then shifted towards the realization of topological systems using artificial gauge fields.

I list below the publications related to the projects I was involved in during my time in the group.

- *Quantum-enhanced sensing using non-classical spin states of a highly magnetic atom*
  T. Chalopin, C. Bouazza, A. Evrard, V. Makhalov, D. Dreon, J. Dalibard, L. A. Sidorenkov, and S. Nascimbene
  Nat. Commun. **9**, 1-8 (2018).

- *Anisotropic lightshift and magic-polarization of the intercombination line of dysprosium atoms in a far-detuned dipole trap*
  T. Chalopin, V. Makhalov, C. Bouazza, A. Evrard, A. Barker, M. Lepers, J.-F. Wyart, O. Dulieu, J. Dalibard, R. Lopes, and S. Nascimbene
  Phys. Rev. A **98**, 040502 (2018).

- *Enhanced magnetic sensitivity with non-gaussian quantum fluctuations*
  A. Evrard, V. Makhalov, T. Chalopin, L. A. Sidorenkov, J. Dalibard, R. Lopes, and S. Nascimbene
  Phys. Rev. Lett. **122**, 173601 (2019).

- *Probing quantum criticality and symmetry breaking at the microscopic level*
  V. Makhalov, T. Satoor, A. Evrard, T. Chalopin, R. Lopes, and S. Nascimbene
  Phys. Rev. Lett. **123**, 120601 (2019).

- *Probing chiral edge dynamics and bulk topology of a synthetic Hall system*
  T. Chalopin, T. Satoor, A. Evrard, V. Makhalov, J. Dalibard, R. Lopes, and S. Nascimbene
  Nature Phys (2020).

Outline and content of the chapters

This manuscript is divided in three parts. The first one consists in a general presentation of the specific properties of dysprosium and of the experimental setup.

The second part focuses on experimental results concerning non-gaussian spin states and their enhanced magnetic field sensitivity. Finally the third part deals with other projects related to pair entanglement and artificial gauge fields, adding spatial degrees of freedom to the large-spin features of dysprosium.

Chapter 1 gives an overview of the experimental setup used to produce cold atomic clouds. We present some properties of dysprosium and their use in the experimental scheme. Details are given about in-trap Doppler cooling performed after the atoms are transported to the glass cell.

Chapter 2 is a description of the spatial modulation of optical dipole traps implemented on the experiment, allowing for a better starting point (in terms of atom number and temperature) of the evaporative cooling procedure.

Chapter 3 starts with a general presentation of spin states and their representation on the Bloch sphere. The notion of coherent spin state is introduced, as well as the one-axis twisting hamiltonian used in the preparation of squeezed spin states or Schrödinger-cat states. The metrological gain is defined in the context of Ramsey spectroscopy. Finally the experimental preparation of these states is described and their sensitivity is measured.

Chapter 4 begins with general concepts of parameter estimation theory and the introduction of the Cramér-Rao bound, which can be saturated with a well-chosen observable in specific cases. The notion of metrological gain is extended further than its definition based on Ramsey oscillations thanks to the Hellinger distance. In particular it allows for the characterization of oversqueezed states which exhibit a better sensitivity than squeezed states. It is followed by a brief presentation of the experimental realization of the Lipkin-Meshkov-Glick model (for 16 spins 1/2).

Chapter 5 is a proposal for a project that has not been experimentally realized yet. It consists in the measurement of the pairwise entanglement of states of a spin J, characterized by a quantity called the concurrence, via photon absorption probability.

Chapter 6 presents an extension of the ideas and tools introduced in chapter 4 to couple spatial degrees of freedom to the internal spin state of dysprosium atoms. It constitutes an experimental realization of a topological system, equivalent to the Landau Hamiltonian of a charged particle in a magnetic field. Finally a second project that is currently investigated in the group is briefly presented, also dealing with artificial gauge fields.

Part I

Production of ultracold dysprosium gases

Chapter 1

Overview of the experiment

This chapter provides a description of some properties of dysprosium and how they are involved in the optical cooling techniques used in the experimental apparatus. We use atomic transitions and laser cooling schemes which have been developed in the group of T.Pfau [17] in 2014.

1.1 Properties of dysprosium

There are seven stable isotopes of dysprosium among which five are relatively abundant in nature. They are listed in table 1.1 along with some of their properties. The work presented in this manuscript only deals with bosonic ^{162}Dy, except for the data taken from [31] which uses ^{164}Dy. This choice is motivated by the value of the background s-wave scattering length, which facilitates the evaporative cooling procedure. Apart from isotopic shifts in the atomic transitions, ^{164}Dy is fairly similar except for a slightly lower background scattering length. ^{160}Dy is much less abundant which makes large atomic samples difficult to obtain. This isotope has been Bose-condensed with a scattering length value tuned by a nearby Feschbach resonance but a background scattering length value could not be extracted [32].

Isotope	^{160}Dy	^{161}Dy	^{162}Dy	^{163}Dy	^{164}Dy
Abundance	2.34 %	18.9 %	25.5 %	24.9 %	28.2 %
Statistics	Boson	Fermion	Boson	Fermion	Boson
s-wave scattering length [a_0]			140(7)		69(4)

Table 1.1 – Different isotopes of Dy and relevant properties. Scattering lengths are expressed in units of the Bohr radius $a_0 = 4\pi\hbar^2/(m_e e^2)$. Their values are taken from [33] for ^{162}Dy and [34] for ^{164}Dy.

There is no nuclear spin I for bosonic isotopes of dysprosium and therefore no hyperfine structure. Its electronic structure can be written

$$[\mathrm{Xe}]4f^{10}6s^2 \tag{1.1}$$

which corresponds to the situation of a *submerged shell*. This means that even though the $6s$ shell is filled with two electrons, the 'previous' $4f$ shell has only 10 electrons (out of 14). Its filling is indicated on figure 1.1 in which the four

unpaired electrons lead to an orbital angular momentum $L = 6$ and an electronic spin $S = 2$. The ground state of dysprosium corresponds to the case of a total angular momentum $J = L + S = 8$.

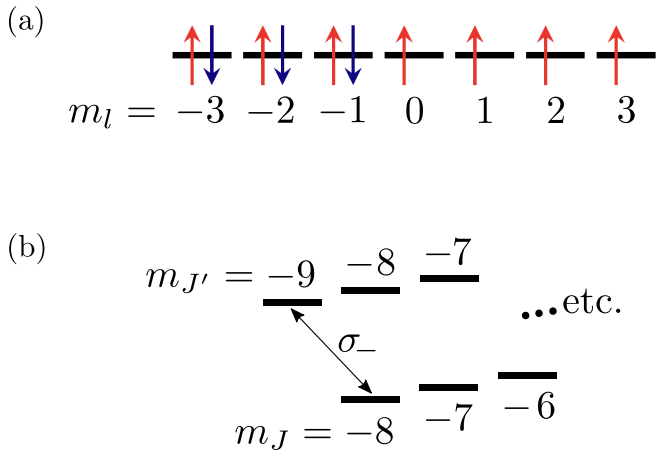

Figure 1.1 – (a) Electronic filling of the inner $4f$ shell giving $L = 6$ and $S = 2$. **(b) $J \to J+1$ cycling transition**. This situation corresponds to a positive Landé g factor for both the ground and excited manifolds. The Zeeman shift between the different m_J states is induced by a positive magnetic field as is the case on the experiment.

The large angular momentum in the ground state leads to accessible magnetic sublevels $m_J = -8$ to $m_J = 8$ and a large magnetic dipole moment $\mu = m_J g_J \mu_B = 9.93\,\mu_B$ in the ground state. This value can be compared to the ones of Erbium ($6.98\,\mu_B$) and chromium ($6\,\mu_B$ [35]), the two other elements that have been used to study dipolar quantum gases.

The large angular momentum also leads to a large number of electronic transitions plotted on figure 1.2 among which a few stand out. First we need to mention the $J = 8$ to $J' = 9$ transitions i.e. the cycling optical transitions relevant for laser cooling (figure 1.1). We use two such transitions at $\lambda = 421$ nm and $\lambda = 626$ nm which will be referred to in the following as the *blue* and *red* transitions.

The blue transition at 421 nm corresponds to an excitation of one of the outer shell electrons to a singlet state $6s^2(^1S_0) \to 6s6p(^1P_1)$ and is quite favorable, with a large width Γ. The line at 626 nm corresponds to the partially forbidden transition to the triplet state $6s6p(^3P_1)$ and is therefore much more narrow.

Most of the transitions plotted on figure 1.2 correspond to excitations of the $4f^{10}$ shell electrons and are thus typically two orders of magnitude narrower than the blue one. The consequence of this strong difference between the transition probabilities will be visible in the following section.

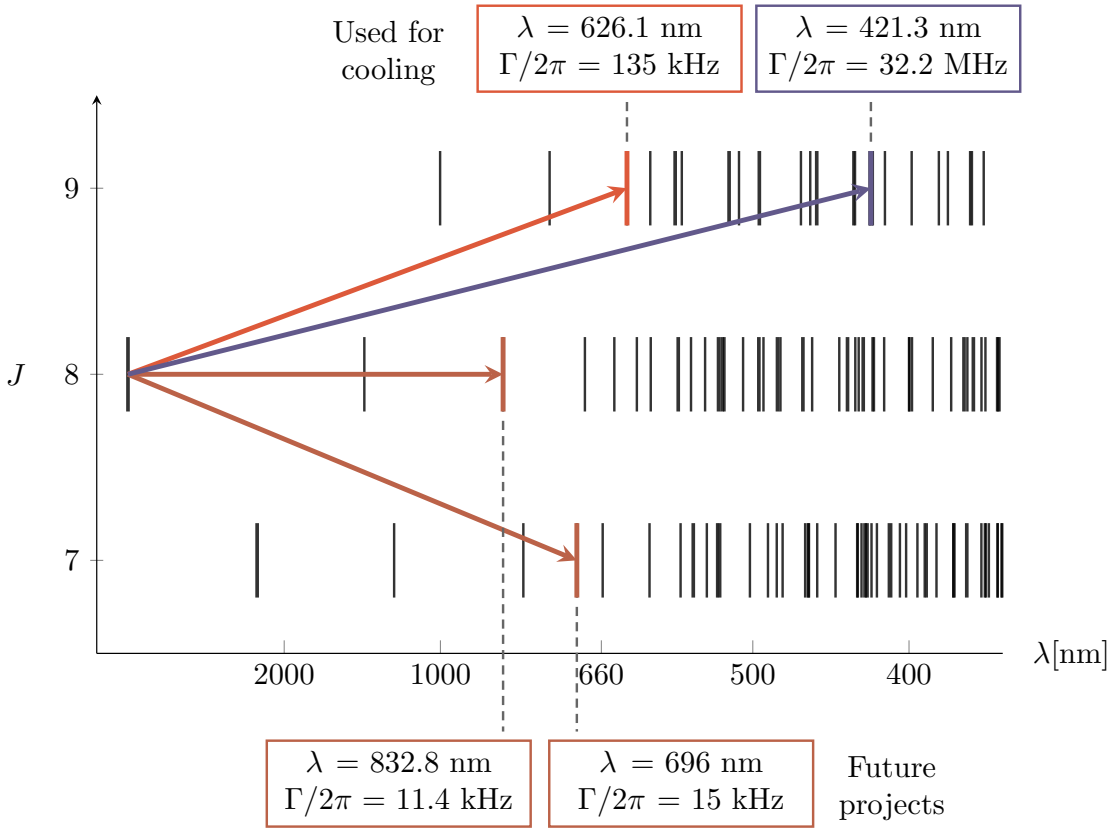

Figure 1.2 – Energy levels of Dysprosium. Only the levels corresponding to transitions $J' = 7, 8, 9$ are shown as the others cannot be excited by a photon from the ground state $J = 8$. The two transitions used on the experiment for cooling ($J' = 9$) are highlighted, as well as two other transitions ($J' = 8$ and $J' = 7$) involved in future projects as described in part III.

1.2 Atom-light coupling

As mentioned in the introduction, dysprosium is especially suited for spin squeezing. The reason is that it is relatively easy to induce quadratic spin couplings with light [36], which is the basic mechanism leading to squeezing and the preparation of other non-classical spin states [37]. The derivation of the light-shift operator has been detailed in the thesis of D. Dreon [38], and this version is similar to [39].

We write the coupling to an electric field $\boldsymbol{E}$ of frequency ω as

$$-\hat{\boldsymbol{d}} \cdot \boldsymbol{E} = -\frac{1}{2} E\, \hat{\boldsymbol{d}} \cdot \boldsymbol{u}\, e^{-i\omega t} - \frac{1}{2} E^*\, \hat{\boldsymbol{d}} \cdot \boldsymbol{u}^*\, e^{i\omega t} \tag{1.2}$$

where $\hat{\boldsymbol{d}}$ is the atomic dipole operator. Using time-dependent second order perturbation theory, one obtains the energy shift of a given level $|a\rangle$ from

$$\delta E_a = -\frac{|E|^2}{4\hbar} \sum_b \mathrm{Re}\left(\frac{|\langle b|\hat{\boldsymbol{d}} \cdot \boldsymbol{u}|a\rangle|^2}{\omega_b - \omega_a - \omega - i\gamma_{ba}/2} + \frac{|\langle b|\hat{\boldsymbol{d}} \cdot \boldsymbol{u}^*|a\rangle|^2}{\omega_b - \omega_a + \omega + i\gamma_{ba}/2} \right) \tag{1.3}$$

where the sum runs over all states $|b\rangle$ (with energy $\hbar\omega_b$) different from $|a\rangle$ (energy $\hbar\omega_a$). The term $\gamma_{ba} = \gamma_a + \gamma_b$ is the sum of their width.

The energy shift δE_a can be written as the expectation value $\langle a|\hat{V}|a\rangle$ of the operator

$$\hat{V} = \frac{|E|^2}{4}\left((\hat{\boldsymbol{d}}\cdot\boldsymbol{u}^*)\mathcal{R}_+(\hat{\boldsymbol{d}}\cdot\boldsymbol{u}) + (\hat{\boldsymbol{d}}\cdot\boldsymbol{u})\mathcal{R}_-(\hat{\boldsymbol{d}}\cdot\boldsymbol{u}^*)\right) \tag{1.4}$$

where

$$\mathcal{R}_\pm = -\frac{1}{\hbar}\sum_b \mathrm{Re}\left(\frac{1}{\omega_b - \omega_a \mp (\omega + i\gamma_{ba}/2)}\right)|b\rangle\langle b| \tag{1.5}$$

Then we assume that not only the energy shift δE_a but the entire physics of the various possible couplings is described by $\hat{V}$. This assumption is not obvious but is consistent with the Floquet formalism that is not detailed here.

One can see from the expression of $\hat{V}$ that it is a tensor operator of rank 2 (because $\hat{\boldsymbol{d}}$ is a rank 1 tensor operator (i.e. a vector operator) and $\boldsymbol{u}$ a vector). It can be decomposed as a sum of three irreducible tensors of respective rank 0, 1 and 2 as

$$\hat{V} = \hat{V}_s + \hat{V}_v + \hat{V}_t \tag{1.6}$$

which are called the scalar, vector and tensor light shifts. In the end we decompose $\hat{V}$ as a sum of the contribution of each transition $J \to J'$ to the scalar, vector and tensor parts as $\hat{V} = \sum_{J'} \hat{V}_{JJ'}$ where we can write $\hat{V}_{JJ'}$ in terms of angular momentum operators $\hat{J}$ as

$$\hat{V}_{JJ'} = -\frac{|E|^2}{4}\left[\alpha^s_{JJ'}\mathbb{1} - i\alpha^v_{JJ'}\frac{(\boldsymbol{u}^*\times\boldsymbol{u})\cdot\hat{\boldsymbol{J}}}{2J} + \alpha^t_{JJ'}\frac{3[(\boldsymbol{u}^*\cdot\hat{\boldsymbol{J}})(\boldsymbol{u}\cdot\hat{\boldsymbol{J}}) + (\boldsymbol{u}\cdot\hat{\boldsymbol{J}})(\boldsymbol{u}^*\cdot\hat{\boldsymbol{J}})] - 2\hat{\boldsymbol{J}}^2}{2J(2J-1)}\right]. \tag{1.7}$$

The $\alpha^{s,v,t}_{JJ'}$ are respectively called the scalar, vector and tensor polarizabilities. They contain the frequency dependence of the coupling (with the usual lorentzian width) and depend on the Clebsch-Gordan algebra of the spins J and J'. Their full expression is given in appendix A. The real part of $\hat{V}$ corresponds to the coupling strength while its imaginary part corresponds to the photon scattering rate. The full landscape of the polarizabilities as a function of the light wavelength λ is plotted on figure 1.3. It corresponds to the sum of the contributions of the transitions $J \to J'$ for $J' = J-1$, J and $J+1$. The transition data correspond to values taken from [40]. Note that not all levels are used and the most narrow ones may have been omitted. In particular the transitions at 696 nm and 832.8 nm mentioned on figure 1.2 are not present. More detailed data are given in [41]. In practice we are either far from any resonance when using optical dipole traps in which case the scalar part dominates (figure 1.3), or almost resonant with a given transition (figure 1.4).

We provide a zoom of the three parts of the polarizability around the red transition at 626 nm on figure 1.4. We are able to induce quadratic spin couplings by

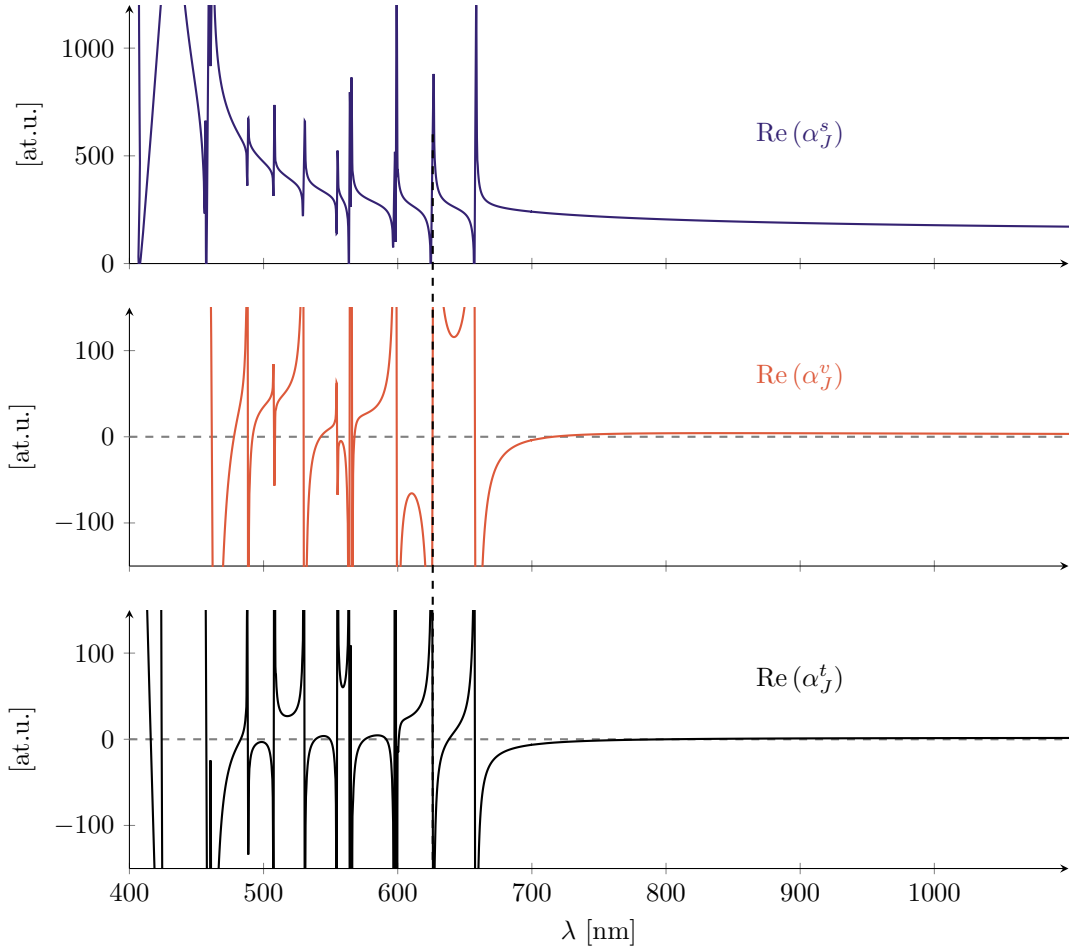

Figure 1.3 – Real part of the three terms of the polarizability. Apart from the narrow transitions, the broad line at 421 nm, as well as two other lines at 405 and 419, set the global trend for the scalar term. However these transitions have no contribution to the vector or tensor parts, which remain close to zero away from any sharp resonance. The vertical dashed line corresponds to the 626 nm transition. The atomic unit of polarizability at.u. corresponds to $1\,\text{at.u.} = 4\pi\epsilon_0 a_0^3$ where a_0 is the Bohr radius.

working close to this transition. Related experiments and results are presented in chapter 3 and 4. Using the same resonance for Doppler cooling in the MOT stage and quadratic spin-couplings is a choice based on the physical characteristics of the resonance (value of the polarizability, small width and $J' = 9$). It is also motivated by the fact that it is generally not simple to produce light at a desired wavelength. Since the setup for the MOT beams at 626 nm had already been built, it was more straightforward to assemble a twin setup for the spin coupling light.

While blue light at 421 nm is produced by a commercial laser, the production of red light at 626 nm requires a more complex sum-frequency-generation described in details in previous thesis manuscripts [38] and [42].

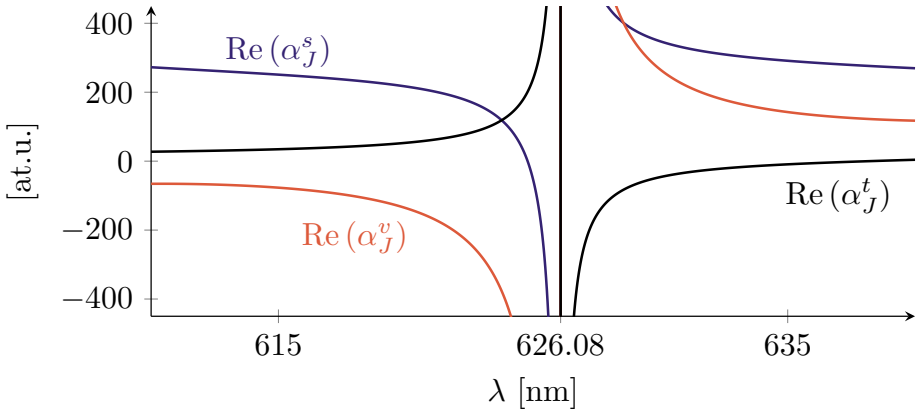

Figure 1.4 – Zoom on the 626 nm transition. A narrow resonance typically spans over a few nanometers. The scalar polarizability is then the sum of the background value mostly given by the broad resonance in the blue and the local contribution around the narrow resonance at 626 nm. The overall trend is given by the resonance used rather than the effect of the broad blue one. The vector and tensor parts become comparable to the scalar part close to resonance.

1.3 Magneto-optical trapping and atomic transport

The experiment consists in several stages used to obtain a dilute atomic gas in the ultracold temperature regime, starting from a sample of solid metallic dysprosium. The whole experiment is under ultra-high vacuum as interactions with the environment would prevent any atom trapping and/or cooling. Indeed collisions with residual gas particles cause the atoms to leave the trap and lead to a certain lifetime for the atomic cloud. Since we hold atoms for times of several seconds during the total experimental cycle, we need a background-limited lifetime on the order of at least 10 seconds. This sets a constraint on the value of the pressure to typically 10^{-10} mbar, obtained with ionic and getter pumps.

In fact the pressure is not the same in the different parts of the experiment owing to differential pumping. The pressure is so low that the regime is *ballistic* and the pressure does not equilibrate between the different parts as it would intuitively because the probability for the remaining particles to find their way to the other part is simply too low. The Zeeman slower geometry consists in a tube with a length of 50 cm and internal diameter 1 cm which induces differential pumping between the oven part and the MOT chamber. It maintains a pressure difference of one order of magnitude , with respective pressures of around 10^{-9} mbar for the oven and below 10^{-10} mbar for the science cell (lowest value that the probes can measure).

1.3.1 Oven

The starting point is an oven used to heat up solid samples of dysprosium so that its vapour pressure exceeds the actual pressure inside the experiment. The typical working temperature is around 1100 °C and results in an effusive flow of dysprosium atoms, that we refer to in the following as *atomic beam*.

The oven parts are made of tantalum to withstand very high temperatures (sev-

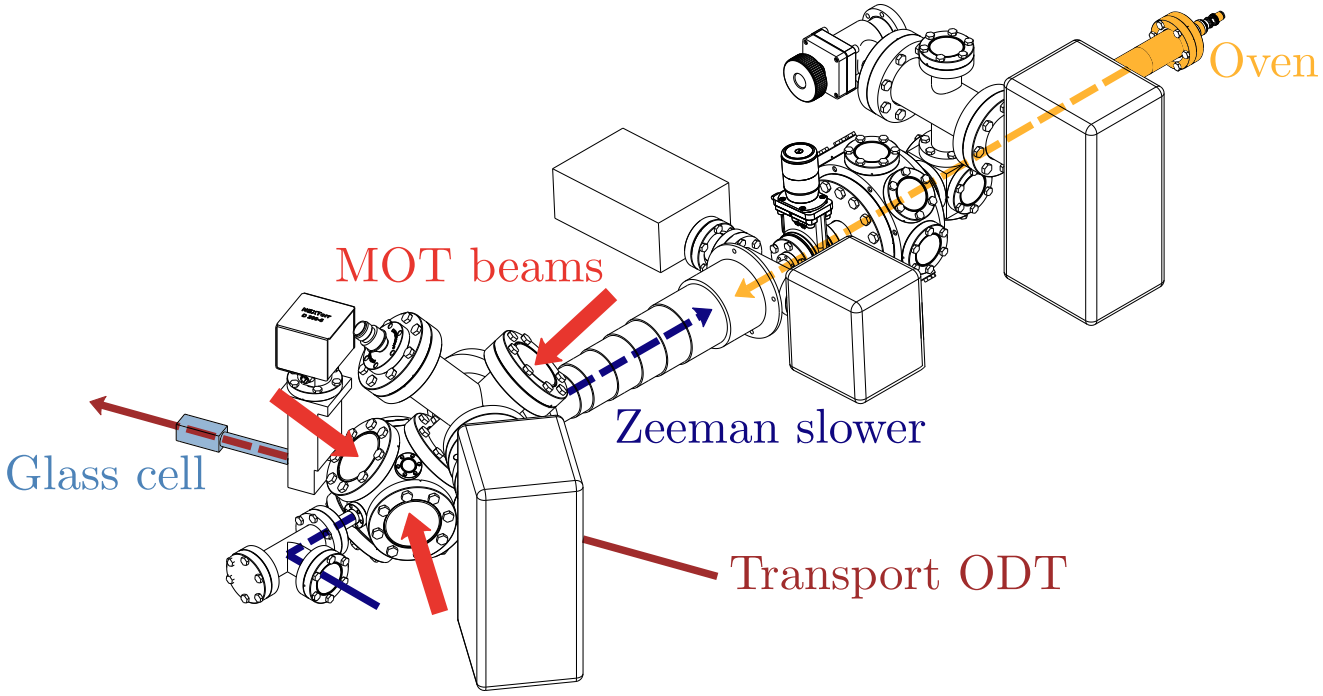

Figure 1.5 – Scheme of the experiment with the main elements. The Zeeman slower beam (blue arrow) counter propagates with respect to the atomic beam (yellow arrow) to slow it down. Three of the six MOT beams (red arrows) are represented. Finally the transport ODT (dark red arrow) brings the atoms to the glass cell.

eral thousands of Celsius degrees). It consists in a crucible in which up to 15 grams of dysprosium are loaded in the form of 1 mm granules. Electrical current passing through a set of wires surrounding the crucible induce heating. The external part of the oven is water cooled and only warm to the touch. The crucible has to be refilled every three to six months. This implies partially breaking the vacuum to open the oven, a valve being used to preserve the rest of the experiment. Repumping of the oven part after the refill takes up to one week.

1.3.2 Zeeman slowing and Magneto-optical trapping

A blocking piece with a $\sim$ 1 cm hole placed after the oven ensures that the atomic beam is narrower and aligned with the axis of the Zeeman slower. The atoms initially propagate with an axial velocity distribution $P(v)$ peaked around 460 m/s. A counter-propagating resonant laser beam is used to slow down the atoms enough so that they can be trapped. Its working principle relies on the interplay between the Doppler effect and the Zeeman effect. Note that the laser beam is sent through a window with a 90° angle with respect to the atomic beam (figure 1.5). This is designed such that the window does not get covered in dysprosium and does not become opaque over time. The mirror placed inside vacuum gets covered in dysprosium but still reflects light, although with additional diffusion slowly building up over the years. This is not yet an issue after 7 years of operation and the Zeeman

beam is still well collimated.

An atom is initially moving fast when it enters the Zeeman slower tube, and therefore the light has to be detuned from resonance by a quantity Δ to account for the corresponding Doppler shift. As the atom starts absorbing and reemiting photons it slows down and gets out of resonance. A space-dependent magnetic field is used so that its Zeeman shift compensates the Doppler shift of the slowing atom and maintains it at resonance with the light along the trajectory, as the atom slows all the way down to 8 m/s in our case. The magnetic field profile $B(x)$ is determined by the chosen local detuning $\delta(x)$ at position x, according to

$$\delta(x) = \Delta \underbrace{- k\, v(x)}_{\text{Doppler}} + \underbrace{\mu_B \frac{g_{J'} m_{J'} - g_J m_J}{\hbar} B(x)}_{\text{Zeeman}} \tag{1.8}$$

Choosing $\delta(x) = 0$ over the entire trajectory ensures maximal absorption probability at all times. We use the blue transition with σ_- polarized light to take advantage of a large transition width to slow down a broader range of velocity classes present in the atomic beam.

Then the atoms are attracted to the center of the magneto-optical trap (MOT) formed by 3 orthogonal pairs of counter-propagating beams and a vertical magnetic field gradient. The magnetic field value can be set along all three directions using coils of a few meters of diameter placed in Helmholtz configuration. A smaller additional pair of coils placed around the MOT chamber sets the field gradient. The red transition is used for its narrow linewidth resulting in a lower Doppler limit $T_{\min} = \hbar\Gamma/2k_B \simeq 3$ µK. The narrow transition leads to a small capture velocity $v \lesssim 5$ m/s which is a limiting factor. There are two ways to counter this effect. First the laser power is chosen such that the saturation parameter $s = I/I_s \simeq 50$ is large to induce power broadening on the atomic line. Second the laser frequency is broadened by means of RF control and acousto-optic modulation up to a full width of 6 MHz, with a center frequency detuning of -3 MHz. These two contributions bring the capture velocity of the MOT to 8 m/s, in tune with the Zeeman slower.

This constitutes the first part of the MOT stage, the capture and trapping strictly speaking. Once the number of atoms in the MOT reaches a plateau of typically 10^8, the power is reduced to $s = 0.1$ and the frequency modulation is turned off. The center frequency is at the same time reduced to -1.5 MHz to compensate for the reduction of trapping force occurring when lowering the power. These changes result in compression and cooling of the MOT cloud down to 15 µK, which occurs without losing atoms. The atoms are also polarized in the state $|J = 8, m_J = -8\rangle$ through processes detailed in [21] where a complete study of the MOT can be found.

1.3.3 Transport

Next we describe the transport setup and the main reasons why this is a sound choice on the experiment. There are several reasons why a transport scheme is used, the main one being optical access. Indeed the MOT chamber has 6 wide laser beams coming from all directions which occupy most of the available space. Once a cold cloud is obtained in the MOT, a next stage of trapping and evaporative cooling is

required to go below the μK level, which in our case requires optical dipole traps. Further experiments on a cold cloud or BEC would also require additional laser beams. Rather than trying to find available directions of space to send additional laser beams on the atomic cloud, the choice here is to transport the atoms to the glass cell which is the last part of the experiment. This grants a lot more optical access for further experimental schemes and also allows us to get rid of possible eddy currents since the glass cell has no metallic casing like the MOT chamber. This is especially relevant for experiments that require very fine tuning of the magnetic field such as working close to a Feschbach resonance or spin squeezing close to zero magnetic field as will be described later on.

The way we transport atoms is by using an optical dipole trap (ODT) at 1070 nm whose focal point can be moved along the direction of propagation of the laser. The laser beam is produced by a YLR 50 W from IPG Photonics, with effectively 40 W of power on the atoms. A collimated beam goes through a converging lens before being reflected by a corner reflector mounted on a translation stage. This can artificially increase or decrease the distance between the lens and the focal point. Other techniques commonly used are magnetic transport schemes [43], or recently developed focus-tunable lenses for dipole traps [44].

The initial position of the focal point (with a waist of 35 μm) is at the center of the MOT chamber where the laser beam overlaps with the atomic cloud and its final position is 30 cm away, in the glass cell. A detailed description of the transport setup was given in the thesis of C. Bouazza [45]. The key point to keep in mind is the adiabaticity of the transport procedure. Increasing the magnetic field along the vertical direction to split the Zeeman levels and making the transport slow enough ensures that the atoms stay in the $|J = 8, m_J = -8\rangle$ state and that the center-of-mass motion mode of the atomic cloud does not get excited. A few 10^6 atoms are transported to the glass cell.

1.4 The glass cell

The glass cell is where the last steps of the experimental cycle occur. The atoms are transferred from the transport beam to a crossed optical dipole trap (cODT) where evaporative cooling is performed in order to obtain thermal atomic clouds at typically 1 μK or Bose-Einstein condensates (BEC) at temperatures of a few hundred nK. Figure 1.6 shows the cell and the various laser beams used.

1.4.1 In-trap Doppler cooling

The transport ODT has a trap depth of around 0.7 mK, such that the temperature of the atomic cloud after transport is roughly 90 μK, whereas the MOT temperature was 15 μK. This is not heating induced by non-adiabaticity of the transport but simply due to the transfer from the MOT to a deep ODT, the volume and temperature of the cloud adjusting themselves in an isentropic way. Even though evaporative cooling could be performed right away with these initial conditions, it proved to be necessary to first apply in-trap Doppler cooling in the transport ODT. Indeed decreasing the temperature early on results in an enhanced collision rate, increasing the evaporation efficiency. The condensation threshold can then be reached

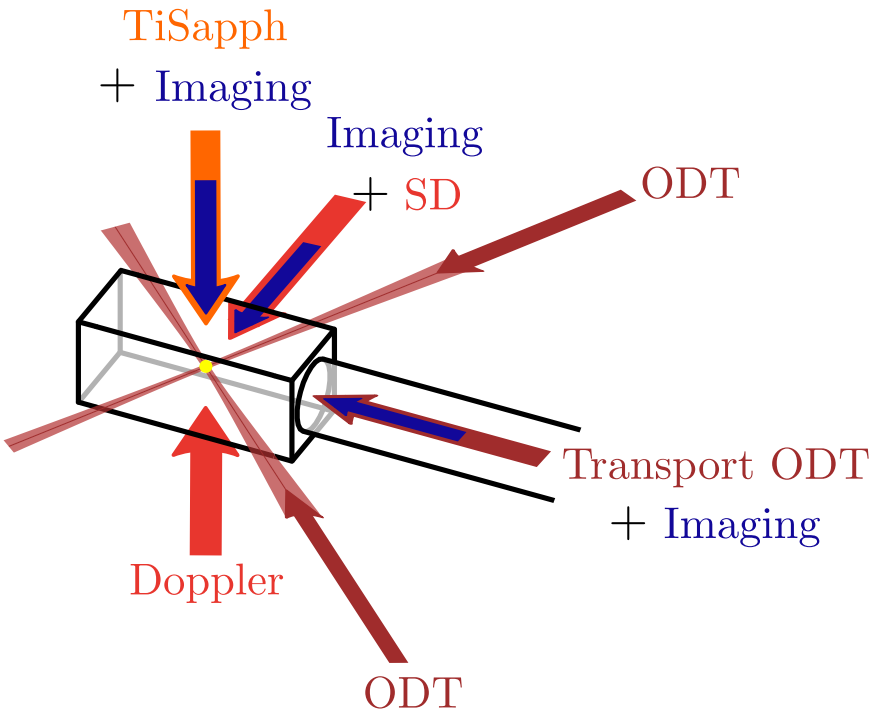

Figure 1.6 – Scheme of the glass cell and associated laser beams. The trapped atoms (yellow) sit at the center of the cell at the intersection of the two ODTs (dark red). An imaging beam (blue) overlaps with the transport beam coming from the MOT region. Another imaging beam in the horizontal plane arrives from the side of the cell and overlaps with the spin dynamics beam (SD, red). The Doppler beam (red) comes from below. Finally the TiSapph beam (orange) comes from the top and overlaps with the third imaging beam along the vertical direction. Laser beams of different wavelengths are superimposed using dichroïc mirrors. The magnetic coils are not represented for simplicity.

before all the atoms leave the trap in the evaporation process.

At this point the atoms are only held by the transport beam and the cODT is not yet on. A broad laser beam close to the 626 nm transition is sent from below to cool down the atoms. There is no counter propagating beam as one would expect from basic Doppler cooling theory. The fact that the atoms are held in the ODT is enough to induce an attractive force towards the center of the trap. However the cooling only occurs along the vertical direction and we expect the cloud to thermalize, the atomic collisions spreading the velocity reduction among all three directions. In-trap cooling has been performed in magnetic traps [46] as well as optical dipole traps [47].

The peak density at the center of the trap is $n_0 \sim 1.2 \times 10^{13}$ cm^{-3} from which we expect multiple photon scattering by the trapped atoms [48] and therefore reduced cooling efficiency. The intuitive solution would be to use a mask to prevent light from hitting atoms in the center of the trap and only address the wings of the atomic distribution, but it has technical disadvantages. We present here a technique in the spirit of [49] that relies on the tunability of the differential light-shift induced by the trap to effectively prevent the atoms at the center of the trap from seeing resonant Doppler-cooling light. This study led to a publication [50].

Differential polarizability

The ODT laser beam is linearly polarized (along $\boldsymbol{u}$) and therefore the vector part of the polarizability in the expression of $\hat{V}$ (equation 1.7) will cancel. A magnetic field sets the quantization axis and induces a Zeeman splitting such that the overall Hamiltonian is

$$\hat{H} = g_J \mu_B \, \hat{\boldsymbol{J}} \cdot \boldsymbol{B} + V_0(\boldsymbol{r}) \left(\alpha_J^s(\omega) \, \mathbb{1} + \alpha_J^t(\omega) \, \frac{3(\boldsymbol{u} \cdot \hat{\boldsymbol{J}})^2 - \hat{\boldsymbol{J}}^2}{2J(2J-1)} \right) \tag{1.9}$$

where $V_0(\boldsymbol{r}) = -|E|^2/4 = -I(\boldsymbol{r})/(2\epsilon_0 c)$ with $I(\boldsymbol{r})$ the laser intensity. The space dependence $\boldsymbol{r}$ corresponds to the gaussian profile of the ODT. The magnetic field is large enough so that the light shift can be treated as a perturbation on top of the Zeeman splitting. The ground state is still $|J = 8, m_J = -8\rangle$ and its energy is shifted by

$$\delta E_g = \langle m_J = -8 | \hat{V} | m_J = -8 \rangle = V_0(\boldsymbol{r}) \left(\alpha_J^s(\omega) + \alpha_J^t(\omega) \, \frac{3\cos^2\theta - 1}{2} \right) \tag{1.10}$$

where θ is the angle between the polarization vector $\boldsymbol{u}$ and the magnetic field $\boldsymbol{B}$. The tensor part remains much smaller than the scalar one.

However the tensor part becomes relevant once we consider the *differential light-shift* which is the relevant quantity here. Indeed the excited state $|J' = 9, m_{J'} = -9\rangle$ experiences a light-shift δE_e in the same way as equation 1.9 although its Landé factor $g_{J'}$ and polarizabilities are different. In the end the relative shift $\Delta E = \delta E_e - \delta E_g$ between the two states is

$$\Delta E = -(J' g_{J'} - J g_J) \mu_B B + V_0(\boldsymbol{r}) \left(\Delta\alpha^s(\omega) + \Delta\alpha^t(\omega) \, \frac{3\cos^2\theta - 1}{2} \right) \tag{1.11}$$

where the $\Delta\alpha^{s,t}$ correspond to the polarizability difference between the two states.

This results in a global shift of the resonance frequency ν according to

$$\nu = \nu_0^* + \frac{V_0(\boldsymbol{r}) \Delta\alpha(\theta)}{h} \tag{1.12}$$

where the Zeeman shift is contained in ν_0^* and $\Delta\alpha(\theta)$ encompasses the scalar term and the angular dependence due to the tensor term. The scalar part no longer dominates in this case as was observed by probing the 626 nm resonance with σ_- polarized light for different values of θ. A pulse of light at frequency ν is sent on

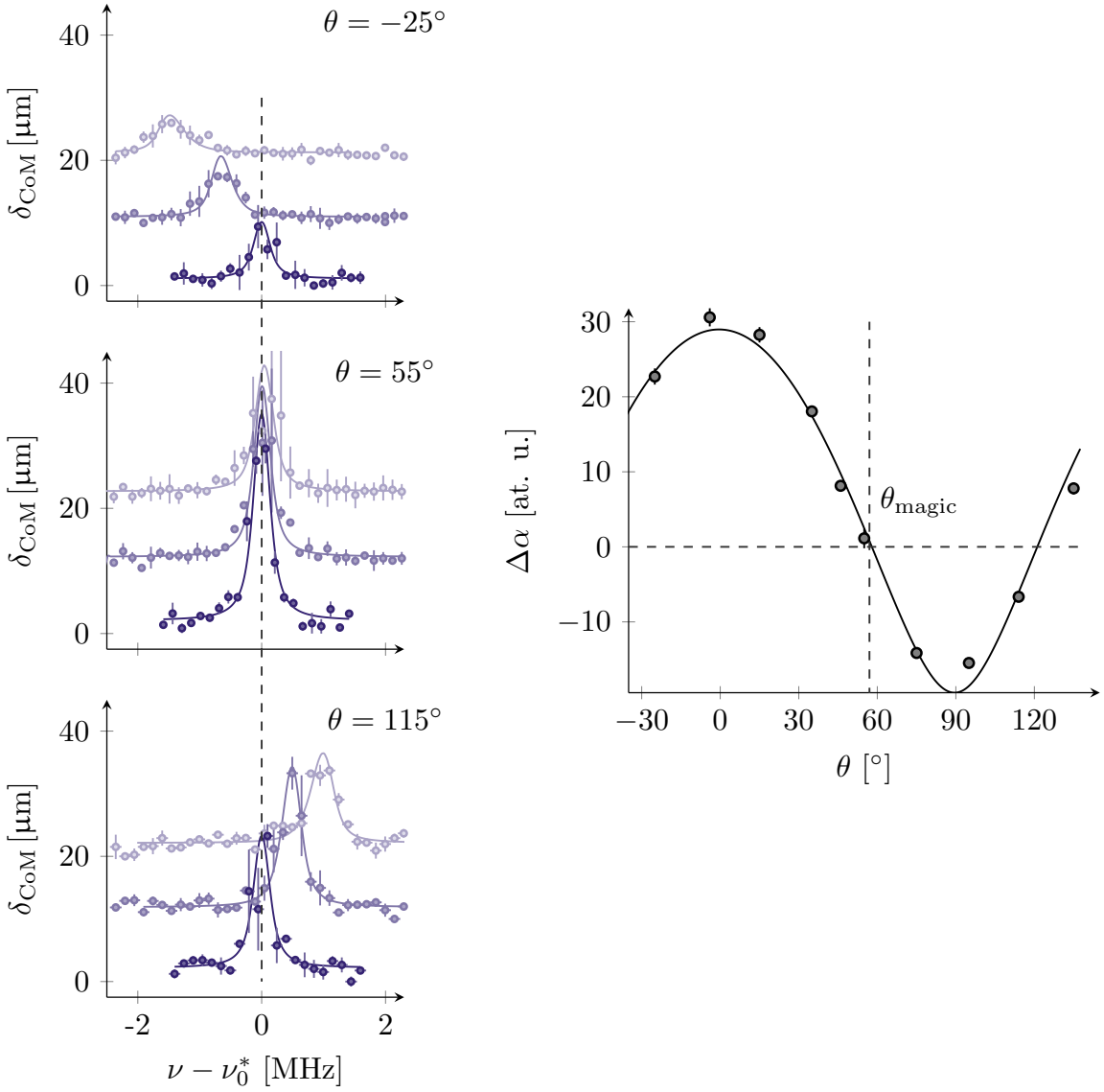

Figure 1.7 – Measurement of the differential polarizability from resonance shifts. **(Left)** Measurements of the resonance frequency as a function of the angle θ. The three shades of blue correspond to three different trap depth, i.e. three values of $V_0(\boldsymbol{r} = \mathbf{0})$. The darker shade correspond to the absence of trap, i.e. the bare resonance frequency. The magnetic field is kept constant for all the measurements hence the use of ν_0^* as reference. The link between the value of θ and the sign of the frequency shift is clearly visible. **(Right)** Differential polarizability $\Delta\alpha$ as a function of θ. $\Delta\alpha^s$ and $\Delta\alpha^t$ are the two free parameters of the fit which yields $\theta_{\text{magic}} \simeq 57(2)°$.

the trapped atoms which receive a kick inducing a position shift δ_{CoM} after a time of flight of 1.5 ms. The result is shown on figure 1.7.

Even though the scalar part is one or two orders of magnitude larger than the tensor part for both the ground and excited states, $\Delta\alpha^s$ and $\Delta\alpha^t$ are comparable.

As a result, $\Delta\alpha(\theta)$ can change sign and cancels for a certain angle θ_{magic} which corresponds to a situation of equal light-shifts for the ground and excited states.

Effect on the cooling efficiency

The set of tunable parameters involved in the cooling process are the light frequency ν, the light intensity through the saturation parameter s, the duration of the light pulse τ and, as we already detailed, the angle θ between the quantization axis and the ODT linear polarization. Even though we expect the cooling to be optimal for a detuning $\nu - \nu_0^* = -\Gamma/2$ from usual Doppler cooling theory, the in-trap cooling performed here can be quite different with the interactions between atoms playing an important role in the redistribution of the cooling along the three spatial directions as mentioned earlier. Nevertheless scans of the four different parameters can be performed in a reasonable amount of time to reach an optimum.

The figure of merit to optimize is the elastic collision rate $\gamma_{\text{coll}} = (2/\sqrt{\pi})\, n_0 \sigma \bar{v}$ where n_0 is the atom density at the center of the trap, σ the scattering cross-section and $\bar{v}$ the average velocity [51]. Indeed the step following the in-trap Doppler cooling is evaporative cooling whose efficiency strongly depends on collisions between atoms. The density scales like $N/T^{3/2}$ and the average velocity $\bar{v}$ scales like $T^{1/2}$ so that γ_{coll} scales like N/T. In the procedure performed here, the total number of atoms obviously cannot increase and the aim is therefore to optimize the cooling while limiting atom losses to maximize the collision rate.

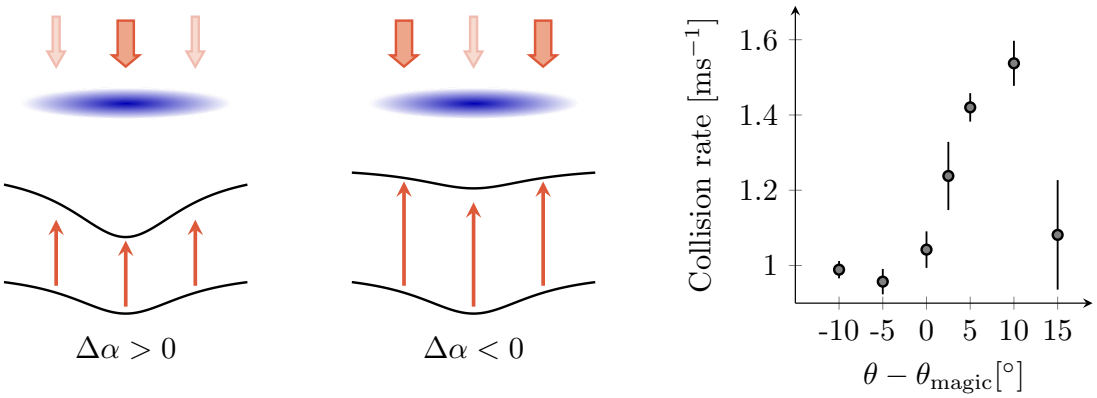

Figure 1.8 – Optimal cooling configuration. **(Left)** Trap profiles for the ground and excited states depending on the sign of $\Delta\alpha$. The ground state trap profiles are represented identically and the excited state trap 'carries' the effect of the differential polarizability. In reality both the ground and excited states traps change with θ but only the relative change between them matters. **(Right)** Measured collision rate in the trap as a function of the polarisation angle. The optimum corresponds to $\Delta\alpha < 0$.

Two different regimes are observed depending on the sign of $\Delta\alpha$ as qualitatively described on figure 1.8. For $\Delta\alpha > 0$, the Doppler beam is closer to resonance for the atoms sitting at the center of the trap than it is for the trap wings. This means that we are trying to cool down the atoms in the most dense region, causing light-assisted collisions associated with high atom density and in turn atom losses. The process is therefore inefficient.

On the other hand for $\Delta\alpha < 0$, we address the wings of the spatial distribution more efficiently while leaving the atoms at the center of the trap unaffected. The optimum was found for $\theta = \theta_{\text{magic}} + 10°$, $s = 0.5$, $\tau = 20$ ms and a frequency ν corresponding to a detuning of typically -0.3 Γ. The gain in collision rate corresponds to a factor 1.9 compared to the absence of Doppler cooling.

1.4.2 Magnetic field control

Coils placed around the glass cell in Helmholtz configuration are used to control accurately the magnetic offset field and gradient separately along all three directions. The main limitation concerning magnetic field stability is caused by the nearby Paris metro line. This could be checked by overnight measurements which show how the noise disappears when the metro lines are shut down. It consists in a slow variation (with a typical timescale of 1 s) of the magnetic field along the vertical direction only, with RMS value 2 mG.

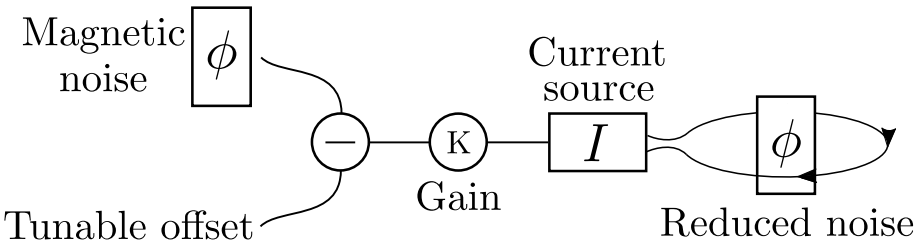

Figure 1.9 – Scheme of the magnetic field noise compensation design. The symbol ϕ stands for magnetic flux based magnetometers

This noise is corrected using a basic open-loop design described on figure 1.9. The noise is measured by a probe placed far enough from the experiment so that it is not sensitive to magnetic field actively varied during the experimental sequence nor magnetic field noise from other experiments or technical devices in the building. This probe still feels the same metro-noise as the atoms since the source is located far away. The probe signal is then sent to a power supply generating a current proportional to its input signal. The power supply is connected to the large coils placed around the entire experiment so that it compensates the metro-noise everywhere as far as the experiment is concerned. This works as long as the variation that we are trying to compensate is much slower than the reaction time of the compensation, which is obviously the case here. The noise reduction factor is close to 7, with a corrected noise RMS value of 0.3 mG (see figure 1.10), which is similar to the noise on the two other directions of space.

In the end the remaining slow variations induce shot-to-shot variations on the experimental results that can partially be taken into account by measuring the magnetic field with an external probe placed close to the atoms and post-processing the data. An additional coil placed below the cell is used for Stern-Gerlach measurements. Large capacitors (2.2 mF) are used to create a current discharge of several hundred amperes over 1 ms resulting in a vertical magnetic field gradient of about 50 G/cm. This allows us to separate different spin-states along the vertical direction and therefore measure the spin composition of the atomic cloud.

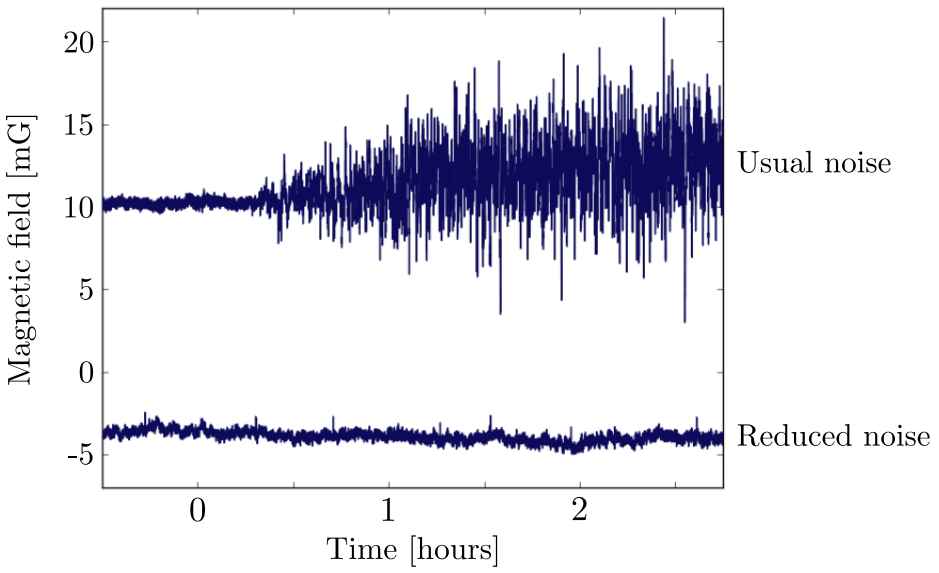

Figure 1.10 – Recording of the magnetic field noise over several hours. The offset between the two curves is arbitrary as the two signals are recorded by probes placed at different spots. The noise is initially not present because it corresponds to night hours when the metro is not running. The x-axis corresponds to absolute durations, with the value 0 corresponding to something close to 5 a.m. in reality.

1.4.3 Imaging

Standard absorption imaging is performed at resonance on the blue transition at 421 nm. The large width of this transition ensures good absorption probability irrespective of small energy level shifts. A pulse of light is sent on the atoms and a camera placed after the cell takes a picture of the shadow of the atomic cloud. The amount of light absorbed by the atoms can be related to the column density $\bar{n}(x, y)$ using the Beer-Lamber law (valid for $I \ll I_{\text{sat}}$)

$$I(x, y) = I_0(x, y) \exp\left(-\sigma_0 \bar{n}(x, y)\right) \tag{1.13}$$

where $\bar{n}(x, y) = \int \mathrm{d}z\, n(x, y, z)$ with z the direction of propagation, and $\sigma_0 = 3\lambda^2/2\pi$ is the scattering cross section at resonance. Then the total atom number N is

$$N = \int \mathrm{d}x\, \mathrm{d}y\, \mathrm{d}z\, n(x, y, z) = \frac{1}{\sigma_0} \int \mathrm{d}x\, \mathrm{d}y \log \frac{I_0(x, y)}{I(x, y)} \tag{1.14}$$

A first picture of the atoms is taken and then typically 100 ms later a background picture, once the atoms have left the field of view. This constitutes a measure of $I(x, y)$ and $I_0(x, y)$ and in turn the density profile $\bar{n}(x, y)$ and N. Dividing $I(x, y)$ and $I_0(x, y)$ also has the advantage of removing static features such as diffraction rings caused by dust particles or optics imperfections. The pixel size on the CCD of the camera combined with the magnification of the various lenses used lead to a resolution of 3 µm per pixel.

In total there are three imaging beams around the glass cell. One along the transport direction, a second perpendicular to it coming from the side of the cell and finally a vertical one from the top (figure 1.6). This allows us to check that all three dipole traps intersect correctly at the center of the cell which is part of the routine checks on the experiment.

1.4.4 Atom trapping

After Doppler cooling is performed on the atoms trapped in the transport beam, they are transferred to the cODT. The two dipole traps are generated using two different 1064 nm AzurLight Systems infrared lasers at 50 W and 10 W. Acousto-optic modulators are used to control the diffracted power effectively sent to the atoms as well as the width of each laser beam thanks to spatial modulation as detailed in chapter 2. They allow the implementation of evaporative cooling, also described in chapter 2, used to obtain ultracold gases of dysprosium atoms.

These two beams are incident on the two sides of the glass cell at an angle close to the Brewster angle (53° based on the optical index of quartz) to avoid any unnecessary light reflexion and maximize transmission inside the cell. They are focused at the position of the atoms at the center of the cell with a waist of typically 25 µm and are damped after exiting the cell.

1.4.5 Other laser beams

The other laser beams sent on the glass cell are related to various projects. The red beam at 626 nm sent from the side is used to induce quadratic spin coupling which will be detailed in chapter 3. By adding a counter propagating red beam to the first one and playing with the detuning, one can perform Raman transfer within the $|J = 8, m_J = -8, ..., 8\rangle$ manifold as described in chapter 6.

Finally a laser beam coming from a M Squared Ti-sapphire laser can be sent on the atoms from the top. The wavelength of this beam can be tuned between 695 and 1005 nm which opens new perspectives about future projects discussed in part III.

Chapter 2

Dipole trap modulation and Evaporative cooling

As briefly mentioned in the previous chapter, a spatial modulation of an ODT can be used to increase its width in a tunable manner. This technique was used to improve the atom transfer from the transport beam to the cODT by maximizing the spatial overlap and was necessary to obtain a BEC at the end of the evaporative cooling stage. In this chapter we first describe the idea of atom trapping using far-detuned laser beams and then explain how their shape can be modified using acousto-optic modulation. Such techniques have been used to produce double-well potentials [52] and more recently to optimize the transfer between two dipole traps [53] in a similar way to the work presented here.

The principle of evaporative cooling is then described and the efficiency of the evaporation procedure in our setup is measured. This technique was first introduced in the context of cooling hydrogen contained in a tank [54], which was the first candidate for the realization of dilute quantum gases. It was later extended to magnetic and/or laser trapped alkali elements. It consists in a process of temperature-dependent atomic losses where the hottest atoms are allowed to leave the trap, which result in an overall reduction of the temperature of the gas. Historically it proved to be necessary to reach Bose-Einstein condensation, even though this regime has been reached recently using novel cooling techniques, without the use of evaporation [55].

2.1 Principle of time-averaged-potentials

2.1.1 Generalities about optical dipole traps

Optical trapping of neutral atoms relies on the atom-light interaction far from any optical transition. It is a tunable tool whose main advantage is to produce spin-independent trapping whereas magnetic traps can only be used for either low field- or high field-seeking states. Optical traps were for example used to produce spinor condensates [56]. In the far-detuned regime, the potential induced by a laser field on an atom is [57]

$$U_{\mathrm{dip}}(\boldsymbol{r}) = -\frac{I(\boldsymbol{r})}{2\epsilon_0 c}\mathrm{Re}(\alpha) \tag{2.1}$$

where α is the polarizability introduced in equation 1.7. From figure 1.3 we know that the scalar part is positive and much larger than the vector or tensor parts away from sharp resonances. We use linearly polarized light at 1064 nm and the overall coupling is therefore attractive.

The intensity profile of a gaussian beam is

$$I(\boldsymbol{r}) = I_0 \left(\frac{w_0}{w(z)}\right)^2 \exp\left(\frac{-2(x^2+y^2)}{w(z)^2}\right) \tag{2.2}$$

which corresponds to a beam of minimal waist w_0 propagating along z. The maximum intensity I_0 relates to the total power P as $I_0 = 2P/(\pi w_0^2)$ and the waist at position z is

$$w(z) = w_0 \sqrt{1 + \left(\frac{z}{z_R}\right)^2} \tag{2.3}$$

where $z_R = \pi w_0^2/\lambda$ is the Rayleigh length. The corresponding ODT is then given by a potential

$$U(\boldsymbol{r}) = -U_0 \left(\frac{w_0}{w(z)}\right)^2 \exp\left(\frac{-2(x^2+y^2)}{w(z)^2}\right) \tag{2.4}$$

where $U_0 = I_0 \mathrm{Re}(\alpha)/(2\epsilon_0 c)$. As expected from the shape of a gaussian beam, the confinement is much stronger along the transverse direction than it is along the axial direction. One can extract the two corresponding trap frequencies by performing a Taylor expansion of the expression of $U(\boldsymbol{r})$ close to its maximum at $\boldsymbol{r} = \boldsymbol{0}$. The expression reduces to

$$U(x,y,z) = -U_0 + \frac{1}{2} m \left[\omega_r^2 (x^2+y^2) + \omega_z^2 z^2\right] \tag{2.5}$$

where $\omega_r^2 = 4U_0/(m w_0^2)$ and $\omega_z^2 = 2U_0/(m z_R^2)$ and indeed $\omega_r/\omega_z = \sqrt{2}\pi w_0/\lambda \gg 1$ which means that the trap is much more tight in the transverse plane.

Based on this fact, one needs to combine two single-beam ODTs to obtain a trap with a more or less spherical shape, depending on the relative angle between the beams, relative powers and waists (assuming they have the same wavelength). The most common case is to combine two orthogonal beams such that the resulting trap frequencies can be immediately inferred from each of the transverse single-beam frequencies (the second contribution would be the axial frequency from the other beam which is negligible). This is the case on the experiment as described on figure 1.6.

2.1.2 Time-averaging criterion

The tunability and control of ODTs can be increased by adding spatial modulation. The idea is to move the position of the dipole trap in a periodic fashion to create an averaged trap with a different shape. This is sometimes referred to as 'painting' since it is reminiscent of the way a painter would move their brush on a canvas. It is a way to increase the trap size while at the same time reducing its

depth, keeping the volume constant. For a single-beam ODT described previously, we perform spatial modulation along the x direction only.

The modulation rate ω matters since we do not want to induce heating or lose atoms in the process. The characteristic frequency to consider in this case is the transverse trap frequency ω_r since it sets the motion of a trapped atom.

The situation of a rate of change of the trap small compared to ω_r corresponds to the case where the atoms would follow the trap adiabatically. A modulation for ω on the order of ω_r would induce resonant excitation of the center-of-mass motion mode of the atomic cloud and is therefore to be avoided. Finally when ω is much larger than ω_r, the atoms see only the averaged intensity profile which is precisely the desired situation [58].

2.1.3 Formalism

To compute the averaged trapping potential V we only need to consider one period of oscillation T, during which the center of the trap x_0 moves in a periodic way such that

$$V(x) = \frac{1}{T}\int_{-T/2}^{T/2} \mathrm{d}t\, U(x - x_0(t)) \tag{2.6}$$

where $U(x)$ is the trapping potential along x in the focal plane $U(x) = -U_0 \exp(-2x^2/w_0^2)$. For example a choice of modulation shape could be a sine of amplitude A

$$x_0(t) = A \sin(2\pi \frac{t}{T}) \tag{2.7}$$

where A is limited by the technical realization of the modulation and we typically have $A_{\max} \simeq 4w_0$.

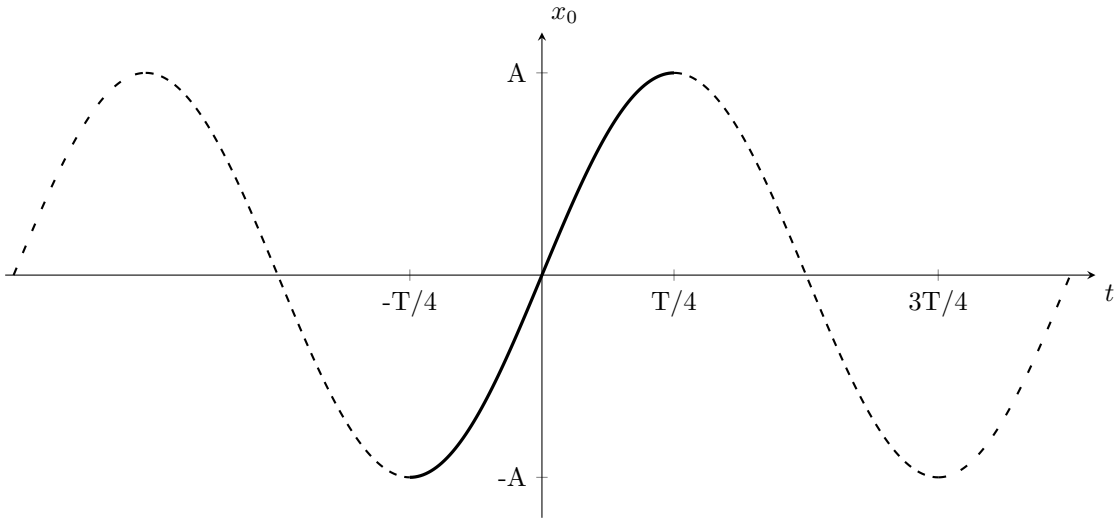

Figure 2.1 – Example of modulation shape. We can restrict ourselves to a domain of half a period over which the function is monotonic to compute the average potential.

From this example one can see that we could compute the average over half of the period only, between $-T/4$ and $T/4$, the second part of the modulation being the 'reflection' of the first part and yielding the exact same averaging. This is true only for modulation shapes that are monotonically increasing over the first half of the period and decreasing in a symmetric way over the second half. We restrict ourselves to such cases in the following and use the word *ramp* to describe the modulation shape.

We can perform a change of variable by writing $x_0 = f(2\pi t/T)$ and restricting the integral over the first half of the period

$$\begin{aligned} V(x) &= \frac{1}{T}\int_{-T/2}^{T/2} \mathrm{d}t\, U(x - x_0(t)) \\ &= \frac{2}{T}\int_{-T/4}^{T/4} \mathrm{d}t\, U(x - x_0(t)) \\ &= \frac{1}{\pi}\int_{-A}^{A} \frac{\mathrm{d}x_0}{(f' \circ f^{-1})(x_0)}\, U(x - x_0) \\ &= \int_{-A}^{A} \mathrm{d}x_0\, \Pi(x_0)\, U(x - x_0) \end{aligned} \tag{2.8}$$

where it is now visible that the average trap is the convolution product of the regular profile $U(x)$ with a normalized gate function $\Pi(x)$ which depends on the modulation shape. Flatter areas of the modulation shape (such as the sine modulation close to its extrema) lead to maxima of the gate function. Indeed the laser beam 'spends more time' in regions where the modulation shape is horizontal. $\Pi(x)$ is a distribution that reflects the amount of time spent by the laser beam at position x. It is normalized according to

$$\int_{-A}^{A} \Pi(x)\, \mathrm{d}x = 1$$

We also see from the previous computations that if we want a symmetric potential along x we need a modulation ramp that is an odd function.

2.1.4 Choice of the modulation shape

A few examples of modulation ramps with their associated gate functions are listed below :

- For a linear ramp, the beam spends the same amount of time at each position, resulting in a uniform distribution

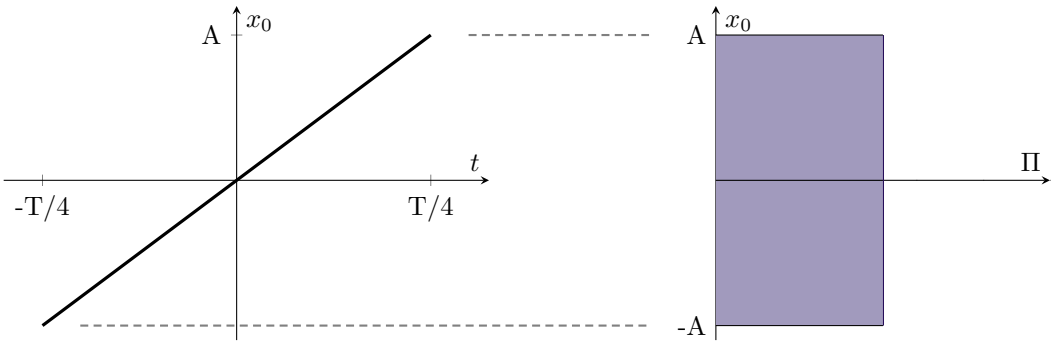

- For a sine modulation, the fact that the ramp is flat on the edges leads to divergences of Π. The function remains integrable as $\Pi(x) \propto 1/\sqrt{1 - x^2/A^2}$ and is a valid gate function.

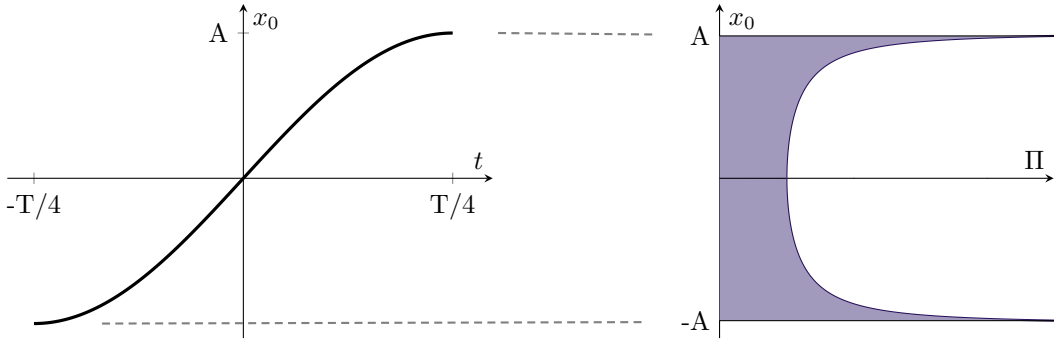

- Finally the arcsine modulation corresponds to the opposite behaviour compared to the sine. Vertical slope on the edges lead to canceling of Π. In this case $\Pi(x) \propto \cos(\pi x/(2A))$.

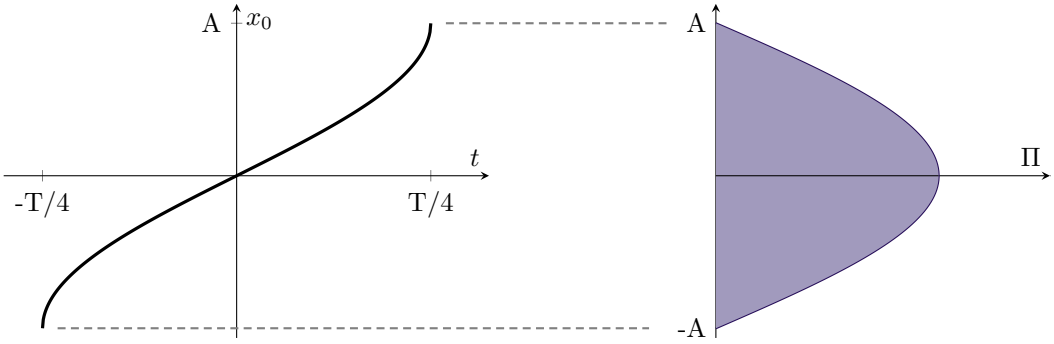

These three modulation shapes correspond to the three following trap profiles.

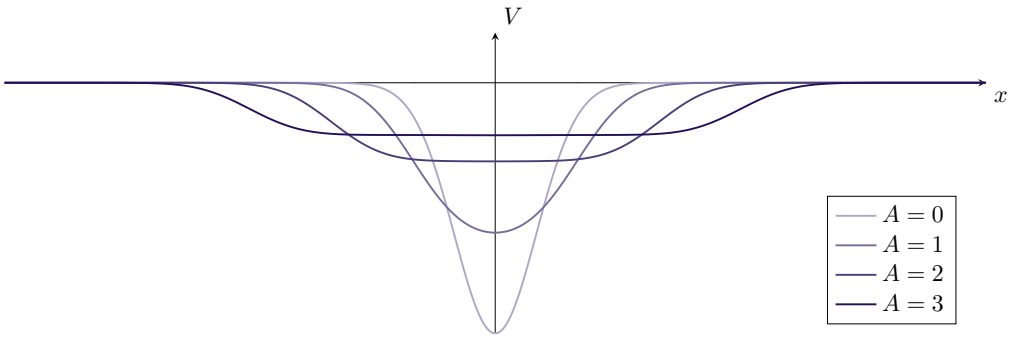

Figure 2.2 – Average trap for a linear modulation for different values of A. The fact that we obtain a flat-bottom trap is not surprising given that the linear modulation corresponds to a uniform distribution. For $A = 0$ there is no modulation and we recover the gaussian profile of the bare laser beam. A is expressed in units of the beam waist w_0.

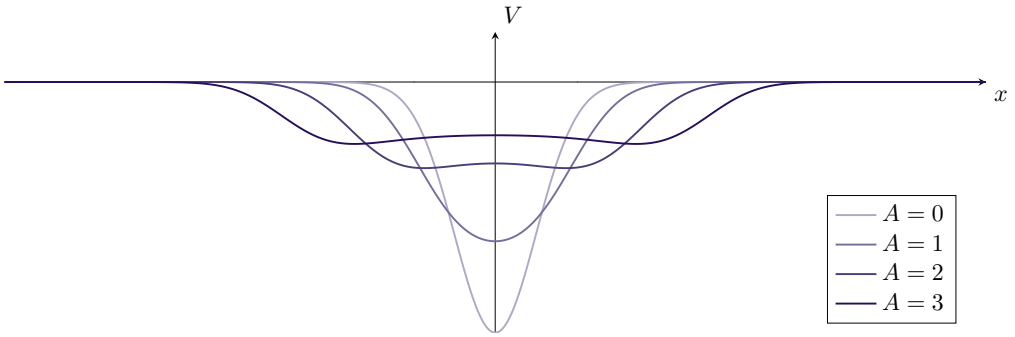

Figure 2.3 – Average trap for a sine modulation for different values of A. The trap looks almost the same as the previous one except that it presents two local minima on the sides due to the shape of the gate function for the sine modulation. It makes it a bad choice for usual atom trapping.

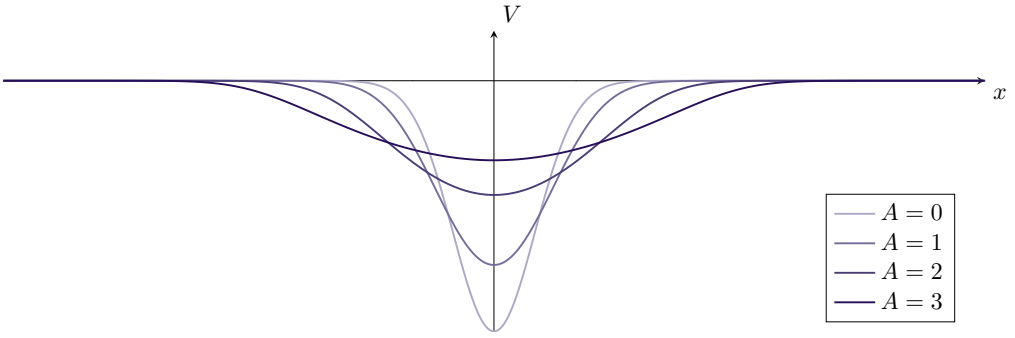

Figure 2.4 – Average trap for the arcsine modulation for different values of A. The result looks quite similar to a usual gaussian trap, although it is not exactly gaussian.

The choice of the arcsine modulation is natural to obtain a trap which is harmonic around its center (figure 2.4). This is a requirement to apply the usual results of evaporative cooling and cold atoms collision theory in harmonic traps.

Note that if the modulation amplitude A is much larger than the waist of the laser w_0, one can assume that it is infinite and the convolution product introduced in equation 2.8 can be extended from $-\infty$ to $+\infty$. In this case one can see that a modulation shape given by $x_0(t) = \mathrm{erf}^{-1}(4t/T)$, where erf is the error function, leads to a gate function Π which is gaussian. The convolution of two gaussian distributions being gaussian, this yields an average trap V which is exactly gaussian.

In practice A is finite and not necessarily much larger than the waist which means that only a truncated erf^{-1} could be used (erf^{-1} is an odd function defined in $[-1, 1]$ with $\lim_{x\to 1} \mathrm{erf}^{-1}(x) = +\infty$)

The question whether this truncated modulation would give a better average trap than the arcsine one was not investigated as the difference is minor. In the end according to the considerations presented so far the modulation choice is the following

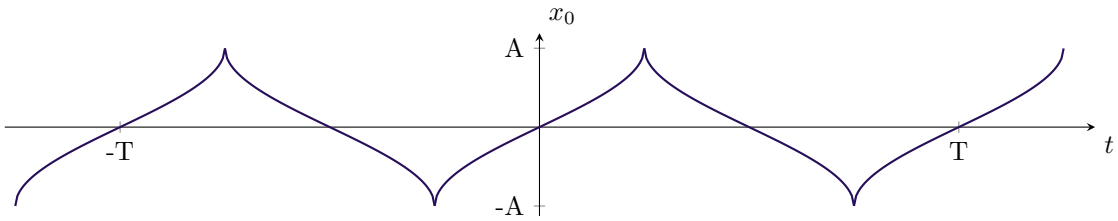

Figure 2.5 – Modulation signal chosen on the experiment.

2.2 Experimental realization

2.2.1 Optical setup

The trap modulation is experimentally realized with a collimated beam going through an AOM whose working frequency can be tuned. When the AOM is working at its center frequency $\nu_0 = 80$ MHz, the diffracted beam goes first through a telescope formed by two lenses and then through the final lens to focus it on the atoms as represented on figure 2.6 The beam is centered on these optical elements for $\nu = \nu_0$. A frequency shift $\delta\nu$ results in a tilt θ at the output of the AOM and in turn a position shift δ of the focal point in the focal plane of f_3 according to

$$\delta = \frac{f_1 f_3}{f_2} \tan(\theta) \quad \text{with} \quad \theta = \frac{\lambda\, \delta\nu}{c} \tag{2.9}$$

where the f_i are the focal lengths of the three lenses in increasing order, $\lambda = 1064$ nm, $c = 5740$ m/s is the speed of sound in the AOM crystal and $\delta\nu$ ranges from -15 MHz to 15 MHz for the AOM used (AA Optoelectronics MCQ80).

We insist on the fact that the AOM does not act as a source point but as a deflector. This means that the AOM position is not constrained to the focal plane of the first lens. Equation 2.9 is valid as long as θ is small enough for the paraxial

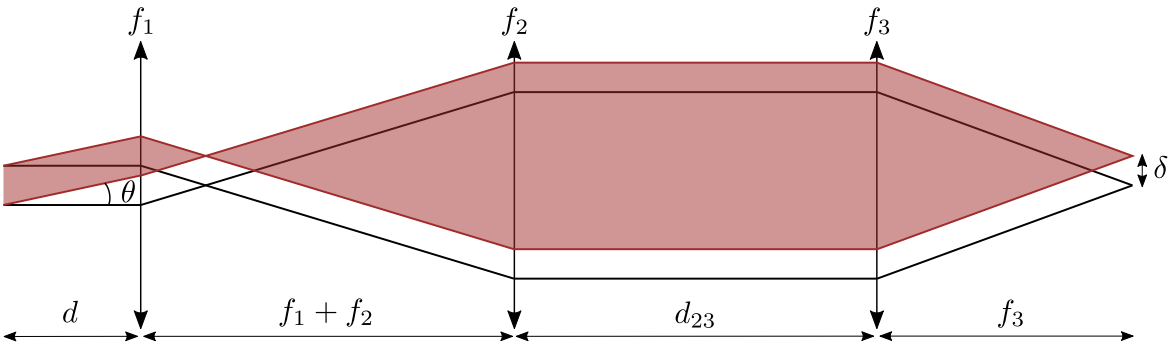

Figure 2.6 – Scheme of the optical elements. The black lines correspond to the AOM-diffracted beam for $\nu = \nu_0$ while the red lines correspond to $\nu = \nu_0 + \delta\nu$. The initial tilt θ between the two collimated beams translates into a shift δ in the focal plane. The distance between f_2 and f_3 is arbitrary and chosen for space convenience in practice.

approximation to be valid and the beam hits the first lens close enough to its center to avoid aberrations.

However there is a constraint on the AOM position from the fact that we want the beam to be focused on the atoms without any angle, which is the case on figure 2.6. This requires that a collimated beam arriving on f_3 from the other side of the optical setup ends up focused after f_1 at the AOM position. It is equivalent to saying that the AOM is in the focal plane of the optical system formed by the three lenses. This results in

$$d = f_1 + \frac{f_1^2}{f_2} + \frac{f_1^2}{f_2^2}(f_3 - d_{23}) \tag{2.10}$$

where d is the distance between the AOM and f_1, and d_{23} is the distance between f_2 and f_3. Given the values of the three f_i given below, d marginally depends on d_{23} and is roughly equal to 80 mm. Both equations 2.9 and 2.10 are derived from ray transfer matrix analysis summing up the optical elements used here.

The focal lengths of the lenses are chosen such that the beam is focused down to a waist of 26 µm. The available space on the experimental setup sets $f_3 = 300$ mm and the initial diameter of the laser beam sets the telescope magnification, with a choice of $f_1 = 75$ mm and $f_2 = 684.5$ mm. The resulting position shift for $\delta\nu = 15$ MHz is $\delta = 91$ µm. By modulating $\delta\nu$ at a rate of 50 kHz (much larger than the trap frequency), we induce a widening of the trap allowing a better spatial overlap when transferring atoms from the transport beam to the cODT.

2.2.2 Application of the modulation

Atomic transfer

The atoms are transferred from the transport ODT to the cODT by overlapping the two traps and waiting for the atoms to 'fall' in the crossed region. The spatial modulation is useful as the atomic cloud trapped in the transport beam has a very elongated shape (so-called 'cigar' shape), with diameter $\sim w_0 \simeq 35$ µm and length $\sim z_R \simeq 3.6$ mm). In the absence of modulation, the spatial overlap with the

cODT (which has a spherical shape of diameter $\sim w_0 \simeq 25$ µm) is quite poor. When modulating at the full amplitude allowed by the bandwidth of the AOM, the waist of each beam becomes around 4.5 times larger, accompanied by a trap depth reduction by a factor 3.7. The atomic transfer is typically increased by a factor 2 thanks to the modulation.

The transfer lasts around 100 ms after which the modulation is turned off. As mentioned in section 1.4.1, the efficiency of the evaporative cooling relies on a high collision rate value. It is therefore beneficial to turn off the modulation and return to a tight confinement to increase the atomic density at the center of the trap before starting the evaporation. This process is isentropic if performed slowly enough.

Cloud shape tuning

The widening of both arms of a cODT allows for a tuning of the aspect ratio of the atomic cloud which is particularly important in the case of dipolar BEC stability. Indeed dipole-dipole interactions induce an orientation-dependent force corresponding to the potential energy [59]

$$U_{dd}(\boldsymbol{r}) = \frac{\mu_0 \mu^2}{4\pi} \frac{1 - 3\cos^2\theta}{r^3} \tag{2.11}$$

where μ_0 is the vacuum permittivity, μ the atomic dipole moment, r the inter-atomic distance and θ the angle formed by the vector connecting two atoms and the direction of the bias magnetic field along which the dipoles are aligned. In particular the dipole-dipole interaction is attractive for certain values of θ, and attractive interactions usually lead to BEC collapse [60]. The strength of the dipolar interaction can be expressed in terms of a dipolar length a_{dd}, similarly to the scattering length a associated with s-wave collisions described by a δ-potential, as

$$a_{dd} = \frac{\mu_0 \mu^2 m}{12\pi\hbar^2}. \tag{2.12}$$

The dimensionless quantity $\epsilon_{dd} = a_{dd}/a$ is the usual figure of merit used to compare the two interactions. The stability of a trapped dipolar BEC depends on the aspect ratio of the cloud [61], as the trap shape can reduce attractive head-to-tail dipole-dipole configurations. Indeed in a 'pancake' shape, with a polarizing magnetic field, the dipoles are mostly aligned side-by-side which corresponds to repulsive interactions. The ODT modulation can be used to tune the effective waist of a beam in a continuous way to ensure stability.

Note that for all the work presented in this manuscript, we stay away from Feschbach resonances so that the value of the scattering length is the background value $a_{bg} = 140(7)\, a_0$ for ^{162}Dy, corresponding to $\epsilon_{dd} = 0.92(5)$. It can be shown [61] that for $\epsilon_{dd} < 1$, a dipolar BEC is stable regardless of the trap aspect ratio (assuming cylindrical symmetry) so that stability is guaranteed in our case. Dipole-dipole interactions still contribute to some extent in the collisions during the evaporation process. In particular they enable evaporative cooling of fermions since they compensate the lack of s-wave collisions at low temperature as demonstrated in [19].

2.3 Evaporative cooling

2.3.1 Principle

The idea of evaporative cooling is to let the hottest atoms in the cloud leave the trap while random collisions ensure thermalization between the remaining atoms, resulting in an overall cooling of the cloud. The trap depth U_0 is assumed to be not too large compared to the energy $3k_BT$ so that atoms may leave the trap. Some 'lucky' atoms undergo collisions that increase their velocity above the trapping threshold and they leave the trap. They correspond to the tail of the Maxwell-Boltzmann velocity distribution describing the gas at temperature T

$$P_T(v) = \sqrt{\frac{2}{\pi}} \left(\frac{m}{k_BT}\right)^{\frac{3}{2}} v^2 \exp\left(-\frac{mv^2}{2k_BT}\right) \tag{2.13}$$

which is normalized to 1. The average kinetic energy $\langle E_c \rangle = m \langle v^2 \rangle /2 = 3k_BT/2$ of an atom remains well below the trap depth U_0 such that the cloud is trapped properly.

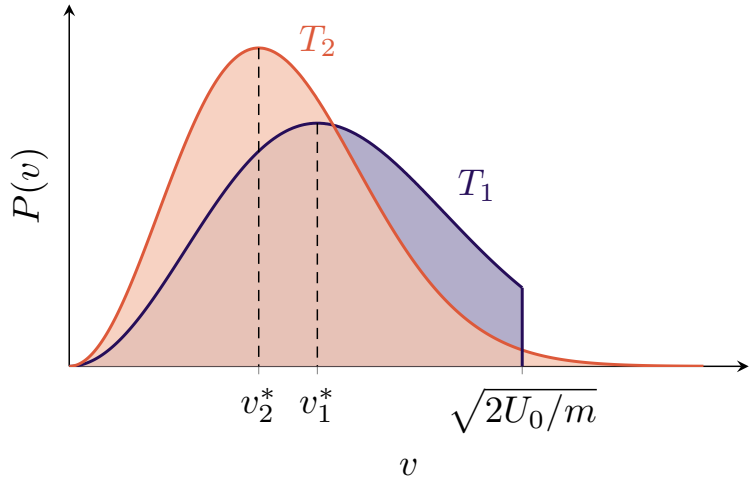

Figure 2.7 – Velocity distributions before and after atoms evaporate from the trap. The velocity $\sqrt{2U_0/m}$ corresponds to the escape threshold $U_0 = mv^2/2$, while v_1^* (resp. v_2^*) corresponds to the most probable velocity at temperature T_1 (resp T_2).

The atoms from the gas at temperature T_1 leave the trap and remove energy from the system, which returns to equilibrium and thermalizes to a lower temperature T_2 as represented on figure 2.7. T_2 is implicitly defined from the truncated T_1 profile as

$$\langle E_2 \rangle = \int_0^\infty \frac{1}{2} mv^2 P_{T_2}(v) dv = \int_0^{U_0} \frac{1}{2} mv^2 P_{T_1}(v) dv \tag{2.14}$$

and we indeed have $T_2 < T_1$. For a given U_0, this elementary process repeats itself and T diminishes until the probability for an atom to escape the trap $P \propto \exp(-U_0/(k_BT))$ becomes too small. This corresponds to being at the equilibrium temperature T, characterized by $\eta = U_0/(k_BT) \simeq 10$. The timescale corresponding

to the atoms spontaneously leaving the trap due to their high velocity scales as $\tau_{\text{evap}} \sim e^{\eta}$, while the losses due to collisions with residual gas particles in the vacuum chamber are described by τ_{loss}. If $\tau_{\text{evap}} > \tau_{\text{loss}}$, one will simply lose atoms in an inefficient way (since atom losses due to the residual gas are velocity-independent) by waiting too long.

Another loss mechanism called dipolar relaxation can be caused by dipole-dipole interactions [62]. This inelastic process consists in a spin-flipping collision between atoms of the type $|m_J\rangle + |m_J + 1\rangle \rightarrow |m_J\rangle + |m_J\rangle$ which releases the Zeeman energy $\Delta E = \hbar\omega_Z$ under the form of kinetic energy, causing the two atoms to leave the trap. This process is suppressed if all the atoms are polarized in the $|-8\rangle$ state and $k_B T \ll \hbar\omega_Z$ so that the $|-7\rangle$ state is not thermally populated. We ensure this is always the case by maintaining a sufficient magnetic field throughout the transport, loading and evaporative cooling steps.

2.3.2 Evaporation efficiency

The goal of the evaporative cooling is to increase the phase space density (PSD). The usual definition is

$$\mathcal{D} = n\lambda_{\text{dB}}^3 \quad \text{where} \quad \lambda_{\text{dB}} = \sqrt{\frac{2\pi\hbar^2}{m k_B T}} \tag{2.15}$$

where λ_{dB} is the thermal de Broglie wavelength. This quantity is useful to describe the length scale where quantum effects start being visible. Here we work with harmonic traps and the PSD reads

$$\mathcal{D} = N \left(\frac{\hbar\bar{\omega}}{k_B T} \right)^3 \tag{2.16}$$

where $\bar{\omega} = (\omega_x \omega_y \omega_z)^{1/3}$.

Evaporative cooling is efficient if the diminution of both N and T results in an increase of N/T^3. Otherwise we simply have inefficient atom losses. *Forced* evaporative cooling consists in reducing the trap depth U_0 in a controlled way to repeat the elementary step pictured on figure 2.7 to progressively increase the PSD. This is done by lowering the laser power of both arms of the cODT.

The evaporation process relies on atomic collisions (occurring on a timescale $\tau_{\text{coll}} \propto 1/\gamma_{\text{coll}}$) to restore a well-defined velocity distribution more quickly than the truncation occurs. This leads to the condition

$$\tau_{\text{coll}} < \tau_{\text{evap}} < \tau_{\text{loss}}. \tag{2.17}$$

A simple model of evaporation relating the number of atoms leaving the trap dN to the induced reduction of temperature dT shows that [63]

$$\frac{dT}{T} = \left(\frac{\eta + 1}{3} - 1 \right) \frac{dN}{N} \tag{2.18}$$

such that, from equation 2.16,

$$\frac{d\mathcal{D}}{\mathcal{D}} = \frac{dN}{N} - 3\,\frac{dT}{T} \tag{2.19}$$

$$= (2 - \eta)\frac{dN}{N}. \tag{2.20}$$

and the PSD increases as N diminishes if $\eta \geq 2$. Note that dT and dN are negative quantities.

The collision rate γ_{coll} mentioned in section 1.4.1 satisfies, in the case of harmonic traps,

$$\gamma_{\text{coll}} = \frac{m\bar{\omega}^3\sigma}{2\pi^2 k_B}\frac{N}{T}. \tag{2.21}$$

It scales like $\bar{\omega}^3 N/T$ and it is not obvious whether it increases or decreases as the evaporation goes on. Indeed $\bar{\omega}$ scales as $U_0^{1/2}$ according to equation 2.5 and decreases as the trap depth is lowered. It is not guaranteed that N/T increases enough to maintain a good collision rate. The *runaway* regime corresponds to the situation where γ_{coll} increases during the evaporation, which is the case if $\eta \geq 5$ [64].

In practice the value of η is limited by the exponential scaling $\tau_{\text{evap}} \sim e^{\eta}$ which still needs to remain smaller than τ_{loss}. Measurements of atom losses as a function of the holding time in the cODT showed an exponential decay corresponding to a $1/e$ lifetime ranging from 5 to 10 seconds, for different values of trap depth used during the evaporation. The total evaporation time is typically 3 seconds and the collision timescale τ_{coll} on the order of 10^{-2} seconds so that condition 2.17 is satisfied. The runaway regime is not attained in practice because of the opening of the optical trap during the evaporation according to a precise model [65]. This issue can be addressed by tuning the scattering length in the vicinity of a Feshbach resonance during the evaporation.

The figure of merit used to characterize the efficiency of an evaporative cooling sequence is the gain in PSD compared to the atom losses in log-log scale

$$\chi = -\frac{d\log\mathcal{D}}{d\log N} \tag{2.22}$$

where the minus sign is used to have a positive quantity, since $d\log N$ is negative during the evaporation process.

The laser power of the cODT is controlled by exponential ramps, whose total duration and time constant are optimized empirically by maximizing the PSD at different steps of the evaporation. The PSD $\mathcal{D}$ is plotted as a function of the atom number N during the evaporation on figure 2.8, as well as the collision rate γ_{coll} during the second half of the evaporation. As expected the atom number decreases while the PSD increases which is the principle of evaporative cooling. The collision rate decreases over time since the optical trap opens progressively as the laser power is lowered, yet the fitted evaporation efficiency remains constant at a value $\chi = 3.6(4)$. The grey shaded region corresponds to the threshold of Bose-Einstein condensation, occurring for $\mathcal{D} \geq \zeta(3) \simeq 1.2$.

In practice we may not have to use BECs to perform experiments, in which case the evaporation ramp is interrupted before the condensation threshold. This allows us to save atoms if very low temperatures are not required, which increases the signal-to-noise ratio of absorption images. This is precisely the case in the next chapter where cold thermal clouds are used.

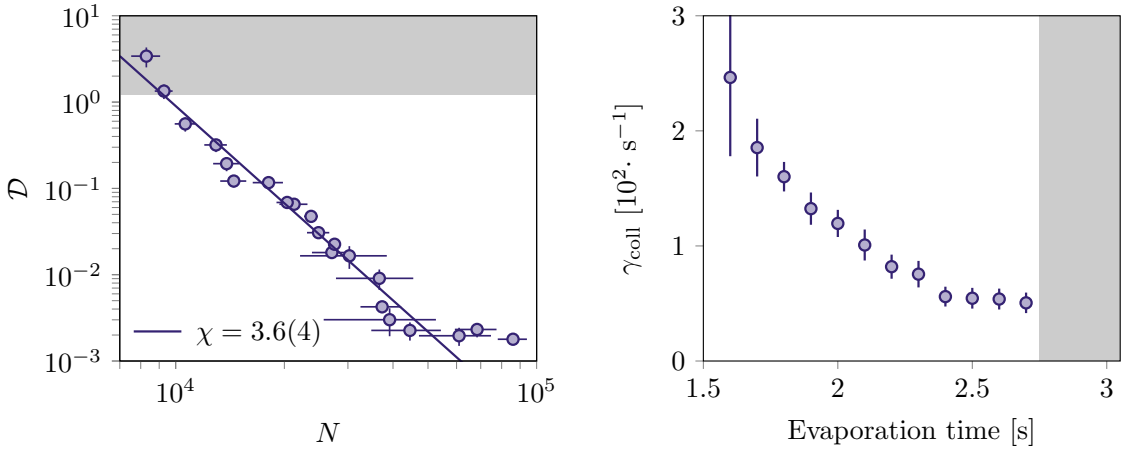

Figure 2.8 – **(Left) Evaporation efficiency**. The graph should be read from right to left to follow the evolution during the evaporation. The solid blue line is a fit of the data, not taking into account the first few points where the PSD does not increase. The grey region corresponds to the BEC threshold. **(Right) Collision rate as a function of time** corresponding to the data points plotted on the left. Equation 2.21 is no longer valid in the grey region corresponding to the condensation threshold.

Part II

Sensitivity of squeezed and non-gaussian spin states

Chapter 3

Spin squeezing and quantum-enhanced sensing

This chapter describes how the spin couplings induced by the light-shift operator close to resonance are used to prepare spin-squeezed states within the ground state Zeeman manifold $|J = 8, m_J = -8, ..., 8\rangle$. These techniques are similar to the ones used to manipulate the hyperfine spin states of cesium in [66]. The Bloch sphere representation is introduced in the usual way for a spin 1/2 and generalized to an arbitrary spin J, in which case a state can be represented by its *Husimi function*. In particular the notion of *coherent spin state* (CSS) plays a central role in this representation.

We define the *standard quantum limit* (SQL) as a reference of sensitivity allowing us to introduce the notion of metrological gain which is the usual figure of merit to characterize the sensitivity of a state. It is related to the contrast of Ramsey fringes to some extent, with some limitations that are developed in chapter 4.

Squeezed states exhibit reduced variance in a specific direction and are therefore of particular interest when it comes to sensing. The first squeezed states of light were obtained experimentally in 1985 [67] and have been recently used to increase the sensitivity of gravitational waves interferometers [68]. We present the *one-axis twisting* (OAT) Hamiltonian along with its use in the experimental preparation of spin squeezed states, using tensor light-shifts. Different techniques such as cavity feedback [69] or squeezing realized by atomic interactions [70] can also be used to prepare spin squeezed states. We measure the purity of the prepared states and show that squeezed states indeed exhibit an enhanced metrological gain. We also provide a reconstruction of their Husimi function.

The enhanced sensitivity that we present in this thesis relies entirely on the large spin $J = 8$ of dysprosium. Some of the sensitivity measurements and observables considered here have been experimentally realized with ultracold ions for a spin $J = 1/2$ in [71]. Even though we work with atomic clouds for good contrast and averaging, the physical effects at play are only 'single-atom'. This guarantees robustness to decoherence [31] compared to systems where a large spin $J = Nj$ is built from an ensemble of atoms (or ions) with individual spin j. It is well known that Schrödinger-cat states, which are coherent superpositions of macroscopic states, are extremely sensitive to decoherence and therefore difficult to realize experimentally.

We are able to prepare a superposition of the states $|J, m_J = +J\rangle$ and $|J, m_J = -J\rangle$ which can be considered as a cat state since $J = 8$ is quite large. However since the corresponding Hilbert space is of dimension $2J + 1$ (linear scaling with J), it constitutes a simpler version of cat states than those constituted by N entangled qubits, with an exponential scaling of the dimension 2^N. Schrödinger-cat states with up to 20 qubits have been prepared with arrays of Rydberg atoms trapped in optical tweezers [72]. Our work naturally extends to systems constituted of a single spin with a large number of internal states such as ultracold molecules [73].

3.1 Magnetic field sensitivity and metrological gain with a spin J

The Bloch sphere is a commonly used way to represent a spin 1/2 that we briefly recall. A general state $|\psi\rangle$ is decomposed in the m_z basis $|-1/2\rangle = |\downarrow\rangle$, $|1/2\rangle = |\uparrow\rangle$ according to

$$|\psi\rangle = \cos(\theta/2)\,|\uparrow\rangle + \sin(\theta/2)\,e^{i\phi}\,|\downarrow\rangle \tag{3.1}$$

where the angles θ and ϕ span the unit sphere.

This way of writing ψ leads to the following expression for the density matrix $\rho = |\psi\rangle\langle\psi|$,

$$\rho = \frac{1}{2}\left(\mathbb{1} + \boldsymbol{r}\cdot\hat{\boldsymbol{\sigma}}\right) \tag{3.2}$$

where $\boldsymbol{r}$ =$(\sin\theta\cos\phi,\ \sin\theta\sin\phi,\ \cos\theta)$ is the vector representing $|\psi\rangle$.

This parametrization is of particular interest when describing the evolution of a spin 1/2 in a magnetic field. The Hamiltonian is $\hat{H} = -(\gamma\hbar/2)\boldsymbol{B}\cdot\hat{\boldsymbol{\sigma}}$ where the $\hat{\sigma}_i$ are the Pauli matrices and γ is called the gyromagnetic factor. The Schrödinger equation for the density matrix

$$i\hbar\frac{d\rho}{dt} = \left[\hat{H}, \rho\right], \tag{3.3}$$

using the formula $(\boldsymbol{a}\cdot\hat{\boldsymbol{\sigma}})(\boldsymbol{b}\cdot\hat{\boldsymbol{\sigma}}) = (\boldsymbol{a}\cdot\boldsymbol{b})\,\mathbb{1} + i\,(\boldsymbol{a}\wedge\boldsymbol{b})\cdot\hat{\boldsymbol{\sigma}}$, reduces to

$$\frac{d\boldsymbol{r}}{dt} = -\gamma\boldsymbol{B}\wedge\boldsymbol{r} \tag{3.4}$$

which is precisely the equation governing the precession of a classical magnetic moment in a magnetic field. This is what makes the Bloch sphere representation a useful and intuitive tool to represent states of a spin 1/2.

3.1.1 Representing states of a spin J on the Bloch sphere

To generalize the representation on a sphere for any state of a spin J, the notion of coherent spin states is required. Let us introduce the algebra of angular momentum (or spin) operators $\hat{J}_x$, $\hat{J}_y$, $\hat{J}_z$ satisfying the commutation relation

$$[\hat{J}_x, \hat{J}_y] = i\hat{J}_z \tag{3.5}$$

and the other two obtained by circular permutation of the x, y, z indices. The 2J+1-dimensional basis of the joint eigenstates of $\hat{\boldsymbol{J}}^2$ and $\hat{J}_z$ (where the z direction can be

chosen arbitrarily) is formed by the Dicke states $|J,m\rangle_z$ for $m = -J, -J+1, ..., J-1, J$. The z subscript is usually dropped for simplicity but it can be necessary in the case of basis changes. The $|J,m\rangle_x$ basis for example will also be used in convenient cases.

The Dicke states are similar to the Fock states in quantum optics, as they obey the same 'ladder' behaviour with

$$\hat{J}_\pm |J,m\rangle = \sqrt{J(J+1) - m(m\pm 1)}\, |J, m\pm 1\rangle \tag{3.6}$$

where $\hat{J}_\pm = \hat{J}_x \pm i\hat{J}_y$.

Coherent spin states

A coherent spin state that we write $|\theta,\phi\rangle$ is an eigenstate of the rotated spin operator $\hat{J}_{\theta,\phi} = \sin\theta\cos\phi\,\hat{J}_x + \sin\theta\sin\phi\,\hat{J}_y + \cos\theta\hat{J}_z$ with eigenvalue J. Such a state can also be referred to as a *classical state* since it is analogous to a classical magnetic dipole pointing in the direction (θ,ϕ). It can be decomposed in the Dicke basis according to [74]

$$|\theta,\phi\rangle = \sum_{m=-J}^{J} \sqrt{\binom{2J}{J-m}} \left(\sin\frac{\theta}{2}\right)^{J-m} \left(\cos\frac{\theta}{2}\right)^{J+m} e^{-i(J+m)\phi} |J,m\rangle \tag{3.7}$$

Now for a given state $|\psi\rangle$ of the spin J, one can define its Husimi function $Q_\psi(\theta,\phi)$ as

$$Q_\psi(\theta,\phi) = |\langle\psi|\theta,\phi\rangle|^2 . \tag{3.8}$$

The value of Q_ψ at position (θ,ϕ) is nothing but the overlap between the CSS $|\theta,\phi\rangle$ and the state $|\psi\rangle$.

The explicit computation of the Husimi function of a CSS $|\theta_0,\phi_0\rangle$ is tractable and yields

$$|\langle\theta_0,\phi_0|\theta,\phi\rangle|^2 = \frac{1}{2^{2J}}\Big[1+\cos(\theta-\theta_0) - \sin\theta\sin\theta_0\big[1-\cos(\phi-\phi_0)\big]\Big]^{2J} \tag{3.9}$$

While this expression is not obvious at first sight, an expansion for θ close to θ_0 and ϕ close to ϕ_0 can be performed to get

$$|\langle\theta_0,\phi_0|\theta,\phi\rangle|^2 \sim \left[1 - \frac{(\theta-\theta_0)^2}{4} - \sin^2\theta_0\frac{(\phi-\phi_0)^2}{4}\right]^{2J} \tag{3.10}$$

$$\sim \exp\left[-\frac{J}{2}\left[(\theta-\theta_0)^2 + \sin^2\theta_0\,(\phi-\phi_0)^2\right]\right] \tag{3.11}$$

which is a gaussian shape of width $\sigma \sim 1/\sqrt{J}$ represented on figure 3.1. This can be understood from the fact that the exponent $2J = 16$ strongly damps the Husimi function away from its maximum. Representing a state by its Husimi function on a sphere constitutes the generalized Bloch sphere representation. The remaining factor $\sin^2\theta_0$ is an artifact of the spherical coordinates.

The average magnetization $m_z = \langle\theta,\phi|\hat{J}_z|\theta,\phi\rangle$ of a CSS is equal to $J\cos\theta$ as expected from its graphical representation.

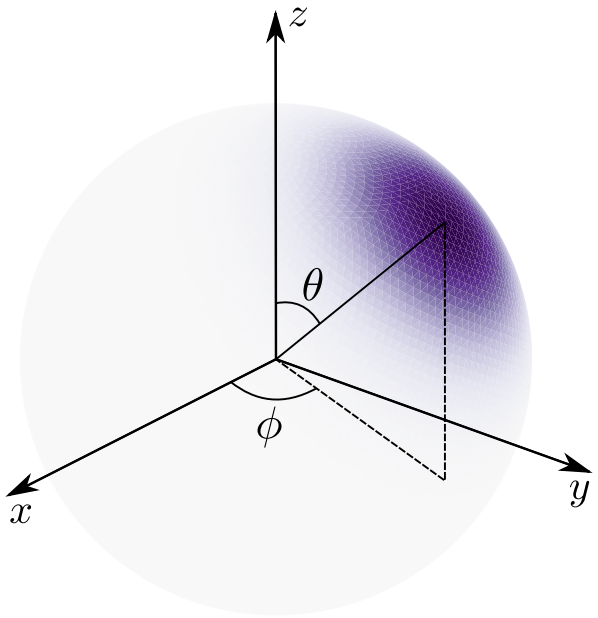

Figure 3.1 – Husimi function of a CSS for a spin $J = 8$, centered on the direction (θ, ϕ) on the generalized Bloch sphere.

A CSS $|\theta, \phi\rangle$ is a gaussian state in the sense that it saturates the Heisenberg uncertainty principle

$$\Delta J_u \Delta J_v \geq \frac{\left|\left\langle [\hat{J}_u, \hat{J}_v] \right\rangle\right|}{2} = \frac{\left|\langle \hat{J}_{\theta,\phi} \rangle\right|}{2} = \frac{J}{2} \tag{3.12}$$

where $\boldsymbol{u}$ and $\boldsymbol{v}$ are two orthogonal directions in the plane orthogonal to (θ, ϕ). This leads to $\Delta J_u = \sqrt{J/2}$ for any direction $\boldsymbol{u}$ orthogonal to (θ, ϕ).

The size $\sigma \sim 1/\sqrt{J}$ of the Husimi function of a CSS is related to the fact that the Bloch sphere has a radius J such that the apparent size of the Husimi function is $\Delta J/J \sim 1/\sqrt{J}$.

A coherent state $|\theta, \phi\rangle$ can be defined as the action of a rotation operator $\hat{\mathcal{R}}(\theta, \phi)$ acting on the maximal state $|J, J\rangle$ as [75]

$$|\theta, \phi\rangle = \hat{\mathcal{R}}(\theta, \phi)\,|J, J\rangle = \exp\left[\theta\,(e^{-i\phi}\hat{J}_+ - e^{i\phi}\hat{J}_-)\right]|J, J\rangle \tag{3.13}$$

in a similar way to the definition of a coherent state of the electromagnetic field $|\alpha\rangle$ as the displacement operator $\hat{\mathcal{D}}(\alpha)$ acting on the vacuum $|0\rangle$.

Dicke states

The Husimi function of a Dicke state is

$$|\langle J, m|\theta, \phi\rangle|^2 = \frac{1}{2^{2J}}\binom{2J}{J-m}(1-\cos\theta)^{J-m}\,(1+\cos\theta)^{J+m} \tag{3.14}$$

and we see that it has no ϕ dependence. A quick computation of the derivative shows that the Husimi function is maximal on a line of equation $J\cos\theta = m$ which

is a parallel of the sphere. The Husimi function indeed corresponds to a ring on the Bloch sphere as shown on figure 3.2.

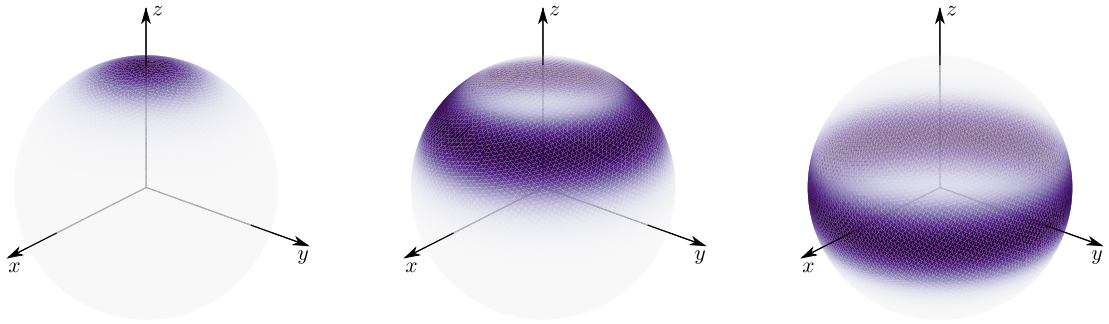

Figure 3.2 – Husimi function of three Dicke states for $J = 8$. Note that the upper Dicke state $m = 8$ is also a CSS corresponding to the vertical direction, pointing up, while $m = -8$ would be pointing down.

3.1.2 Rotations and magnetic field sensitivity

The effect of a magnetic field pointing along z on a CSS can be easily computed. The time-independent Hamiltonian $\hat{H} = g_J \mu_B \boldsymbol{B} \cdot \hat{\boldsymbol{J}} = g_J \mu_B B \hat{J}_z$ leads to a unitary evolution operator $\hat{U}(t) = \exp(-i\omega t \hat{J}_z)$ with $\omega = g_J \mu_B B/\hbar$. The state evolves according to

$$\hat{U}(t) \left|\theta_0, \phi_0\right\rangle = e^{iJ\omega t} \left|\theta_0, \phi_0 + \omega t\right\rangle \tag{3.15}$$

which is a CSS precessing around the vertical axis with angular velocity ωt as depicted on figure 3.3. The global phase factor does not play a significant role and disappears when computing the Husimi function. This result is valid for any magnetic field since we can always perform a basis change mapping the z-axis onto the direction of the magnetic field. We recover the same behaviour as for a spin 1/2 on the Bloch sphere. This is another reason why the generalized Bloch sphere representation is useful and intuitive.

The notion of magnetic field sensitivity of a spin state is related to how much it rotates on the Bloch sphere under the influence of a magnetic field. The smallest magnetic field that can be measured over a duration τ is related to the smallest displacement $J\delta\phi = J\omega\tau$ that can be resolved on the sphere. If $J\delta\phi$ is larger than the width of the state ΔJ then the state displacement can be resolved. If it is smaller, then the spread of the state hides the displacement. This effect is visible on figure 3.3.

As previously described a Dicke state is invariant along ϕ and is therefore invariant under the application of a vertical magnetic field. This is to be expected from the fact that Dicke states are eigenstates of $\hat{J}_z$. The magnetic field sensitivity intuitively corresponds to how much a state needs to change for a difference to be measurable.

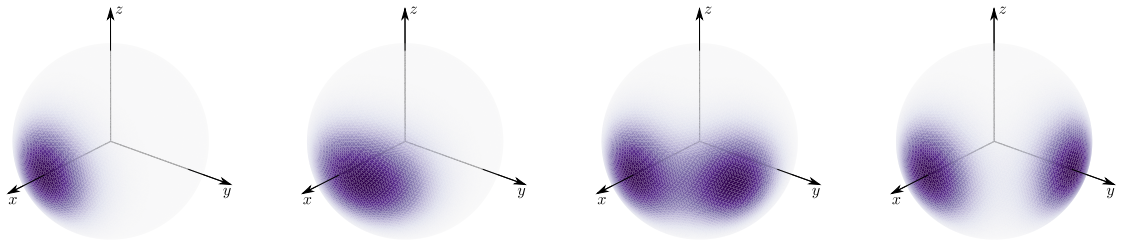

Figure 3.3 – Husimi functions of two CSS, the first one centered on x and the second one experiencing Larmor precession around the z-axis. They both have an average magnetization $m_z = 0$. The rotation angles are 0, $\pi/6$, $\pi/3$ and $\pi/2$ from left to right. The $\pi/6$ angle cannot be resolved precisely due to the intrinsic variance of the CSS whereas $\pi/3$ is clearly visible.

3.1.3 Sensitivity based on Ramsey oscillations

In order to quantify the sensitivity $\Delta\phi$ that can be attained from a general measurement corresponding to the operator $\hat{A}$ (depending on ϕ), we use the *method of moments* stating that [76]

$$\Delta\phi = \frac{\Delta\hat{A}}{\left|d\left\langle\hat{A}\right\rangle/d\phi\right|} \tag{3.16}$$

for a single measurement and a single probe.

For spin states, the experimentally accessible quantities are the populations of the different $|m\rangle_z$ states, through a Stern-Gerlach measurement. We drop the letter J in the kets since it will stay the same throughout the chapter. The z subscript will be omitted as well unless basis changes are involved. The rotation around z corresponding to the Larmor precession leaves the relative populations unchanged and therefore they do not depend on the angle ϕ.

The technique of Ramsey interferometry is well known in the context of spins 1/2 and also applies to any spin J. It has the advantage of mapping variations of ϕ onto variations of the populations along z and is therefore especially suited in this context. We assume that the initial state is a CSS on the north pole of the sphere. This is the situation usually found in experiments. A first $\pi/2$ rotation around y (note that it could also be any axis of the xy plane) brings the CSS on the equator of the sphere, on the x-axis. The first panel of figure 3.4 represents this state on the x-axis. It will precess for a given waiting time τ due to the presence of the external magnetic field along z. Then a $-\pi/2$ rotation around y brings the state away from the equator and turns the accumulated phase ϕ into a change of the azimuthal angle θ. This induces a change in populations as represented in figure 3.5. The population distributions are binomial according to equation 3.7, and have a gaussian shape far from the edges.

Using this technique and according to equation 3.16, the phase sensitivity is then

$$\Delta\phi = \frac{\Delta J_z}{|dm_z/d\phi|} \tag{3.17}$$

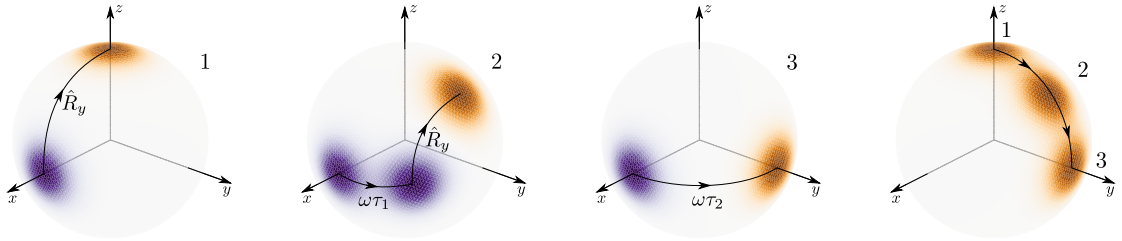

Figure 3.4 – Scheme illustrating Ramsey oscillations. From left to right (1, 2 and 3), three different precession times $0, \tau_1, \tau_2$ (in blue) followed by a $-\pi/2$ rotation $\hat{R}_y$ around y-axis (in orange). On the third panel the state is brought onto the x-axis by Larmor precession and remains invariant under $\hat{R}_y$. The fourth panel represents the final states (orange) obtained from the first three panels. It shows how the variations of ϕ on the equator are mapped into variations of the azimuthal angle θ.

where ΔJ_z is the variance along the vertical direction and m_z is the average magnetization along z. Intuitively a precise measurement corresponds to a small $\Delta\phi$, meaning a small variance ΔJ_z and a large 'change of m_z per change of ϕ'. Explicit computation of $\langle \hat{J}_z^2 \rangle$ is tractable and, together with the result $\langle \hat{J}_z \rangle = J \cos\phi$ previously derived (ϕ replaces θ thanks to the Ramsey rotations), yields $\Delta J_z = \sqrt{J/2} \sin\phi$ and finally $\Delta\phi = 1/\sqrt{2J}$.

This value corresponds to the *Standard Quantum Limit* (SQL). It is also referred to as classical limit in the sense that it is similar to the $1/\sqrt{N}$ reduction of uncertainty when averaging over the measurement outcomes of N uncorrelated probes. In this case $N = 2J$ corresponds to the fictitious $2J$ spins 1/2 combined to form a large spin J. This analogy will be developed in details in chapter 4.

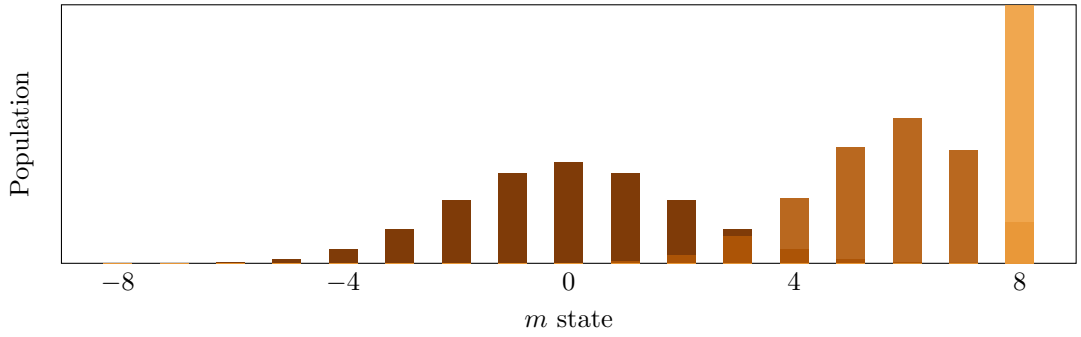

Figure 3.5 – Populations of the three CSS obtained during the Ramsey procedure (rightmost panel of figure 3.4). Three shades of orange, from light to dark, are used to represent the three successive states with $\theta = 0$, $\pi/4$ and $\pi/2$. $\theta = 0$ corresponds to only the upper m-state $m = 8$ being populated, while $\theta = \pi/2$ corresponds to $m_z = 0$ with a Husimi function located on the equator of the sphere.

3.2 Spin squeezing and enhanced sensitivity

From looking at figure 3.3, one can see how a 'narrower' state would lead to an increase of phase sensitivity. Such a state is called a *squeezed* state and is characterized by a reduced variance along one axis. It can be prepared using the one-axis twisting (OAT) Hamiltonian introduced for the first time in [37].

3.2.1 The one-axis twisting Hamiltonian

The OAT corresponds to the quadratic spin operator

$$\hat{H} = \hbar\chi \hat{J}_u^2 \tag{3.18}$$

where $\boldsymbol{u}$ is a unit vector defining any direction on the sphere and χ is a real parameter characterizing the coupling strength. We will always use the direction $\boldsymbol{u} = \boldsymbol{e}_x$ in the following as it is the axis used on the experimental setup.

We first describe the effect of the OAT on the initial state $|-J\rangle_z$. This is the initial state prepared experimentally as will be described later. The evolution is $2\pi/\chi$-periodic and the different populations along z are plotted for $J = 8$ in figure 3.6. Only the states with even m get populated because the initial state has even m and $\hat{J}_x^2 \propto (\hat{J}_+ + \hat{J}_-)^2$ changes m-states by increments of 2. It is not easy to follow the varying populations in all the 17 states at different times , but it can be better understood by expressing the states in the x-basis (by performing the right angle changes in equation 3.7), where the $\hat{J}_x^2$ operator has a simple effect. Indeed

$$\begin{aligned} |\psi(t)\rangle &= e^{-i\chi t\hat{J}_x^2} |-J\rangle_z \\ &= e^{-i\chi t\hat{J}_x^2} \frac{1}{2^J} \sum_{m=-J}^{J} \sqrt{\binom{2J}{J-m}} i^m |m\rangle_x \\ &= \frac{1}{2^J} \sum_{m=-J}^{J} \sqrt{\binom{2J}{J-m}} e^{i(m\pi/2 - m^2\chi t)} |m\rangle_x \end{aligned} \tag{3.19}$$

which is a superposition of terms oscillating at different frequencies. Such a situation leads to dephasing after a short time. In this case the timescale can be deduced from the magnetization m_z (second panel on figure 3.6). It experiences a collapse from the initial value $m_z = -J$ corresponding to the singly occupied state $|-J\rangle$, to zero corresponding to a superposition of all states. It can be shown [37] that

$$m_z(t) = -J\big[\cos(\chi t)\big]^{2J-1} \tag{3.20}$$

which for large J scales at short times as $\exp[-2J(\chi^2 t^2/2)]$. The associated collapse timescale is $1/(\chi\sqrt{2J})$.

The $2J+1$ oscillating terms come back in phase for $\chi t = \pi$ for which the resulting state is

$$|\psi(\pi/\chi)\rangle = \frac{1}{2^J} \sum_{m=-J}^{J} \sqrt{\binom{2J}{J-m}} i^m (-1)^m |m\rangle_x = |+J\rangle_z \tag{3.21}$$

and is clearly visible with a maximum of the magnetization at $\chi t = \pi$.

Another simple quantum state occurs at $\chi t = \pi/2$ and is visible with a peak of the variance to its maximal value $\Delta \hat{J}_z^2 = 64$. This situation corresponds to the two extremal states $|-J\rangle_z$ and $|+J\rangle_z$ being equally populated. Indeed

$$|\psi(\pi/2\chi)\rangle = \frac{e^{-i\pi/4}}{\sqrt{2}}(|-J\rangle_z + i\,|+J\rangle_z) \tag{3.22}$$

is a coherent superposition of these two states which can be called Schrödinger-cat state, GHZ state [77] or N00N state [78]. The second half of the period is identical to the first half and we recover the initial state $|-J\rangle_z$ at the end.

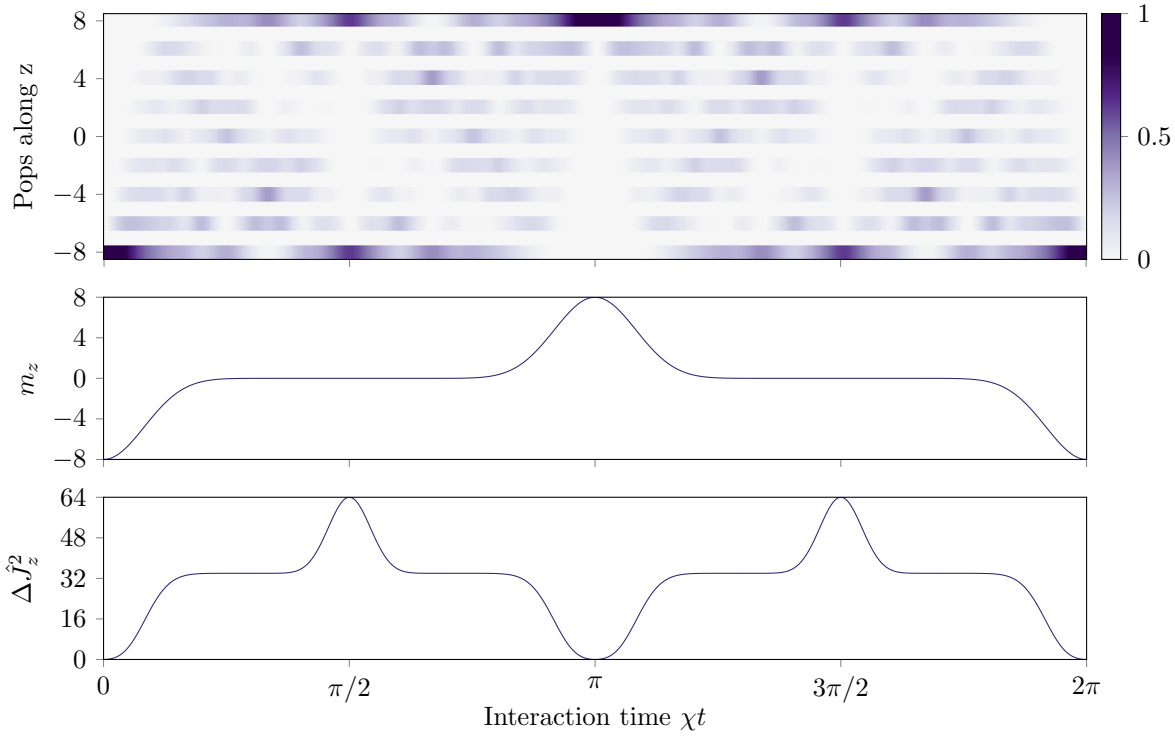

Figure 3.6 – Evolution over one period of the OAT. We first plot the populations as a function of time. A 'vertical slice' of this color plot at a given time is a population histogram similar to the ones of figure 3.5. From the populations $\Pi_m(z)$ along z, the mean m_z and variance $\Delta \hat{J}_z^2$ are computed as $m_z = \sum_m m\,\Pi_m(z)$ and $\Delta \hat{J}_z^2 = \sum_m m^2\,\Pi_m(z) - m_z^2$.

3.2.2 Squeezing parameter

At this stage the squeezing is not apparent yet. The squeezing parameter ξ_R if the figure of merit usually used to characterize the amount of squeezing. It is defined as [79]

$$\xi_R = \sqrt{2J}\frac{\Delta J_{\min}}{|m_z|} \tag{3.23}$$

where $\Delta J_{\min}$ is the minimal variance in the xy plane.

For a CSS along the z direction, we have $|m_z| = J$ and $\Delta J_{\min} = \sqrt{J/2}$ such that $\xi_R = 1$.

In terms of magnetic field sensitivity, ξ_R can be related to the smallest displacement that can be measured on the sphere in a similar way to figure 3.3. We now have

$$\Delta\phi_{\min} = \frac{\Delta J_{\min}}{|m_z|} = \frac{\xi_R}{\sqrt{2J}} = \xi_R \, \Delta\phi_{\mathrm{SQL}}. \tag{3.24}$$

This leads to the notion of *metrological gain* G_R defined as

$$G_R = \left(\frac{\Delta\phi_{\mathrm{SQL}}}{\Delta\phi} \right)^2 \tag{3.25}$$

which for spin squeezing satisfies

$$G_R = 1/\xi_R^2. \tag{3.26}$$

We plot on figure 3.7 the minimal and maximal variance in the xy plane as well as the metrological gain and the 'gaussianity' of the prepared state as a function of the interaction time χt. This is the result of numerical simulations. We observe a reduction of the minimal variance below 4 (the value for the initial coherent state) at short times while the maximal variance increases to satisfy the Heisenberg uncertainty principle. The squeezing is associated to an increase of the metrological gain with a maximum at $\chi t_s \simeq 0.15$. This optimally squeezed state minimizes ξ_R.

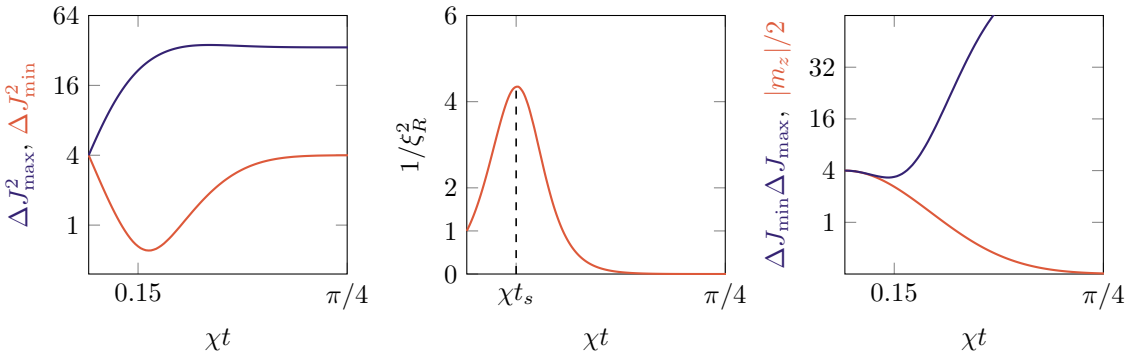

Figure 3.7 – Manifestation of the squeezing at short times. We restrict the plot to short times up to $\chi t = \pi/4$ since the interesting changes occur during the collapse timescale $\chi t \sim 1/\sqrt{2J}$. Note that the maximum of G_R does not occur exactly at the same time as the minimal variance. The maximal variance reaches a plateau at $J(J+1/2)/2 = 34$ in the oversqueezed regime [80].

At longer times, the metrological gain collapses as the minimal variance reaches an asymptotic value of $J/2 = 4$ and the average magnetization along z goes to zero. This region corresponds to *oversqueezed* states, a word introduced for the first time in [81]. This category of states had already been studied in [69] and [82]. In this regime the prepared state ceases to be gaussian as can be seen from the

comparison between the product of uncertainties $\Delta J_{\min}\Delta J_{\max}$ and $|m_z|/2$. The Heisenberg uncertainty principle is no longer saturated which means that the states become non-gaussian.

Note that for the cat state, prepared at $\chi t = \pi/2$, the magnetization along z is equal to zero as plotted on figure 3.6, which means that the gain G_R computed from the squeezing parameter (equation 3.26) is $G_R = 0$. However the cat state is the one with the highest magnetic field sensitivity in the entire manifold [83]. This is true if the sensitivity is extracted from an experimental sequence that is different from Ramsey interferometry and the metrological gain defined in this chapter cannot account for it. It is also the case for the oversqueezed states which indeed have a sensitivity worse than a CSS in the case of Ramsey interferometry ($G_R < 1$) but in fact exhibit higher sensitivity for a different experimental protocol. These two specific cases are described in chapter 4.

3.3 Experimental realization of the OAT

We now present the experimental realization of spin-squeezed states using ultracold clouds of dysprosium. Off-resonant light at 626 nm is used to induce quadratic spin coupling in a similar way to [66]. Arbitrary rotations of the prepared state can be performed using magnetic field pulses. Finally the spin composition of the cloud can be determined by a Stern-Gerlach measurement. The Husimi function of the prepared states as well as their purity can be deduced from population measurements. Their magnetic sensitivity is measured from Ramsey oscillations or equivalently from computing the squeezing parameter ξ_R.

3.3.1 State preparation and readout

We work with cold gases of typically 10^5 atoms at a temperature of 1.1 µK. Note that these are ultracold thermal clouds, not BECs. The specific features of BECs are not required here and the compromise between low temperature (to resolve the different spin states) and large atom number (for good absorption imaging contrast) of the evaporation process led to the numbers mentioned here. The cloud is initially polarized in the $|-8\rangle_z$ state thanks to the value of the vertical quantization field of 0.5 G used during the evaporative cooling stage. It is ramped down in typically 50 ms to a value of 60 mG which still corresponds to a Zeeman splitting of 5 µK. This value is chosen to have a defined quantization axis while limiting thermal excitations to higher m-states. We present the experimental setup on figure 3.8 and the steps used to prepare and measure spin states. These various steps can also be separately used as calibration tools presented afterwards.

Light pulse to induce one-axis twisting

The OAT dynamics is induced by a pulse of light close to the 626 nm transition. The duration and amplitude of the pulse is controlled by an AOM with a rising time of typically 100 ns and the laser beam is focused at the position of the atoms with a waist of 50 µm and available power above 1 W. The cODT is turned off before the light pulse is sent on the atomic cloud. The effect of gravity and thermal expansion on its vertical position and size (a few µm) are not significant over the duration of

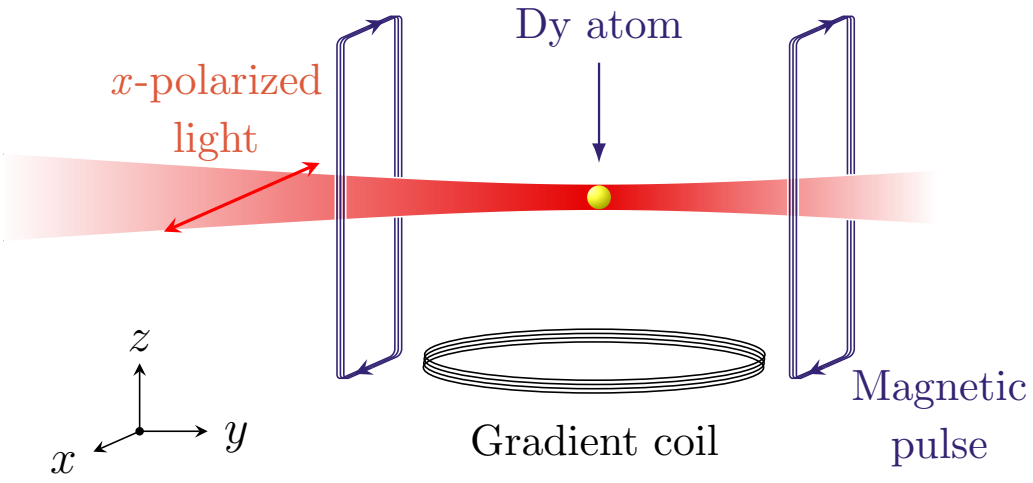

Figure 3.8 – Scheme of the experimental setup for one-axis twisting.

the spin dynamics (µs timescale). This allows us to neglect inhomogeneous coupling over the spatial extension of the atomic cloud.

The light is linearly polarized along x which according to equation 1.7 leads to the presence of a $\hat{J}_x^2$ term and the absence of vector light-shift. The scalar term corresponds to an overall m-independent energy term which has no effect on the spin dynamics. The Hamiltonian therefore reduces to

$$\hat{H} = \hbar\omega_Z \hat{J}_z + \hbar\chi \hat{J}_x^2 \quad \text{with} \quad \chi = -\frac{1}{(J+1)(2J+1)} \frac{3\pi\Gamma c^2}{2\omega_0^3} \frac{I}{\Delta} \tag{3.27}$$

where $\omega_Z = g_J \mu_B B/\hbar$ corresponds to the presence of a vertical magnetic field. The value of $B = 60$ mG specified above ensures that the Zeeman term remains small compared to χ. The associated Larmor rotation is typically 3° over the duration of the light pulse (a few 100 ns) and is therefore neglected. Therefore the light pulse realizes the OAT Hamiltonian almost ideally.

Note that the rising time of the AOM and the total duration of the light pulse are of the same order of magnitude. This results in a pulse shape (figure 3.10) which is not rectangular but rounded. The interaction time χt introduced in the previous section is proportional to the integrated pulse and is extracted numerically. The detuning Δ is chosen to be $2\pi \times -1.1$ GHz which leads to a power-tunable value of $\chi = 1 - 10\,\mu\text{s}^{-1}$.

Magnetic pulses to induce rotations

Rotations around the y-axis can then be performed by sending current pulses of various durations in the coils placed laterally around the cell. The goal is to be able to bring a state from the pole of the Bloch sphere to the equator as described in the previous section with the Ramsey sequence. The magnetic pulse consists in changing the direction of the magnetic field over a short duration (typically 3 µs) so that the Larmor precession is tilted and brings the state away from the pole as described on figure 3.9.

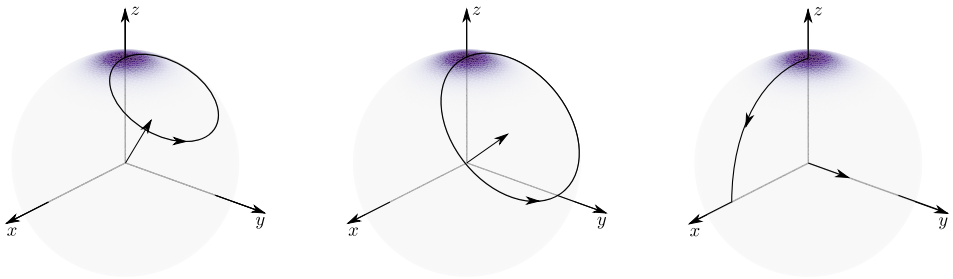

Figure 3.9 – Rotations corresponding to magnetic pulses of different strengths. From left to right, B_y increases while the value of B_z remains constant, with the extreme case $B_y \gg B_z$ corresponding to the ideal $\pi/2$ rotation on the right. In the first case the pulse is not strong enough to bring the state to the equator and cannot be used in a Ramsey sequence. One can see that to reach the equator, the total magnetic field needs to have an angle of at least 45° with respect to the vertical direction.

The case of an ideal $\pi/2$-pulse corresponds to a field B_y much larger than B_z producing a rotation around the y-axis. However the technical limitations of the power amplifier used on the experiment only allow for an imperfect $\pi/2$ pulse. The state rotates around a tilted axis between z and y and therefore acquires a phase ϕ when brought on the equator. With the value $B_z = 60$ mG previously mentioned, we measure an offset phase of 1.94 radians that we take into account in the analysis when speaking of a $\pi/2$ rotation. This offset is never an issue when performing a Ramsey sequence.

Rotations around z naturally occur due to the Larmor precession induced by the quantization field. A magnetic field of 60 mG corresponds to a Larmor period of 9.6 µs. We can therefore perform arbitrary rotations on the Bloch sphere by combining active rotations (pulses) around y and passive rotations (waiting times) around z.

Stern-Gerlach state readout

The populations along z are measured by a Stern-Gerlach experiment. A magnetic field gradient is applied during a few milliseconds and induces a force

$$F_m = -m_J \, g_J \, \mu_B \nabla B. \tag{3.28}$$

which linearly depends on m_J. It separates the atomic cloud in up to seventeen smaller clouds, corresponding to the different m-states. Two consecutive m-state clouds are visibly distinguishable if their thermal expansion remains smaller than the distance between them. This is achieved with a field gradient of around 50 G/cm and a temperature of a few µK.

Absorption imaging leads to optical densities of the m-state clouds proportional to the relative atom numbers in each of these states. Gaussian fits of the clouds allow us to retrieve the relative populations by normalizing to the total atom number. An example of single-shot pictures is given on figure 3.10.

This measurement projects each atomic state of the form $|\psi\rangle = \sum_m \alpha_m \, |m\rangle_z$ on the state $|m\rangle_z$ with probability $\Pi_m = |\alpha_m|^2$. Since there are 10^5 atoms, the number

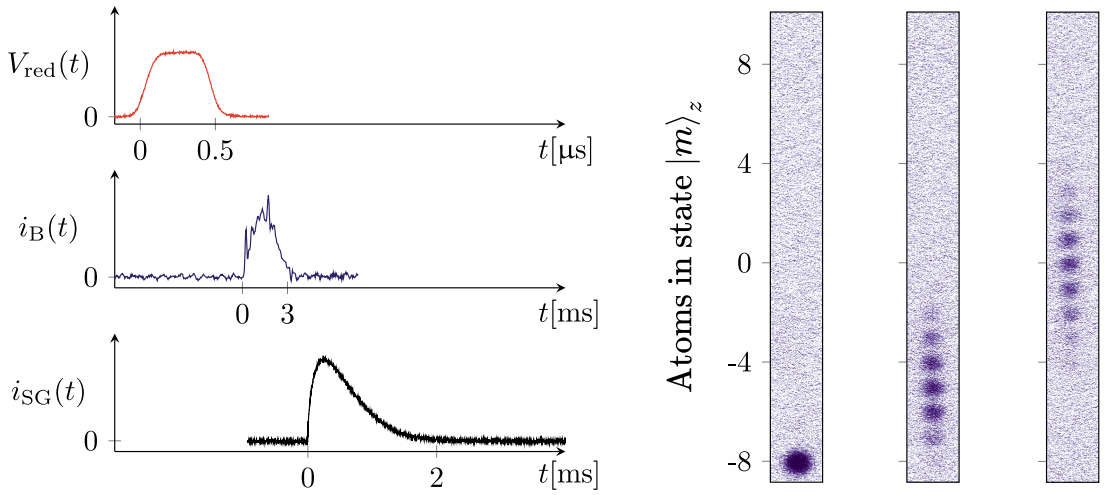

Figure 3.10 – Experimental sequence for state preparation and examples of single-shot pictures for three CSS. (Left) The three traces correspond to the recorded red laser power on a photodiode, the recorded intensity corresponding to the rotation pulse and finally the Stern-Gerlach pulse. The timescales are not identical for the three traces. These are the essential ingredients used to prepare and probe states. The rotation stage can be more complicated with additional pulses and well-chosen waiting times. **(Right)** The three states correspond to average magnetizations $m_z = -8$, $m_z = -5$ and $m_z = 0$. The ground state $m = -8$ is the initial state in all our experiments, the other two are obtained after performing magnetic rotations of different durations. Pulses of red light were *not* used to prepare these three states.

of atoms N_m found in each single-m cloud is directly proportional to Π_m according to

$$N = \sum_m N_m \quad \text{and} \quad \Pi_m = \frac{N_m}{N}. \tag{3.29}$$

By combining this measurement along z with arbitrary rotations mapping a direction $\hat{\mathbf{n}}$ onto z, we have access to the populations $\Pi_m(\hat{\mathbf{n}})$ for any direction $\hat{\mathbf{n}}$. From this measurement only, one cannot distinguish a superposition state from a statistical mixture. However the purity of the states can be inferred from population measurements along various directions, as described in section 3.3.2

Atom number calibration

The difference with standard absorption imaging described by equation 1.14 is that the scattering cross section depends on m through the Clebsch-Gordan coefficients of the $J = 8 \rightarrow J' = 9$ transition (at 421 nm). Therefore we need to take these coefficients into account in order to extract unbiased populations. Note that the imaging pulse also need to be short enough so that it does not induce optical pumping resulting in a transfer between the different m-states.

The cross section calibration is achieved by performing a sequence that populates all the states while keeping the total atom number constant. The Ramsey sequence is especially suited in this case as we do not expect magnetic rotations to induce m-dependent losses. We know that the total atom number should be independent from m if the different coefficients are well chosen. We perform a fit of these 17 coefficients to minimize the variance of the total atom number and get the result plotted on figure 3.11. We observe a symmetric behaviour for the fitted coefficients consistent with the fact that we use linearly polarized light to image the atoms. The Clebsch-Gordan coefficients $c_{m,q}$ indeed satisfy $c_{-m,-q} = c_{m,q}$ where $q = -1, 0, 1$ stands for σ_-, π and σ_+ polarizations. The additional visible tilt can be attributed to slightly non uniform light intensity over the extension of the single-m clouds. This method has the advantage of correcting experimental imperfections as well as the physical imaging bias.

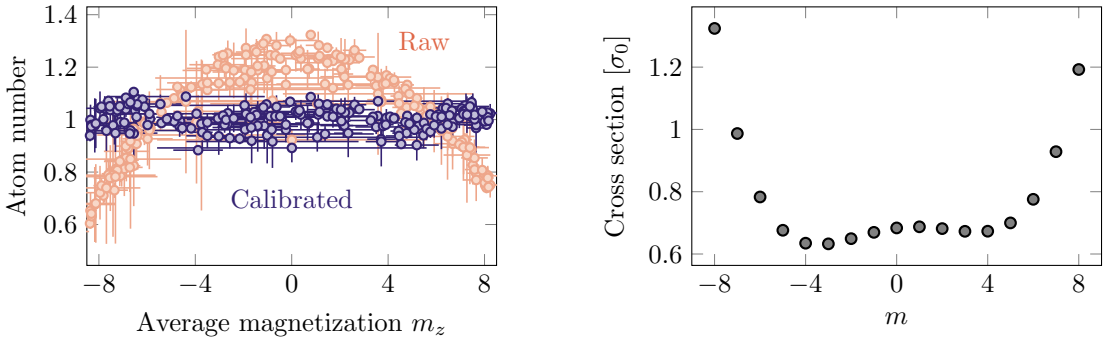

Figure 3.11 – Calibration of the m-dependent cross sections. (Left) Total atom number as a function of the average magnetization m_z during a Ramsey sequence, without calibration (light red), and with corrections (blue). The atom number is normalized to 1 for the calibrated coefficients. **(Right)** Calibrated cross sections for the different m-states.

Alignment of the quantization field

The magnetic field gradient direction is physically set by the way the coil is placed below the glass cell and therefore cannot be changed. This is what sets the vertical direction in practice. The direction of the magnetic field used as a quantization axis is then aligned on it by imaging coherent states.

We know that the atomic cloud is initially polarized in the $|-8\rangle_u$ state where $\boldsymbol{u}$ is the direction of the magnetic field. If $\boldsymbol{u}$ coincides with z, we should image only a single cloud corresponding to the state $|-8\rangle$. If the two directions are different, several m-states will be populated in the spirit of figure 3.10. Scanning the transverse magnetic field generated by the coils along x and y and minimizing the magnetization m_z down to -8 allows us to align the quantization field on the measurement axis.

3.3.2 OAT evolution, purity and squeezing parameter

We now present the experimental results published for the most part in [84].

Implementation of the OAT

Using the tools presented here, we can engineer the one-axis twisting Hamiltonian and probe the prepared states. We focus on the short-time evolution i.e. the squeezing strictly speaking. We are able to experimentally reproduce the graphs of figure 3.7 that we plot on figure 3.12 for $\chi t < 0.5$.

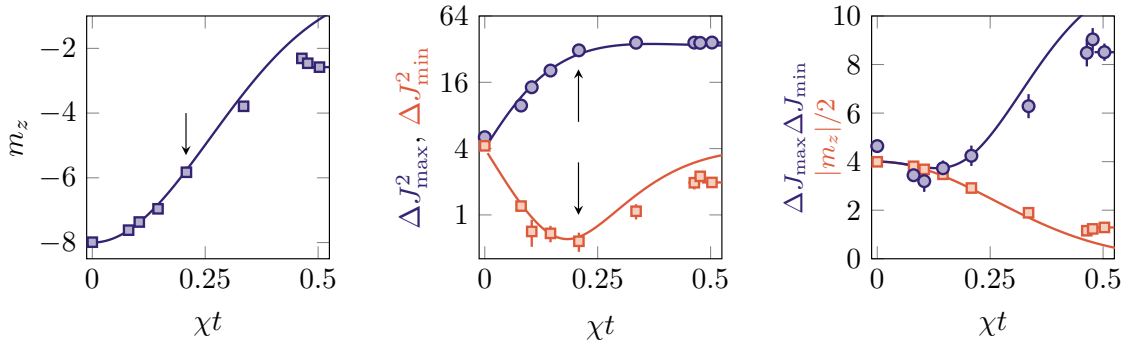

Figure 3.12 – Magnetization and variance measurements. (Left) Mean magnetization m_z as a function of the interaction time χt. **(Center)** Minimal and maximal variance in the xy plane. **(Right)** Uncertainty product and lower bound of the Heisenberg uncertainty principle $|m_z|/2$. Solid lines correspond to the OAT predictions. Arrows point at the values corresponding to the data obtained for the state represented in figure 3.13.

We indeed observe a reduction of the minimal variance in the xy plane i.e. spin squeezing, in good agreement with the predictions of the OAT. There is an increasing difference between experimental results and theory for data points at times longer than $\chi t = 0.25$ that we attribute to the $\hat{J}_z$ term in the Hamiltonian. Its effect gets visible as the interaction time increases.

The only fitted quantity is the overall scaling of the x axis as the coupling χ is proportional to the power of the laser beam used to induce the $\hat{J}_x^2$ coupling at the position of the atoms. This is a quantity that we cannot accurately measure because of the small absorption caused by the sides of the glass cell. The value of χ was also subject to daily recalibration, as the laser beam can drift away from the position of the atoms and its total power also drifts over days (because of small alignment drifts building up in the optical setup). By measuring the mean magnetization m_z for a few states as plotted on the left panel of figure 3.12 and comparing it with the predictions of the OAT, we can calibrate χ before any data acquisition.

The successive steps used to measure the minimal and maximal variance in the xy plane are represented in figure 3.13. We measure for a squeezed state the populations $\Pi_m(\hat{\mathbf{n}})$ for $\hat{\mathbf{n}}$ in the xy plane to extract the squeezing direction $\phi_{\min}$.

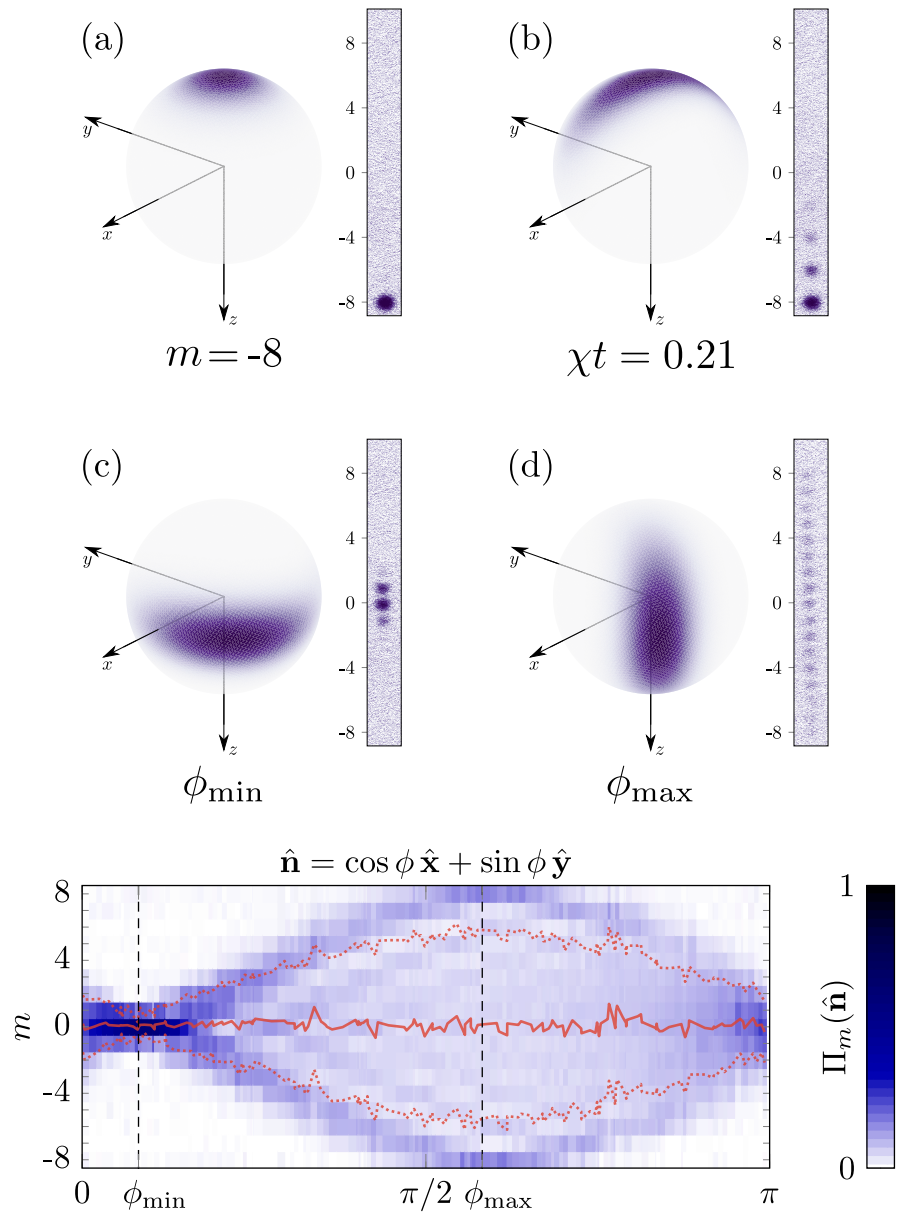

Figure 3.13 – Experimental steps used to measure the minimal and maximal variance in the xy plane for a squeezed state. Since the initial state $|-8\rangle_z$ is oriented along the direction $-z$, we choose to represent the z-axis pointing down for an easier visualization **(a)** . After preparing a squeezed state **(b)**, an additional waiting time induces a rotation with respect to the z-axis, on top of the sphere (not represented here). It is followed by a rotation bringing the state to the equator, which allows a mapping of the variance in the xy plane to the z-axis. By adjusting the waiting time during which the state rotates about z, one can change ϕ and vertically align the squeezed state along its minimal **(c)** or maximal **(d)** variance. The Husimi functions shown here are the results of simulations while the populations are single-shot pictures. **(Bottom)** Populations $\Pi_m(\hat{\mathbf{n}})$ along the direction $\hat{\mathbf{n}}$ in the xy plane used to compute the minimal and maximal variance for the squeezed state prepared at $\chi t = 0.21$. The solid (resp. dotted) red line corresponds to the average magnetization m_z (resp. variance).

Purity measurements

The purity of a spin state can be written as a function of its populations $\Pi_m(\hat{\mathbf{n}})$ [85] as

$$\mathrm{Tr}\left[\rho^2\right] = (2J+1)\sum_{m=-J}^{J}\int \frac{d\Omega}{4\pi}\,\Pi_m(\hat{\mathbf{n}})\Big[\Pi_m(\hat{\mathbf{n}}) - \Pi_{m+1}(\hat{\mathbf{n}})\Big] \tag{3.30}$$

where we define $\Pi_{J+1}(\hat{\mathbf{n}}) = 0$. The derivation of this equation is given in appendix B.

We evaluate the integral (3.30) from a discrete set of $\simeq 1000$ independent $\Pi_m(\hat{\mathbf{n}})$ measurements sampling the sphere. The quantity $p(\theta)$ is obtained after an integration over the azimuthal angle ϕ, i.e.

$$p(\theta) = (2J+1)\sum_{m=-J}^{J}\int_0^{2\pi}\frac{\mathrm{d}\phi}{2\pi}\,\Pi_m(\hat{\mathbf{n}})\left[\Pi_m(\hat{\mathbf{n}}) - \Pi_{m+1}(\hat{\mathbf{n}})\right], \tag{3.31}$$

such that

$$\mathrm{Tr}\left[\rho^2\right] = \frac{1}{2}\int_0^{\pi} p(\theta)\sin\theta\,\mathrm{d}\theta. \tag{3.32}$$

The quantity $p(\theta)$ is measured for coherent, squeezed and oversqueezed states and matches well the values expected from the one-axis twisting model as can be seen on figure 3.14. Integrating over the variable θ, we obtain purity values $\mathrm{Tr}[\rho^2] = 1.00(2)$, 1.00(3) and 1.01(4) respectively. Thanks to the symmetry $\Pi_m(\theta,\phi) = \Pi_{-m}(\pi-\theta,\phi+\pi)$, it is sufficient to compute $p(\theta)$ for $\theta < \pi/2$. The error bars are determined using a bootstrap sampling method.

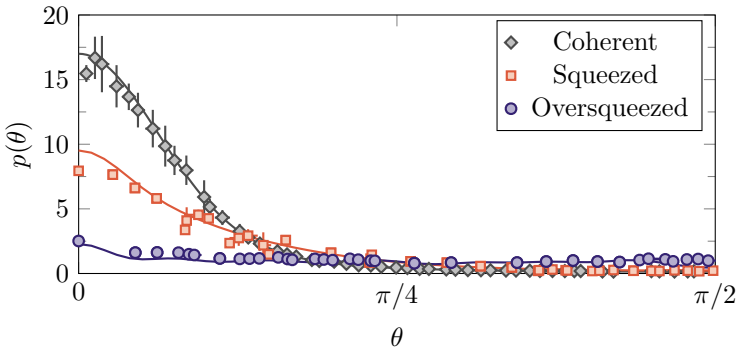

Figure 3.14 – Intermediate quantity $p(\theta)$ used to measure the purity. $p(\theta)$ is computed from $\Pi_m(\theta,\phi)$ for a coherent ($\chi t = 0$), squeezed ($\chi t = 0.12$) and oversqueezed ($\chi t = 0.55$) state. The solid lines correspond to the prediction of the one-axis twisting Hamiltonian. Intuitively $p(\theta)$ should be peaked more around $\theta = 0$ for the initial coherent state since it has population $\Pi_m(z)$ in $m = -8$ only. When the OAT evolves towards the squeezed and oversqueezed states, the populations spread among the m-states and the quantity $p(\theta)$ becomes more and more uniform.

Husimi functions

We can also experimentally reconstruct the Husimi function $Q(\theta, \phi) = Q(\hat{\mathbf{n}})$ of the prepared states. Using equation 3.13, Q can be related to the populations Π_m as

$$Q(\theta, \phi) = |\langle \theta, \phi | \psi \rangle|^2 = \left| \left(\hat{\mathcal{R}}(\theta, \phi) \, |m_J = +J\rangle \right)^\dagger |\psi\rangle \right|^2 \tag{3.33}$$

$$= \left| \langle m_J = +J | \, \hat{\mathcal{R}}(-\theta, \phi) \, |\psi\rangle \right|^2 = \Pi_{m=+J}(-\theta, \phi). \tag{3.34}$$

We plot on figure 3.15 the reconstructed Husimi function for the initial coherent state and for a squeezed state at $\chi t = 0.12$. Using again the symmetry $\Pi_m(\theta, \phi) = \Pi_{-m}(\pi - \theta, \phi + \pi)$, we only need to take data sampling half of the sphere. Two points of the Husimi function that are opposite on the sphere correspond to the same populations data.

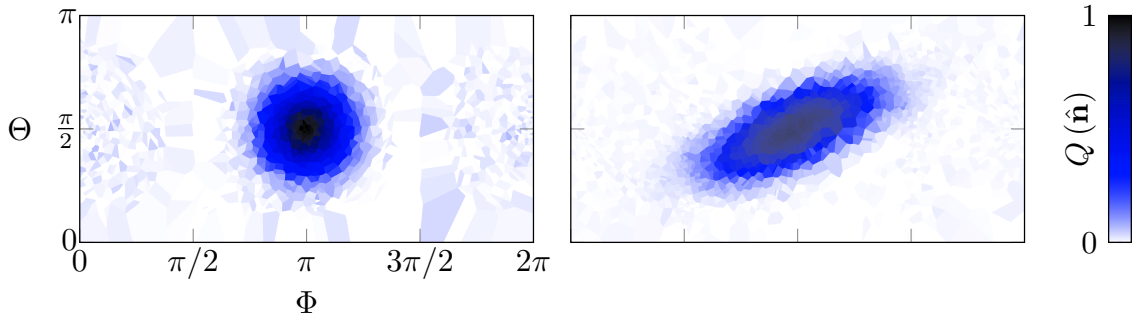

Figure 3.15 – Reconstructed Husimi function for a CSS and a squeezed state. We plot the Husimi function in a planar way for an easier visualization. The angles Θ and Φ correspond to a parametrization of the sphere in the (y, z, x) frame. This choice is made so that the distribution is centered on the graph and therefore remains minimally distorted, as the poles of the sphere are mapped onto lines on the graph. The data used here are the same as for the purity measurements.

These measurements confirm that the state preparation procedure is correct and that the corresponding states can be used for metrology. From the reduced variance observed in section 3.3.2, we expect enhanced magnetic field sensitivity, which remains to be explicitly shown from experimental Ramsey oscillations.

3.3.3 Ramsey oscillations for different states

The experimental sequence used to measure Ramsey oscillations is the following. The $\hat{J}_x^2$ coupling is applied for a duration t, after which we let the state precess on the north pole for a given time so that, once it is brought to the equator by a $\pi/2$ rotation, its direction of maximal variance is aligned on the z axis, and its minimal variance is aligned on the equator (except for the coherent state which is circular). We let the state precess on the equator during a waiting time τ before applying another $\pi/2$ rotation.

We represent on figure 3.16 the populations $\Pi_m(z)$ measured after the aforementioned sequence as a function of the azimuthal angle θ. The initial state of the Ramsey sequence obtained after the OAT preparation corresponds to $\theta = \pi$.

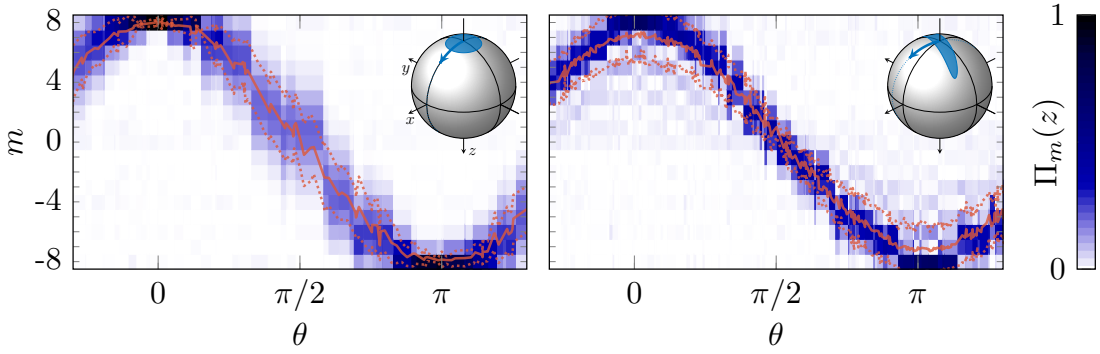

Figure 3.16 – Ramsey oscillations for a **(Left)** coherent state and **(Right)** squeezed state (corresponding to $\chi t = 0.15$). The solid red line corresponds to the average magnetization m_z and the red dotted lines correspond to $m_z \pm \Delta J_z$ computed from the populations $\Pi_m(z)$. The Bloch spheres show a semi-classical representation of the states and their trajectory during the Ramsey sequence.

We focus on the magnetization m_z and variance ΔJ_z^2 of these states as they are involved in the expression of the phase sensitivity according to equation 3.16. One can see that the slope $|dm_z/d\theta|$ is maximal at $\theta = \pi/2$ for both states. However while the variance is maximal at this point for the coherent state (expected value of 4, measured value of 4.3(1)), it is minimal for the squeezed state. Therefore when computing $\Delta\theta$ at position $\theta = \pi/2$ for both states, we find

$$\Delta\theta_{\text{coh}} = \frac{\sqrt{4.3(1)}}{8.01(4)} = 1.04(3)\,\Delta\theta_{\text{SQL}} \quad \text{and} \quad \Delta\theta_{\text{squeezed}} = 0.48(2)\,\Delta\theta_{\text{SQL}}$$

The sensitivity is indeed higher for the squeezed state. The oscillation contrast of m_z is smaller than 8 due to the fact that the states $m = -8$, $m = -6$ and $m = -4$ are populated, compared to the case of the coherent state. However the reduced variance greatly compensates this. The metrological gain G_R is deduced from the uncertainties $\Delta\theta$ and can be compared to the values of $1/\xi_R^2$ obtained from the minimal variance measurements of figure 3.12. As can be seen on figure 3.17, they coincide quite well.

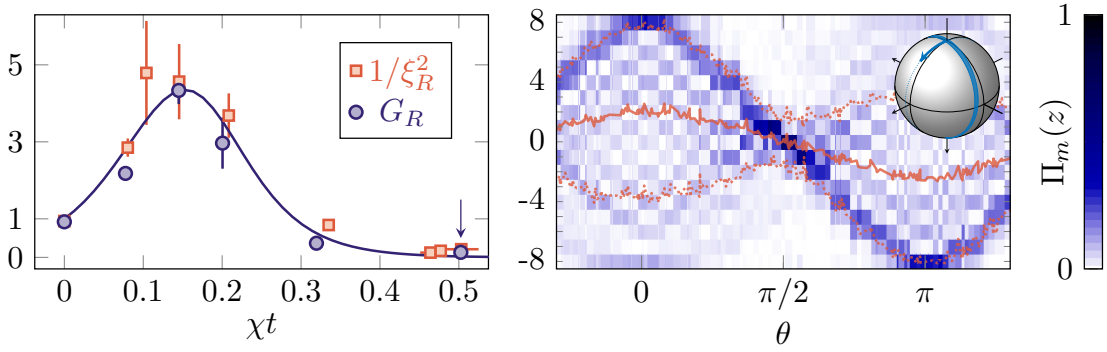

Figure 3.17 – Metrological gain and Ramsey oscillations for an oversqueezed state. **(Left)** Comparison between the metrological gain G_R directly computed from Ramsey oscillations and the $1/\xi_R^2$ value obtained from the minimal variance of the states. The arrow points at the oversqueezed state corresponding to the Ramsey oscillations. **(Right)** Details of the populations in the different m-states (along z) for the Ramsey oscillations of an oversqueezed state. The solid and dotted red lines correspond to the same quantities as for the previous Ramsey graphs.

We also plot on figure 3.17 the Ramsey oscillations obtained for an oversqueezed state. The fact that many m-states are populated induces a strong reduction of the contrast on the oscillations of m_z. Therefore the metrological gain computed from the method of moments is smaller than 1. However one can see how the populations of the single m-states vary quickly around $\theta = 0$. This means that even though the mean m_z is constant in the vicinity of $\theta = 0$, the state is changing rapidly. This is exactly what it means for a state to be sensitive : it changes 'a lot' under the effect of a magnetic field. This change is however not captured by the first and second moments of the population distribution. This suggests the use of another figure of merit that takes advantage of the variation at the single-m level. We present this figure of merit in the next chapter along with details of the oversqueezed states that are not captured by looking only at the mean and variance of Ramsey oscillations.

Chapter 4

Generalized metrological gain applied to non-gaussian spin states

Following the previous chapter, we first recall notions of *parameter estimation theory* which enable us to introduce a quantity called the *Fischer information* and the corresponding Cramér-Rao bound. This sets a theoretical limit on the metrological gain that we can obtain with a given state. We show an example of a well-chosen observable, the parity, that allows to reach this limit for the cat state.

We then introduce a statistical distance between distributions from which we can extract the metrological gain in a way that generalizes the definition given in equation 3.25 and works for all the states present in the OAT evolution [86]. In particular the metrological gain of an oversqueezed state computed in this new framework is better than that of a squeezed state. We show that this new definition of the metrological gain saturates the Cramér-Rao bound and is therefore optimal. It makes use of the full population distribution whereas the Ramsey sequence is intrinsically limited as it uses only the mean and variance of the population distribution. We provide a reconstruction of the Wigner function for an oversqueezed state, illustrating the metrological interest of these states.

We then describe how a state of a spin J can be seen as a symmetric state of $N = 2J$ fictitious spins 1/2. In particular a CSS corresponds to the absence of entanglement between them, while the cat state obtained at $\chi t = \pi/2$ is maximally entangled. The *Majorana stellar representation* is introduced and used to get a better understanding of the Husimi function of an oversqueezed state.

Finally this analogy is used to simulate a system of 16 indistinguishable interacting spins 1/2 corresponding to the Lipkin-Meshkov-Glick model.

4.1 Optimal sensitivity measurements

4.1.1 Parameter estimation theory and Cramér-Rao bound

In the context of spin states, measuring a magnetic field consists in measuring the angle ϕ corresponding to the effect of the Larmor rotation on a quantum state. The initial state $\hat{\rho}_0$ evolves according to the unitary evolution $\hat{\rho}_\phi = \hat{U}_\phi \, \hat{\rho}_0 \, \hat{U}_\phi^\dagger$ under the effect of the external magnetic field that we want to measure and/or controlled manipulations such as the $\pi/2$ rotations in a Ramsey sequence. While a full quantum

state tomography would be a way to deduce the value of ϕ (assuming we know the exact expression of $\hat{U}_\phi$), this is not feasible in most cases because of the size of the density matrix.

The phase ϕ can also be deduced from measurements on $\hat{\rho}_\phi$ whose outcome are used to infer the value of ϕ with minimum possible error. We assume that the measurements are described by an operator $\hat{A}$ with average outcome $\mu = \mathrm{Tr}[\hat{\rho}_\phi \hat{A}]$. We write $P(\mu|\phi)$ the probability to obtain a result μ given that the parameter has the value ϕ. By performing N such measurements independently, we obtain a set of results $\{\mu_1, ..., \mu_N\}$ from which we can define an *estimator* $\Phi(\mu)$ which associates a value of ϕ to the measured value of μ. It is a random variable with average value $\bar{\Phi} = \sum_{i=1}^{N} P(\mu_i|\phi)\Phi(\mu_i)$ and variance $\Delta\Phi^2 = \sum_{i=1}^{N} P(\mu_i|\phi)(\Phi(\mu_i) - \bar{\Phi})^2$. An estimator is said to be *locally unbiased* if it satisfies $\bar{\Phi} = \phi$ which means that the statistical average yields the parameter ϕ itself. In this context, the Cramér-Rao bound sets a limit to the minimum variance on the parameter ϕ that can be deduced from N independent measurements according to

$$\Delta\phi^{\,2} \geq \Delta\phi^{\,2}_{\mathrm{CR}} = \frac{1}{N\,F(\phi)} \tag{4.1}$$

where the $1/N$ factor corresponds to the usual reduction of variance with the number of measurements, and $F(\phi)$ is the Fischer information defined as

$$F(\phi) = \sum_{i=1}^{N} \frac{1}{P(\mu_i|\phi)} \left(\frac{\partial P(\mu_i|\phi)}{\partial \phi} \right)^2 . \tag{4.2}$$

$F(\phi)$ still depends on the choice of the operator $\hat{A}$ producing the measurements μ_i. The *quantum* Fischer information is defined as $F_Q(\phi) = \max_{\hat{A}}\ F(\phi)$ and the *quantum* Cramér-Rao bound now sets a limit on the minimal achievable variance irrespective of the chosen observable $\hat{A}$ as

$$\Delta\phi^{\,2}_{\mathrm{QCR}} = \frac{1}{N\,F_Q(\phi)} \tag{4.3}$$

In the case we are interested in here (pure spin states, unitary evolution), it can be shown that the quantum Fischer information simply is [87]

$$F_Q(\phi) = \max_{\hat{\mathbf{n}}}\ 4\,\Delta\hat{J}^2_{\hat{\mathbf{n}}} \tag{4.4}$$

where $\hat{\mathbf{n}}$ is a direction on the sphere. However this does *not* mean that it suffices to measure the mean magnetization in the direction $\hat{\mathbf{n}}$ to exhibit the maximum sensitivity. Saturating the quantum Cramér-Rao bound may require in practice complex measurements involving higher orders of the spin operators $\hat{J}^k_{\hat{\mathbf{n}}}$ [88] .

This yields for the maximum metrological gain $G_{\max}$ to be expected from a given state, knowing that $\Delta\phi_{\mathrm{SQL}} = 1/\sqrt{2J}$, the value

$$G_{\max} = \left(\frac{\Delta\phi_{\mathrm{SQL}}}{\Delta\phi_{\mathrm{QCR}}} \right)^2 = \frac{2}{J} \Delta\hat{J}^2_{\hat{\mathbf{n}}} \tag{4.5}$$

where the variance $\Delta\hat{J}^2_{\hat{\mathbf{n}}}$ is obtained from the averaging of several measurements on the considered state and therefore 'contains' the factor $1/N$.

The maximum variance $\Delta\hat{J}^2_{\hat{\mathbf{n}}}$ among all spin states is obtained for a coherent superposition of $|+J\rangle$ and $|-J\rangle$ with equal weights i.e. a cat state. It has a variance $\Delta\hat{J}^2_{\hat{\mathbf{n}}} = J^2$ and therefore the overall gain limit irrespective of the state is $G = 2J$. This global bound is called the *Heisenberg limit* [89].

4.1.2 Use of the parity operator to measure the sensitivity of a cat state

So far we have only considered the metrological gain G_R related to the contrast of Ramsey oscillations, which shows an increase of sensitivity at short times but decreases below one in the oversqueezed regime. However as suggested previously we should be able to obtain a better sensitivity by choosing another observable. An example of specific observable which saturates the Cramér-Rao bound is the parity operator $\hat{P}_x = (-1)^{J-\hat{J}_x}$ applied to the cat state [83]. The method of moments can be applied to this observable by computing its mean value and variance as

$$p_x = \langle\psi|\,\hat{P}_x\,|\psi\rangle = \sum_{m,m'} \alpha^*_{m'}\alpha_m \,\langle m'|_x\,(-1)^m\,\,|m\rangle_x = \sum_m (-1)^m\,\Pi_m(x) \tag{4.6}$$

$$\Delta P_x^2 = \langle\psi|\,\hat{P}_x^2\,|\psi\rangle - p_x^2 = 1 - p_x^2 \tag{4.7}$$

where we decomposed $|\psi\rangle$ in the x-basis as $|\psi\rangle = \sum_m \alpha_m\,|m\rangle_x$.

We plot computations of the metrological gain G_{par} inferred from the parity on figure 4.1, as well as the Cramér-Rao bound, for χt up to $\pi/2$. We can see that it indeed yields the maximum gain at $\chi t = \pi/2$ and reaches the Heisenberg limit.

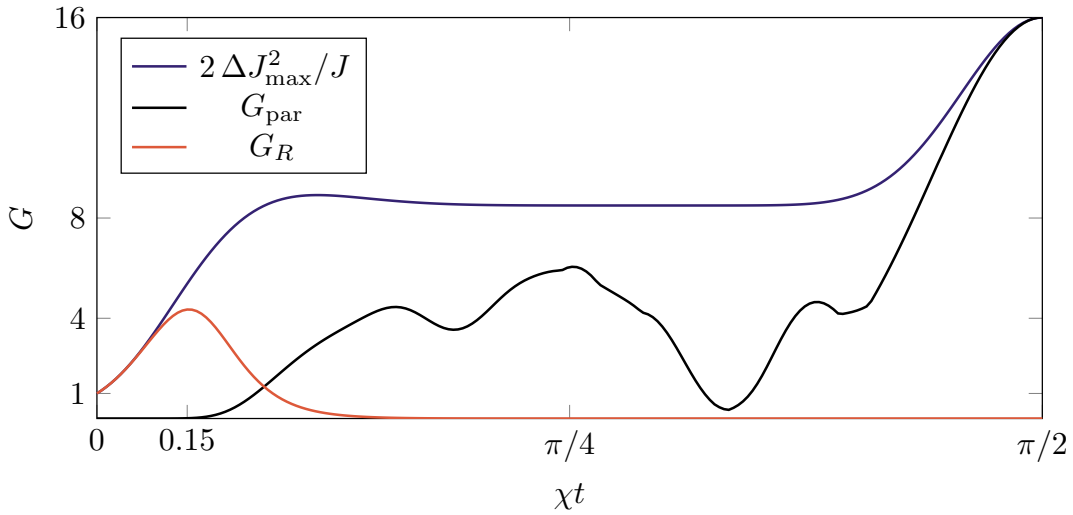

Figure 4.1 – Cramér-Rao bound and metrological gain expected from a parity measurement. The three curves are the result of simulations. While the standard Ramsey gain G_R (red) collapses when entering the oversqueezed regime, the gain G_{par} obtained from the parity (black) saturates the Cramér-Rao bound (blue) for the cat state at $\chi t = \pi/2$.

The experimental results presented in this section were published in [31]. We start by preparing a cat state with a light pulse of duration $\chi t = \pi/2$ as shown

on figure 4.2. The preparation is not perfect as the obtained state has a variance $\Delta\hat{J}_z^2 = 57.1(2)$ due to the presence of a non-zero quantization field along z (with a value of 18.5(3) mG) which perturbs the ideal OAT dynamics plotted on figure 3.6.

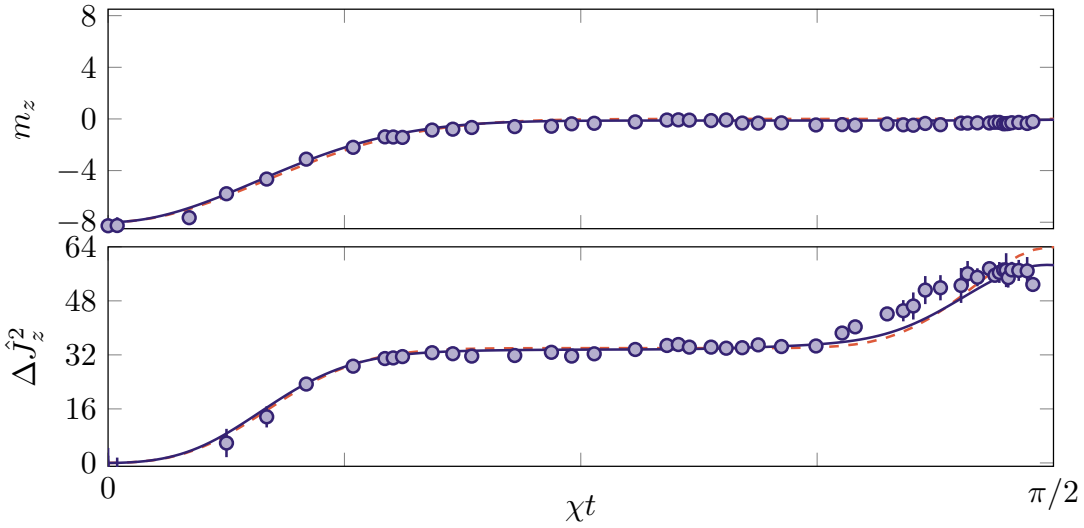

Figure 4.2 – Preparation of a cat state from the OAT Hamiltonian at $\chi t = \pi/2$. We plot both the magnetization and variance along z computed from the measured populations $\Pi_m(z)$. The red dashed lines correspond to the ideal OAT predictions while the solid blue lines are fitted taking into account imperfections such as non-zero magnetic field along z and inhomogeneous spin-coupling due to the spatial extension of the atomic cloud. The state identified as a 'cat' state corresponds to the variance maximum occurring a bit before $\chi t = \pi/2$.

We let the cat state acquire a phase ϕ under Larmor precession during a certain waiting time and explicitly write its evolution. We drop the global phase factor from equation 3.22 for simplicity. The acquired phase reads

$$|\psi(\phi)\rangle = \frac{1}{\sqrt{2}}(e^{iJ\phi}\,|-J\rangle_z + ie^{-iJ\phi}\,|+J\rangle_z) \tag{4.8}$$

which corresponds to a phase difference of $2J\phi$ between the two states. We can indeed see that the cat state is $2J$ times more sensitive to magnetic fields than a coherent state since it experiences a phase shift $2J$ times larger (in the same amount of time). However this phase shift cannot be measured from the populations along z, as these quantities remain invariant (eigenstates of $\hat{J}_z$).

We already saw in the previous chapter that it was beneficial to decompose the cat state in the x-basis. It allows to compute the parity easily as

$$|\psi(\phi)\rangle = \frac{1}{2^J}\sum_{m=-J}^{J}\sqrt{\binom{2J}{J-m}}\,i^m\frac{1}{\sqrt{2}}\left(e^{iJ\phi} + i(-1)^m e^{-iJ\phi}\right)|m\rangle_x \tag{4.9}$$

such that

$$\Pi_m(x) = \frac{1}{2^J}\binom{2J}{J-m}\Big(1 + (-1)^m\sin(2J\phi)\Big) \tag{4.10}$$

and finally

$$p_x = \sum_{m=-J}^{J} (-1)^m \, \Pi_m(x) = \sin(2J\phi) \tag{4.11}$$

which indeed corresponds to an oscillation period $2\pi/(2J)$.

The parity along x is experimentally accessible by performing a rotation mapping the z-axis onto x (i.e. a $\pi/2$ rotation along y). We plot on figure 4.3 the populations along x and the deduced average parity (according to equation 4.6) as a function of ϕ.

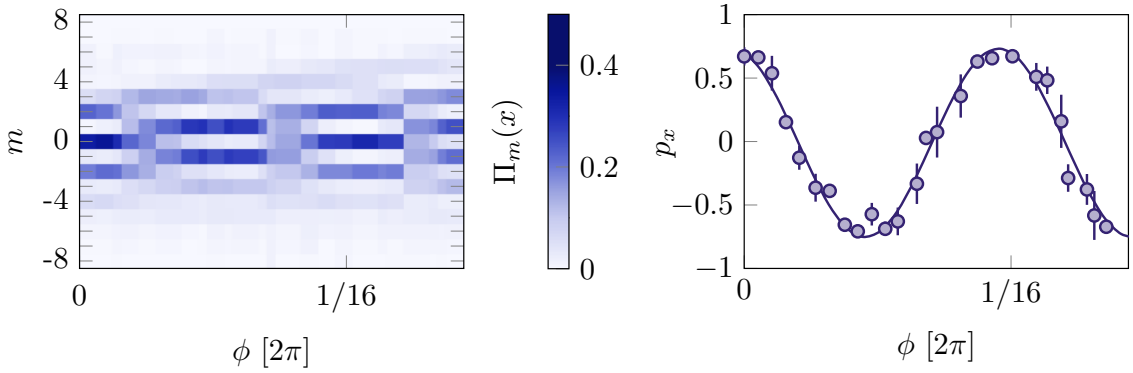

Figure 4.3 – Measured parity oscillations as a function of the Larmor phase ϕ. (Left) Populations in each m-state along x plotted as a color scale. Only even-m states are populated at $\phi = 0$, while only odd-m states at $\phi = 2\pi/32$ (half period). The period is 16 times smaller than the Larmor period measured for a standard Ramsey sequence with a CSS. **(Right)** Parity computed from the corresponding populations. The solid line corresponds to a fit of the data points. While it should in principle have a contrast of one (equation 4.11), experimental imperfections in the measurement of the populations lead to a reduced contrast $C = 0.74(2)$.

While the metrological gain computed from the method of moments applied to the oscillations of p_x is supposed to saturate the Cramér-Rao bound and reach $G = 16$, we do not obtain this value experimentally. Even though the factor $2J$ in the oscillation frequency is observed, taking into account the reduced contrast C, the experimental value of the metrological gain is computed as $G = 2JC^2 = 8.8(4)$ which is quite far from the Cramér-Rao bound for this state $2\Delta\hat{J}_z^2/J = 14.3(1)$. This can be understood from the fact that the experimental computation of the parity is very sensitive to detection imperfections. Populations are spread between many m-states and small population imbalances between even and odd m build up when computing $\sum_m (-1)^m \, \Pi_m$.

4.1.3 Metrological gain based on the Hellinger distance

The extraction of a metrological gain from a Ramsey sequence, presented in details in chapter 3, is optimal only for gaussian states, and the parity operator is an example of specific observable which is supposed to be optimal for the cat state. Yet in practice we are not able to recover the expected maximal sensitivity. These two types of measurements both rely on the method of moments, i.e. the mean and variance of operators, in the first case a spin operator $\hat{J}_{\hat{\boldsymbol{u}}}$, in the second case the parity operator $\hat{P}$.

However we have access to the single-m populations, i.e. all the information encoded in a given state, not just the first and second moments of the distribution Π_m. The idea that we can make use of all the populations separately was already hinted at in figure 3.17, which is a plot of Ramsey oscillations for an oversqueezed state. We introduce the notion of statistical distance [90] and in particular the (squared) Hellinger distance between two distributions $\Pi_m(\theta,\phi)$ and $\Pi_m(\theta',\phi)$ as

$$d_H^2(\theta,\theta') = \frac{1}{2}\sum_m \left[\sqrt{\Pi_m(\theta,\phi)} - \sqrt{\Pi_m(\theta',\phi)}\right]^2 . \tag{4.12}$$

This quantity accounts for changes in population for every m-state in a way that the method of moments cannot. It allows to generalize the notion of metrological gain according to [91]

$$G(\theta) = \frac{2}{J}\left.\frac{\partial^2 d_H^2(\theta,\theta+\alpha)}{\partial\alpha^2}\right|_{\alpha=0} \tag{4.13}$$

i.e. the sensitivity is related to the rate of change of d_H^2 when performing an infinitesimal rotation of angle α. We expect $G(\theta)$ to be maximum around $\theta = 0$ according to [86]. Note that this new definition of the metrological gain coincides with G_R (related to the contrast of Ramsey oscillations) for gaussian states, i.e. coherent and squeezed states.

The Hellinger distance was already used as an experimental tool to characterize the sensitivity of non-gaussian spin states of an ensemble of $N = 380 \pm 15$ atoms in the group of M. Oberthaler [82]. The intrinsic difference with our work is the fact that in their case the OAT is engineered through atomic interactions. Cat states remain out of reach for such systems despite a very good experimental precision, since the decoherence scaling is exponentially unfavorable as mentioned already. In our case, the metrological gain of the cat state is measured from the Hellinger distance curvature at a value $G = 13.9(11)$, quite close to the corresponding Cramér-Rao bound $G_{\max} = 14.3(1)$. This technique based on the Hellinger distance can be applied to the entire range of oversqueezed states, provided that all measurement directions are accessible. For oversqueezed states there is no 'lucky' observable like the parity for the cat state, and they require a complex combination of spin operators of order 5 [88]. In addition this operator choice depends on the specific preparation time χt and therefore cannot be easily used in a systematic way.

Experimental procedure

We describe the experimental procedure to extract the value of the metrological gain from a state prepared at $\chi t = 0.21(3)$. We first plot on figure 4.4 the populations

when performing small-θ rotations for two different values of ϕ to understand the role of ϕ on the metrological gain computed from the Hellinger distance. We see in (a) that only the even states are initially populated and we observe no change as a function of θ. On the other hand in (b) the odd states get populated as θ increases, which results in a large change of $d_H^2(0,\theta)$.

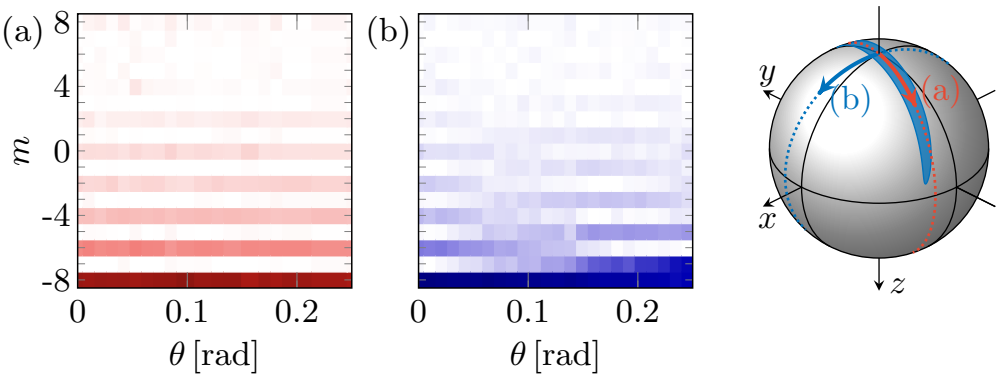

Figure 4.4 – Variation of the populations Π_m for small rotations θ in two directions. After preparing a squeezed state (so that we can define the directions of minimum and maximum variance), we measure its populations along z after performing small-θ rotations with ϕ chosen in the direction of minimum (a) and maximum (b) variance as illustrated on the sphere on the right.

The metrological gain G is deduced from the curvature of the Hellinger distance as plotted on figure 4.5.

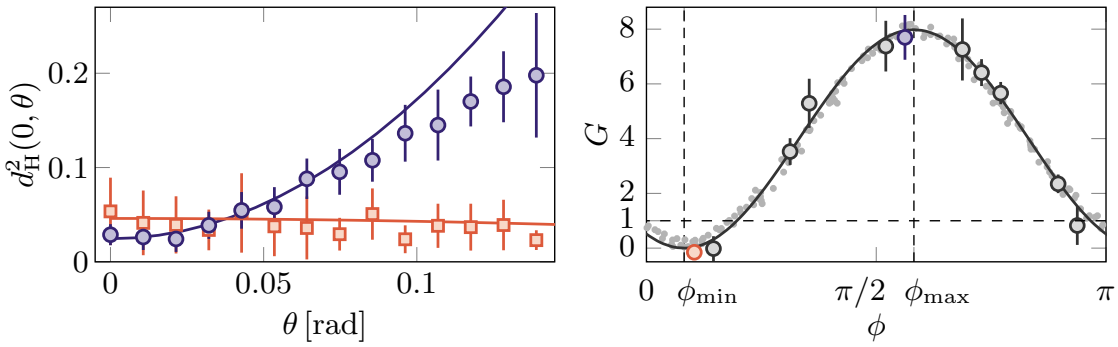

Figure 4.5 – Curvature of the Hellinger distance resulting in different values of G. (Left) Hellinger distance around $\theta = 0$ for the two angles $\phi_{\min}$ (red) and $\phi_{\max}$ (blue) corresponding to the directions plotted on figure 4.4. Solid lines are quadratic fits performed at small-θ (more details are given below). **(Right)** Value of the metrological gain G deduced from the curvature of the Hellinger distance. The red and blue dots are the extremal points corresponding to $\phi_{\min}$ and $\phi_{\max}$. The black solid line is a sine fit of the data and grey dots correspond to the Cramér-Rao bound.

It is not obvious how to fit the curvature of $d_H^2(0,\theta)$ in the vicinity of $\theta = 0$. The procedure used here is to measure first $d_H^2(\theta,\theta')$ as shown on figure 4.6 and perform a fit with the ansatz

$$d_H^2(\theta,\theta') = \sum_{0\leq p+q\leq n} a_{p,q}(\theta-\theta')^{2p}(\theta+\theta')^{2q} \tag{4.14}$$

which is a polynomial of order n in the two variables $(\theta-\theta')^2$ and $(\theta+\theta')^2$. This a way to separate the $(\theta-\theta')^2$ terms that we are interested in from the $(\theta+\theta')^2$ terms which come from experimental imperfections or appear only far from the origin $\theta = \theta' = 0$. Equation 4.13 then simply yields $G = 4a_{1,0}/J$. Different values of n were considered, with an optimal result for $n = 2$. Indeed $n = 1$ does not allow for the presence of quartic terms and the fit of the harmonic part picks up higher order contributions. For $n \geq 3$, the error bars (obtained from a bootstrap method) become increasingly large which suggests that the number of fitted parameters becomes too large and the fit is therefore not constrained enough. The fact that the value of G obtained for $n = 2$ remains consistent with the Cramér-Rao bound also validates the analysis. The data plotted on the left panel of figure 4.5 is a line-cut of $d_H^2(\theta,\theta')$ for $\theta' = 0$.

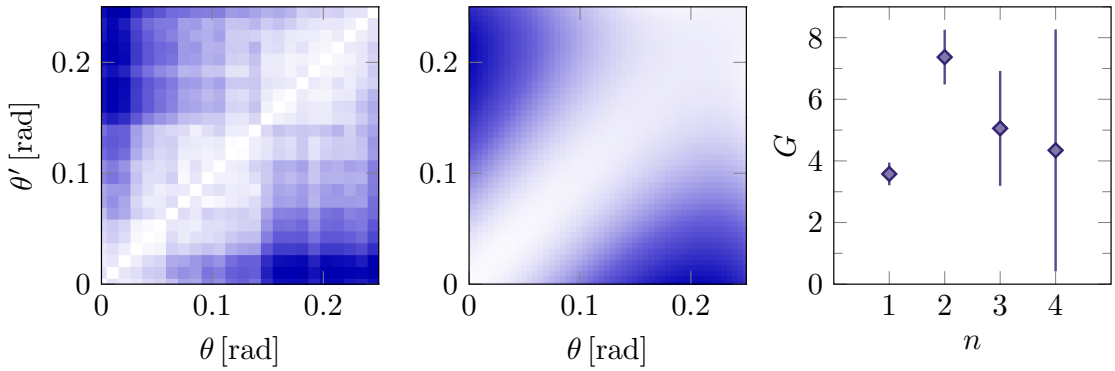

Figure 4.6 – Extracting the value of G from the Hellinger distance. **(Left)** Hellinger distance $d_H^2(\theta,\theta')$ plotted as a color scale. **(Center)** Fitted polynomial of degree $n = 2$. **(Right)** Different values of G obtained for different values of n.

For each interaction time χt, the Hellinger distance $d_H^2(\theta,\theta')$ is measured for different values of ϕ according to the previous method. The value of $\phi_{\max}$ depends on the orientation of the prepared state since the directions of minimum and maximum variance rotate as the state gets squeezed [37]. By maximizing the measured value of G over the angle ϕ as shown on the right panel of figure 4.5, we can extract the overall maximum of G for a given state. We plot the result on figure 4.7 as well as the values of G_R corresponding to the 'old' definition with a Ramsey sequence. We see that we saturate the Cramér-Rao bound meaning that the Hellinger distance is an optimal figure of merit for the class of states corresponding to the OAT [86]. The reason why it works so well is that we have access to the single-m populations, which is a key feature of our system and does not have a simple equivalent in systems of N interacting qubits. Therefore one cannot necessarily expect to saturate the Cramér-Rao bound in other situations.

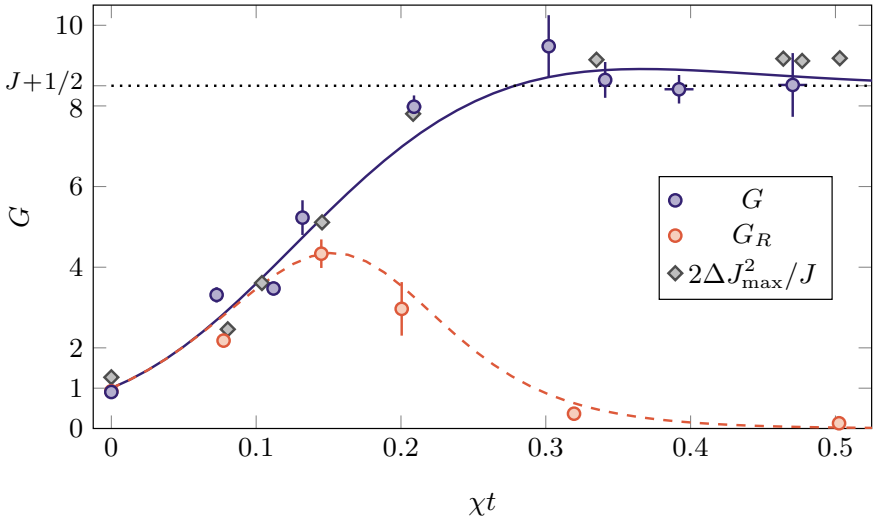

Figure 4.7 – Metrological gain for the different prepared states. Blue circles are the values obtained from the Hellinger distance curvature while red circles are the values from figure 3.17, corresponding to Ramsey oscillations. Grey squares correspond to the Cramér-Rao bound. The solid blue and dashed red lines are theoretical predictions of the OAT with the only fitted parameter being the scaling of the x-axis i.e. the value of χ.

4.1.4 The Wigner function

A feature of oversqueezed states is that their Wigner function exhibits negative parts, which is a sign of non-classicality [92]. The Wigner function is similar to the Husimi function in the sense that it is a function of the variables θ and ϕ used to represent spin states on the sphere. So far we used only the Husimi function to represent coherent and squeezed states as it intuitively represents the probability $P(\theta,\phi) = |\langle\psi|\theta,\phi\rangle|^2$ to measure a spin state $|\psi\rangle$ entirely polarized in the direction (θ,ϕ). However for oversqueezed states and for the cat state the Wigner function exhibits characteristic oscillatory features that are not captured by the Husimi function.

The Wigner function $W_{\hat{A}}(\theta,\phi)$ of an operator $\hat{A}$ is defined as [75]

$$W_{\hat{A}}(\theta,\phi) = \sum_{k=0}^{2J}\sum_{q=-k}^{k} A_{kq} Y_k^q(\theta,\phi) \tag{4.15}$$

which corresponds to an expansion on the basis of multipole operators $\hat{T}_{k,q}$ with

$$A_{kq} = \mathrm{Tr}[\hat{A}\,\hat{T}_{kq}^{\dagger}] \tag{4.16}$$

$$\hat{T}_{kq} = \sum_{m,m'=-J}^{J} (-1)^{J-m}\sqrt{2k+1}\begin{pmatrix} J & k & J \\ -m & q & m' \end{pmatrix} |J,m\rangle\langle J,m'| \tag{4.17}$$

where the bracket term is a Wigner-3j coefficient.

The formalism of the Wigner function yields a convenient way to compute traces as [93]

$$\mathrm{Tr}[\hat{A}\hat{B}] = \int W_{\hat{A}}(\theta,\phi)\, W_{\hat{B}}(\theta,\phi)\, d\Omega \tag{4.18}$$

for any operators $\hat{A}$ and $\hat{B}$. In the case where the operator $\hat{A}$ is the density matrix ρ of a given state, we can define the Wigner function of this state as $W(\theta,\phi) = W_\rho(\theta,\phi)$. In the same way that we were able to express the Husimi function and the purity in terms of the populations $\Pi_m(\hat{\mathbf{n}})$ in the direction $\hat{\mathbf{n}}$, the Wigner function can be decomposed as

$$W(\hat{\mathbf{n}}) = \sum_{m=-J}^{J} (-1)^{J-m} a_m \Pi_m(\hat{\mathbf{n}}) \tag{4.19}$$

where

$$a_m = \frac{2k+1}{\sqrt{4\pi}} \sum_{k=0}^{2J} \begin{pmatrix} J & J & k \\ m & -m & 0 \end{pmatrix} \tag{4.20}$$

as shown in appendix C. The Wigner function, reconstructed from $\Pi_m(\hat{\mathbf{n}})$ measurements similarly to the Husimi functions of figure 3.15, is plotted on figure 4.8.

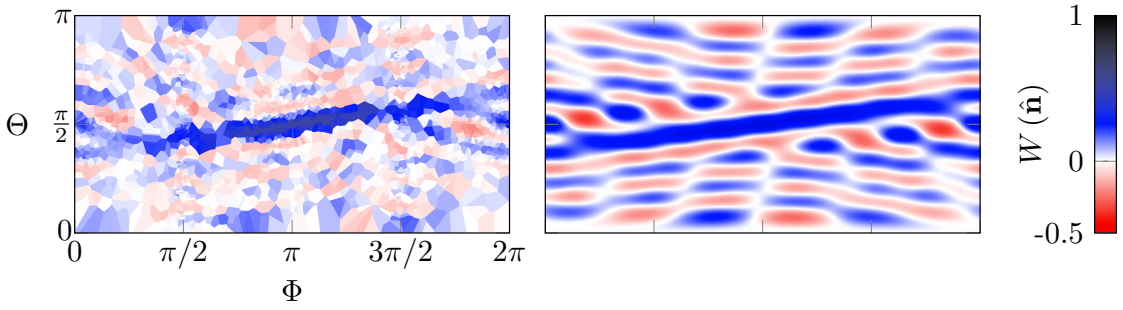

Figure 4.8 – Wigner function of an oversqueezed state. The state corresponds to $\chi t = 0.55$. **(Left)** Wigner function experimentally reconstructed from measurements of the populations in different directions $\Pi_m(\hat{\mathbf{n}})$. **(Right)** Expected Wigner function. Red regions correspond to the negative parts of the Wigner function which is an indicator of non classicality.

The fringes of the Wigner function are a way to intuitively understand the magnetic field sensitivity of oversqueezed states. Indeed the sensitivity is equivalent to the amount of change that a state undergoes under an infinitesimal rotation, which is why the Hellinger distance proved to be a successful tool. The Wigner function of a state undergoing an infinitesimal rotation of angle $\delta\theta$ has the shame shape has the initial Wigner function, with a small global shift $\delta\theta$. Therefore the overlap $O_{\delta\theta}$ between the initial state $|\psi\rangle$ and the slightly rotated state $|\psi_{\delta\theta}\rangle$, which is equal to

$$O_{\delta\theta} = \left|\, \langle\psi|\psi_{\delta\theta}\rangle \,\right|^2 = \mathrm{Tr}[\rho\, \rho_{\delta\theta}] \tag{4.21}$$

can be written in terms of Wigner functions thanks to equation 4.18 as

$$O_{\delta\theta} = \int W(\theta,\phi)\, W_{\delta\theta}(\theta,\phi)\, d\Omega \tag{4.22}$$

$$= \int W(\theta,\phi)\, W(\theta-\delta\theta,\phi)\, d\Omega. \tag{4.23}$$

The overlap varies a lot even with small values of $\delta\theta$ due to the presence of small-scale oscillations between positive and negative values in the Wigner function of an oversqueezed state, resulting in a large sensitivity.

The Wigner function of the cat state, plotted on figure 4.9 with the so-called Mollweide (or elliptical) projection, is even more striking as it also shows that this state is much more sensitive to rotations around z than other directions. The explicit effect of such a rotation has already been mentioned in equation 4.8. The interference pattern on the equator shows how a rotation of angle $\delta\phi$ along z is going to induce a large change when computing $\int W(\theta,\phi)\, W(\theta,\phi+\delta\phi)\, d\Omega$. Note that the fringes consist in 16 oscillations on the equator of the Bloch sphere corresponding to the value $G = 16$ mentioned earlier.

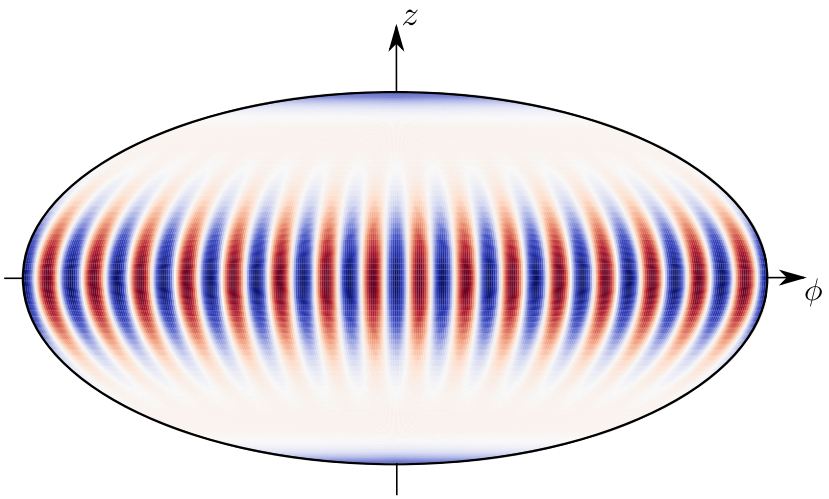

Figure 4.9 – Wigner function for the cat state with an elliptical projection of the sphere computed numerically from equation 4.19.

4.2 Investigating the link to symmetric states of 2J entangled qubits

4.2.1 Husimi function of an oversqueezed state

As we just described, the Wigner function can be perceived as a more powerful representation than the Husimi function. However the Husimi function of the oversqueezed state is still worth taking a closer look at. We plot on figure 4.10 the reconstructed Husimi function for an oversqueezed state at $\chi t = 0.55$, from the same data used to reconstruct the Wigner function, along with the exact shape expected from calculations. As the elliptical shape of the squeezed state gets more stretched,

it wraps around the sphere and starts overlapping with itself. The wrapping is visible on the edges of the planar plot, which has periodic boundary conditions in Φ. This shows the intrinsic difference between squeezed states of the electromagnetic field in representation $\hat{x}, \hat{p}$ and spin squeezed states. The topology of the sphere leads to a saturation of the squeezing 'efficiency' [69] while on a plane there is no intrinsic limit to how much a squeezed state can stretch. This 'self-overlap' occurs together with the apparition of 'holes' in the distribution $Q(\hat{\mathbf{n}})$.

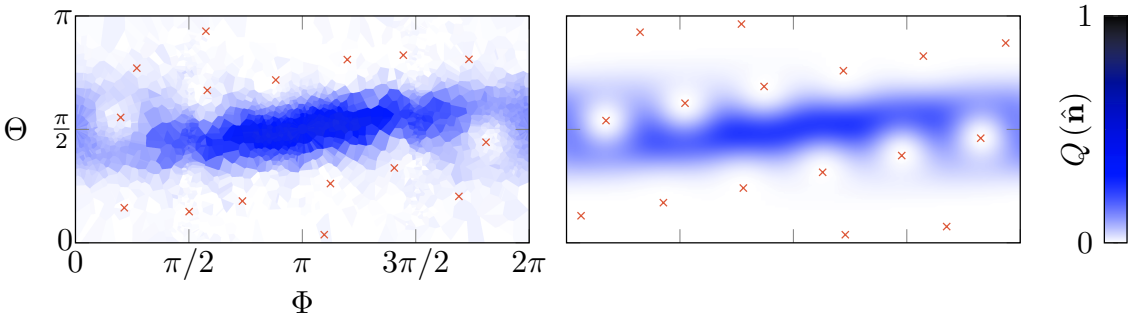

Figure 4.10 – Husimi function of an oversqueezed state. The state corresponds to $\chi t = 0.55$. **(Left)** Experimentally reconstructed Husimi function. **(Right)** Expected Husimi function. The key feature is the apparition of 'holes' in the distribution, interpreted as the directions opposites to that of the unit spins 1/2 constituting the spin J, and represented as red crosses.

If we consider a spin J as an assembly of $2J$ spins 1/2, the OAT Hamiltonian appears as a way to induce correlations between these spins, resulting in non-isotropic variance, i.e. squeezing. A coherent spin state $|\theta, \phi\rangle$ corresponds to all the unit spins pointing in the direction (θ, ϕ). The Dicke state $|m\rangle_z$ corresponds to $J + m$ spins 1/2 pointing up and $J - m$ pointing down.

We define the $\hat{\boldsymbol{u}}_i$ as the orientations (in the sense of equation 3.1) of the $2J$ spins 1/2, allowing to write the Husimi function as

$$Q(\hat{\mathbf{n}}) \propto \prod_{i=1}^{2J} |\langle \hat{\boldsymbol{u}}_i | \hat{\mathbf{n}} \rangle|^2 \tag{4.24}$$

where $|\hat{\mathbf{n}}\rangle$ corresponds to the state of a qubit pointing in direction $\hat{\mathbf{n}}$. Note that if $\hat{\boldsymbol{n}}$ is defined by the angles (θ, ϕ) and $\hat{\boldsymbol{u}}_i$ by (θ_i, ϕ_i), we have

$$|\langle \hat{\boldsymbol{u}}_i | \hat{\mathbf{n}} \rangle|^2 = 1 + \hat{\boldsymbol{u}}_i \cdot \hat{\mathbf{n}} = 1 + \cos(\theta - \theta_i) - \sin\theta \sin\theta_i \big[1 - \cos(\phi - \phi_i)\big] \tag{4.25}$$

such that if all the $\hat{\boldsymbol{u}}_i$ coincide in the direction (θ_0, ϕ_0), we recover the expression of the Husimi function for a coherent state given in equation 3.9.

The Majorana stellar representation is a way to define the state of a spin J uniquely by the position of $2J$ points on the Bloch sphere. $Q(\hat{\mathbf{n}})$ has $2J$ zeroes corresponding to the directions opposite to the Majorana 'stars' $\hat{\mathbf{n}} = -\hat{\boldsymbol{u}}_i$, some of them being visible as they sit close to regions where the Husimi function is localized,

causing the presence of 'holes'. Red marks on the experimental data of figure 4.10 stand for the positions of the zeroes fitted according to equation 4.24.

These zeroes are entirely defined, for a state written as $|\psi\rangle = \sum_m c_m |m\rangle_z$, as the $2J$ roots of the polynomial (of degree $2J$)

$$P(z) = \sum_{m=-J}^{J} (-1)^{J-m} \sqrt{\binom{2J}{J-m}}\, c_m\, z^{J+m} \tag{4.26}$$

where z is a complex number [94]. The position of the zeroes on the sphere in terms of the angles (θ, ϕ) is deduced from the stereographic projection of the complex plane on the sphere by writing z in terms of modulus and argument as

$$z = \tan(\theta/2)\, e^{i\phi}. \tag{4.27}$$

Red marks on the expected Husimi function of figure 4.10 are deduced from equation 4.26, given the coefficients c_m of the oversqueezed state prepared at $\chi t = 0.55$.

Construction of the Dicke basis

The equivalence between a system of $N = 2J$ spins 1/2 and a large spin J is only valid for symmetric states, i.e. invariant under exchange of any two spins 1/2. Indeed in the picture of $2J$ fictitious spins 1/2 adding up to form a spin J, we cannot label the spins and specify which one would be up or down.

The dimension of the Hilbert space for a general system made of N spins 1/2 is 2^N, however in the case of symmetric states the only relevant quantity is the number of spins pointing up or down. The basis of symmetric states is thus constituted of the $N+1$ states

$$\begin{cases} |\downarrow\downarrow ... \downarrow\rangle \\ \Big(|\uparrow\downarrow ... \downarrow\rangle + |\downarrow\uparrow ... \downarrow\rangle + ... + |\downarrow\downarrow ... \uparrow\rangle \Big) / \sqrt{N} \\ : \\ \sum\limits_{\binom{N}{k} \text{ terms}} |k\times\uparrow, N-k\times\downarrow\rangle \Big/ \sqrt{\binom{N}{k}} \\ : \\ |\uparrow\uparrow ... \uparrow\rangle \end{cases}$$

which correspond to the $2J+1$ states of the Dicke basis $\{|J,m\rangle\,,\ m = -J, ..., J\}$ for $N = 2J$. This is equivalent to saying that we have taken into account the indistinguishability of the spins 1/2 by symmetrizing the basis states of the full Hilbert space.

4.2.2 Decoherence of a cat state

The cat state obtained from OAT at $\chi t = \pi/2$ corresponds in this context to the superposition of the states $|\downarrow\downarrow ... \downarrow\rangle$ and $|\uparrow\uparrow ... \uparrow\rangle$. However it lives in the $2J+1$ - dimensional subspace of symmetric states, not in the full 2^{2J}- dimensional Hilbert

space of $2J$ spins 1/2. The number of decoherence channels is reduced and we expect the dephasing of the cat state to occur $2J = 16$ times faster than for a coherent state, to be compared for example with a N^2 scaling of the decoherence observed for $N = 14$ qubits in [95]. Measurements of decoherence for a coherent state, based on the reduction of the contrast C of Ramsey oscillations over time, are plotted on figure 4.11, along with the decoherence of a cat state. The latter is characterized by a reduction of the reconstructed density matrix correlation term $|\rho_{-J,J}|$. While the $1/e$ decay time for the coherent state is measured at $\tau_0 = 740 \pm 80\,\mu$s and taken as reference, the $1/e$ decay for the cat state is $\tau = 58 \pm 4\,\mu$s. In the end we obtain $\tau_0/\tau = 13(2)$ from these measurements, showing that the increase in metrological gain comes together with an intrinsic fragility to decoherence. In this case it can be considered as 'classical' decoherence in the sense that it is directly proportional to the sensitivity. It is equivalent to saying that the cat state is 16 times more sensitive to magnetic field noise than a coherent state, and therefore decoheres 16 times faster.

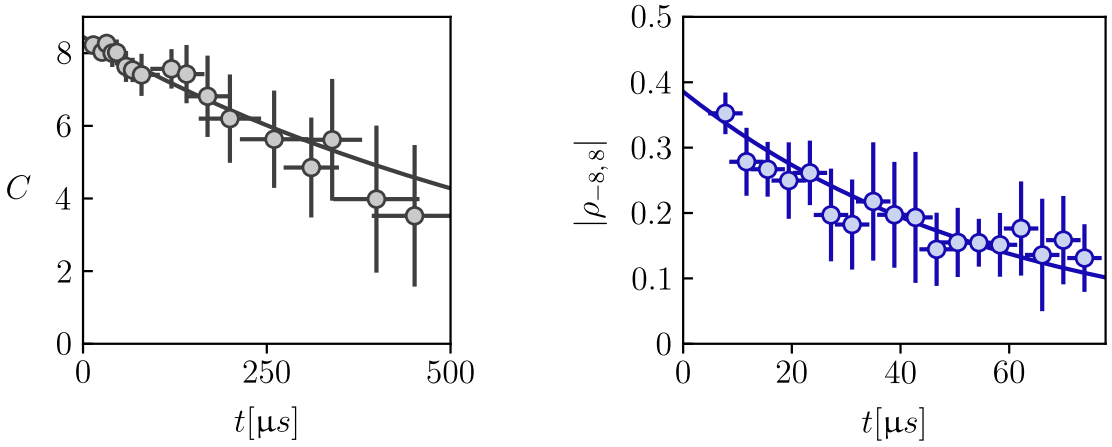

Figure 4.11 – Decoherence for a coherent state and a cat state. **(Left)** The measured contrast of Ramsey oscillations decays from its initial value of 8 because of magnetic field fluctuations. **(Right)** The off-diagonal term of the density matrix $|\rho_{-8,8}|$ corresponding to the coherence of the cat state decays much faster. Solid lines correspond to exponential decay fits.

The fundamental difference with the 'real' entanglement of N qubits can be illustrated by considering the loss of one atom. In our case it does not change the state of the entire system since the entanglement is not induced by atom-atom interactions bur rather 'contained' within each of the atoms with large spin J. This is to be opposed with the entanglement of a NOON state $\big(|N,0\rangle + |0,N\rangle\big)/\sqrt{2}$, whose coherence is destroyed by the loss of only one atom.

This is what justifies the interest of oversqueezed states, with a plateau of metrological gain $G = J + \frac{1}{2}$. However the method we use to extract the metrological gain (with the Hellinger distance) relies on the fact that we are able to measure single-m populations. This cannot necessarily be transferred to other systems, in particular to the case of a large spin formed by N qubits. It could nevertheless be

applied to the case of ultracold molecules which constitute a natural extension of our large-spin atom study [73]. Oversqueezed states are obtained for interaction times $\chi t \sim 1/\sqrt{2J}$, short for relatively large J compared to $\chi t = \pi/2$ for the cat state. This is of particular interest in situations where there are fluctuations of the coupling strength χ. In such cases, the preparation of the cat state would be strongly altered whereas states prepared at short times are more reliable.

4.2.3 Analogy with a system of 16 interacting spins 1/2

Ground state preparation

Based on the equivalence between the electronic spin $J = 8$ of dysprosium (in the ground state) and symmetric (upon exchange) states of $N = 2J = 16$ spins 1/2 described previously, we simulate a system of 16 interacting spins 1/2. The results presented in this section were published with further details in [96].

The Lipkin-Meshkov-Glick model (LMGm) describes indistinguishable quantum spins with infinite range Ising interactions in a transverse field. The corresponding Hamiltonian reads

$$\hat{H} = -\frac{\hbar\lambda}{4(N-1)} \sum_{i \neq j} \sigma_x^{(i)} \sigma_x^{(j)} + \frac{\hbar\omega_z}{2} \sum_i \sigma_z^{(i)} \tag{4.28}$$

where $\sigma_{x,z}^{(i)}$ are the Pauli matrices applied to the spin i. The interaction strength $\lambda > 0$ corresponds to spin-spin interactions, ω_z is the Zeeman energy associated with the transverse magnetic field and the factor $1/(N-1)$ ensures the extensivity of the energy in the large N limit. From the expression of equation 4.28 it is clear that the Hamiltonian is invariant under spin-exchange, as the interactions are all-to-all and of infinite range (there cannot be a notion of position in this system as the spins are indistinguishable).

We introduce the collective spin operators $\hat{J}_{x,z} = \frac{1}{2}\sum_i \sigma_{x,z}^{(i)}$ from which we get

$$\hat{H} = -\frac{\hbar\lambda}{N-1}\left(\hat{J}_x^2 - \frac{N}{4}\right) + \hbar\omega_z \hat{J}_z. \tag{4.29}$$

We can neglect the constant term in $\hat{H}$ to obtain

$$\hat{H} = -\frac{\hbar\lambda}{2J-1}\hat{J}_x^2 + \hbar\omega_z \hat{J}_z \tag{4.30}$$

which has the same $\hat{J}_x^2$ and $\hat{J}_z$ terms as the experimental implementation of the OAT in presence of a quantization field along z given in equation 3.27. The difference is that now the goal is to prepare the ground-state of the Hamiltonian, whereas for the OAT the goal was to induce coherent dynamics in the $\{|J, m\rangle, m = -J, ..., J\}$ Zeeman manifold. Instead of a light pulse, here the laser power is adiabatically ramped up, in approximately 100 µs. The other experimental aspects are identical to the ones used for the study of spin squeezing and metrological gain that we already presented.

Quantum phase transition

The LMGm exhibits a phase transition at $\lambda/\omega_z = 1$, which we can study properly with well-chosen values of the experimental parameters. The value of the magnetic field is $B_z = 114(1)$ mG, leading to $\omega_z = 2\pi \times 198(2)$ kHz, the available laser power being large enough to reach values around $\lambda/\omega_z = 4$, with typical ramp speed $\dot{\lambda} \simeq 0.015\,\omega_z^2$. In the absence of light ($\lambda = 0$), the ground state is $|-J\rangle_z$ due to the $\hat{J}_z$ term of the Hamiltonian. In the limit $\lambda/\omega_z \gg 1$, the $-\hat{J}_x^2$ term is dominant and the ground state is a superposition of $|-J\rangle_x$ and $|+J\rangle_x$, where the x subscript corresponds to the decomposition of a state in the x-basis.

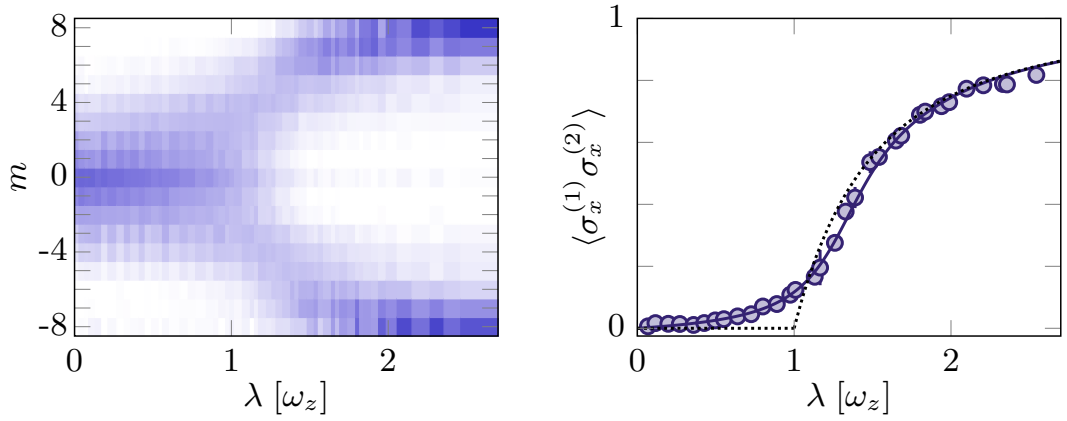

Figure 4.12 – Populations along x showing the crossover between paramagnetic and ferromagnetic phases. **(Left)** Measured populations along x. These are single-shot measurements, showing the relatively low experimental noise. **(Right)** Spin correlator along x deduced from the variance of the populations. The blue line corresponds to the prediction of the LMGm while the black dotted line corresponds to a classical mean-field model exhibiting the usual discontinuity of the derivative at the transition point $\lambda = 1$.

We plot on figure 4.12 the measured populations along x as a function of λ. We observe at $\lambda = 0$ populations centered on $m = 0$ consistent with the decomposition of $|-J\rangle_z$ in the x-basis given in equation 3.19. In the ferromagnetic phase for large $\lambda/\omega_z \gtrsim 2$, the population distribution shows two peaks close to the $|-J\rangle_x$ and $|+J\rangle_x$ states. The correlator $\langle\sigma_{1x}\sigma_{2x}\rangle$ characterizing the relative alignment between spins along x is deduced from the variance of the populations. Indeed we have [97]

$$N + N(N-1)\langle\sigma_{\hat{\mathbf{n}}}^{(1)}\sigma_{\hat{\mathbf{n}}}^{(2)}\rangle = 4\langle\hat{J}_{\hat{\mathbf{n}}}^2\rangle \tag{4.31}$$

from the indistinguishability between the spins 1/2. While the notion of symmetry breaking is usually associated to ferromagnetic phases, it is only true in the thermodynamic limit and we observe no spontaneous symmetry breaking in our finite-size system.

We expect entanglement to occur between the spins in the critical region [98] around $\lambda = 1$. This quantity is not directly accessible because we only simulate the 16 interacting spins by working with a large spin $J = 8$, although this question will

be addressed in more details in chapter 5. However entanglement can be indirectly probed by measuring spin correlations [99]. The populations along y and the correlator $\langle \sigma_y^{(1)} \sigma_y^{(2)} \rangle$ deduced from the variance are plotted on figure 4.13. For a separable state being symmetric upon spin exchange, correlators satisfy $\langle \sigma_{\hat{\mathbf{n}}}^{(1)} \sigma_{\hat{\mathbf{n}}}^{(2)} \rangle = \langle \sigma_{\hat{\mathbf{n}}}^{(1)} \rangle^2$ and are therefore positive [100]. However the value measured in figure 4.13 is negative, with higher values (in absolute value) near $\lambda/\omega_z = 1$, showing that the corresponding state is not separable, i.e. entangled.

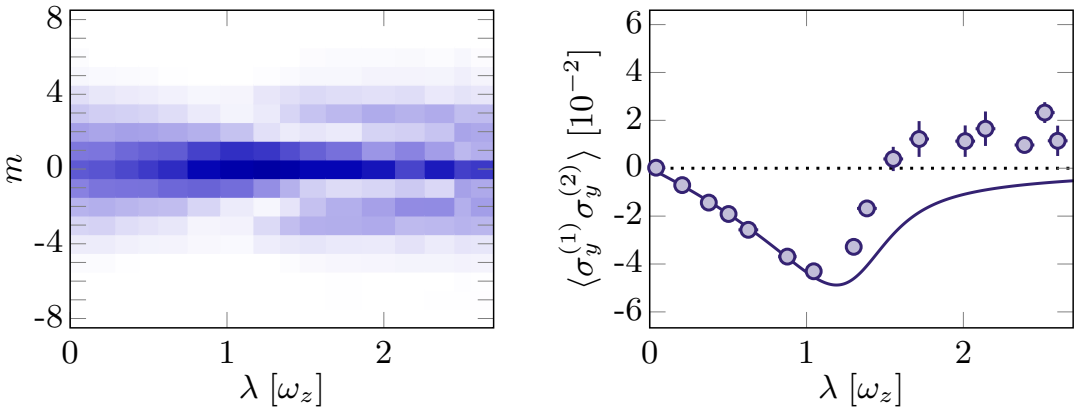

Figure 4.13 – Populations along y showing reduced variance in the critical region. (Left) Measured populations along y. This is the averaging of 5 measurements. We observe a reduction of variance in the critical region. **(Right)** Spin correlator along y deduced from the variance of the populations. The solid blue (resp. dotted black) line corresponds to the LMGm (resp. mean-field model) similarly to figure 4.12. Note that the correlator remains smaller than $5 \cdot 10^{-2}$ whereas it has values of order 1 along x (figure 4.12), hence the need for more averaging and the slight discrepancy between theory and experimental results.

Symmetry breaking

The state preparation can be strongly affected by the presence of a small magnetic field bias along x, the corresponding energy term $-\hbar\omega_x \hat{J}_x$ lifting the degeneracy between $|-J\rangle_x$ and $|+J\rangle_x$. This phenomenon is illustrated with an effective potential plotted on figure 4.14. The order parameter $\langle \sigma_x^{(1)} \rangle$ is proportional to the average magnetization $m_x = \langle \hat{J}_x \rangle$ as $\langle \hat{J}_{\hat{\mathbf{n}}} \rangle = J \langle \sigma_{\hat{\mathbf{n}}}^{(1)} \rangle$. In the ferromagnetic phase for $\lambda > 1$, it stays in the symmetric state $\langle \sigma_x^{(1)} \rangle = 0$ only on a very narrow region where ω_x is sufficiently small. Away from the line $\omega_x = 0$, a bias field corresponding to $\omega_x/\omega_z < 1/100$ is enough to make the state 'fall' in the minimum of potential as illustrated by the green curves.

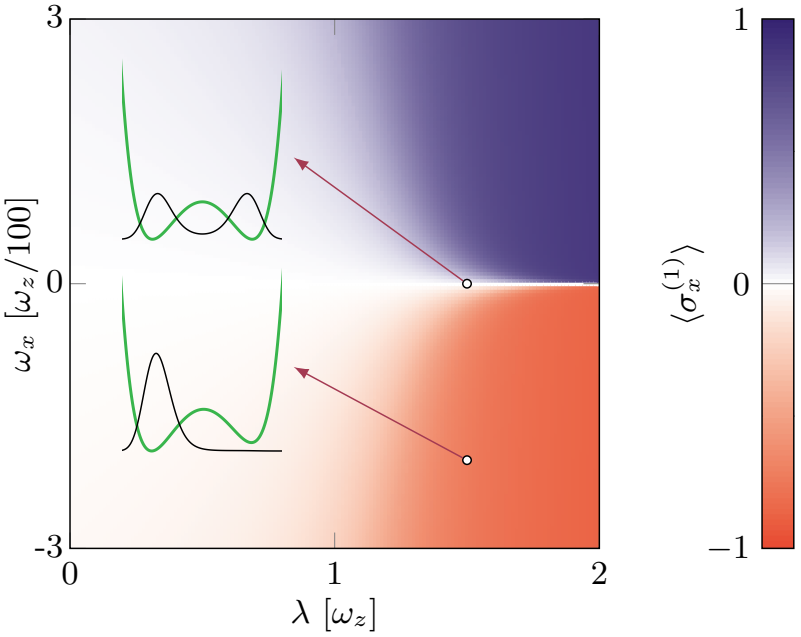

Figure 4.14 – Symmetry breaking illustrated by the tilting of a potential. The order parameter $\langle\sigma_x^{(1)}\rangle$ is plotted in color scale as a function of ω_x and λ. This is the result of computations. One can see that the transition between positive and negative values is sharp at $\lambda = 2$ but becomes smoother as λ approaches 1. **(Inset)** Effective potential (green) and corresponding wavefunction (black) in the symmetric and symmetry-broken cases.

This behaviour is characterized in figure 4.15(a,b) where a magnetic field bias along x is applied during the state preparation, for $\lambda/\omega_z = 1.40(3)$. The system 'picks a side' based on the sign of ω_x, with a smoothened region in the center. $\langle\sigma_x^{(1)}\rangle$ saturates to a value smaller than 1 because the value of λ used here cannot guarantee that only the states $|\pm J\rangle_x$ are populated (similarly to figure 4.12). The mean-field approach predicts an infinitely sharp transition between the two sides.

We then set the value of ω_x to zero with as much precision as possible and perform very slow ramps of the ferromagnetic coupling $\dot{\lambda} = 10^{-3}\omega_z^2$ so that the system gets sensitive to the magnetic field noise along x. We repeat this procedure to obtain 100 shots for four different values of λ and plot the result on figure 4.15(c). While at low values of λ the ground state is always $|-J\rangle_z$, in the ferromagnetic phase the system randomly ends up on the positive or negative sides, based on the sign of ω_x set by the noise during the preparation. This procedure works as intended because the state preparation lasts typically 1 ms while the magnetic field noise varies on much larger timescales, inducing only shot-to-shot variations. The magnetic field bias induced by the slowly varying noise was independently measured. We could see that for large values of λ, small fluctuations of the magnetic field along x were correlated with the order parameter of the prepared state.

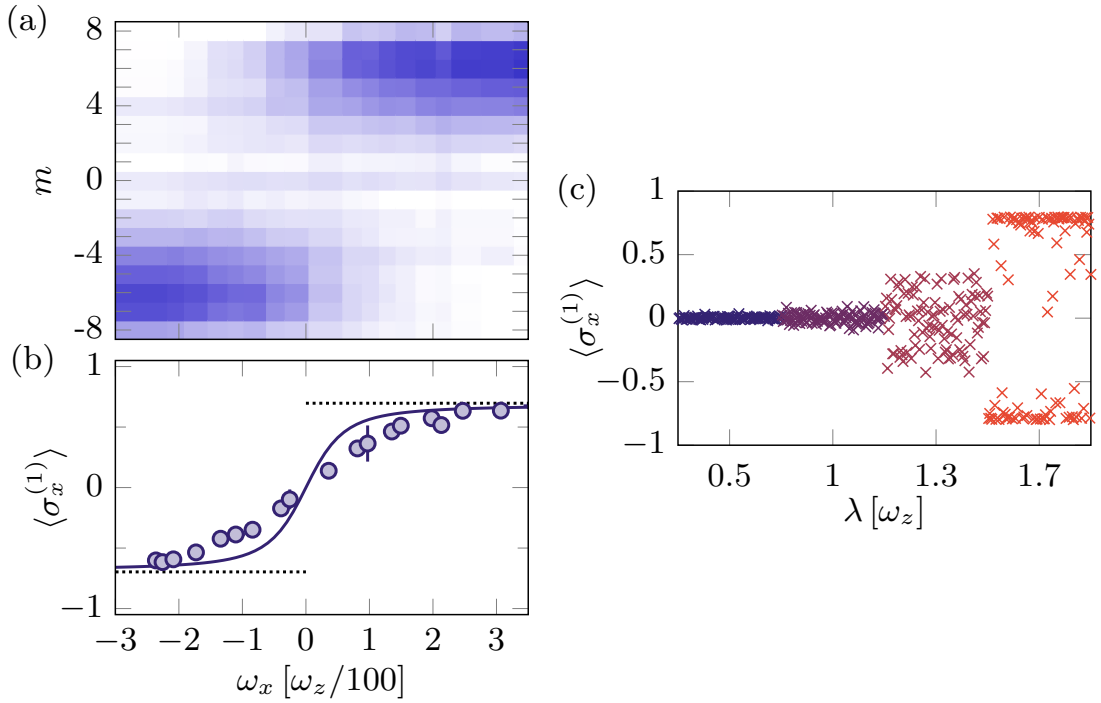

Figure 4.15 – Measurements showing the symmetry breaking. **(a)** Populations along x as a function of the bias field ω_x for $\lambda = 1.40(3)$. **(b)** Order parameter computed from the average of the populations plotted in (a). The solid blue (resp. dotted black) line corresponds to the LMGm (resp. mean-field model). **(c)** Order parameter of the state prepared under the effect of magnetic field noise. Each of the four colors represents a set of 100 measurements, for four different values of λ.

These results demonstrate the relevance of our device as a magnetic field sensor. This illustrates the metrological interest of this system of 16 indistinguishable interacting spins 1/2 realized with the large spin $J = 8$ of dysprosium.

Part III

Perspectives

Chapter 5

Pairwise entanglement

In this chapter we are interested in quantifying the 'amount of entanglement' that is present in various states of a total spin J. We have already described in section 4.2.1 how such a state can be seen as a collection of $2J$ qubits in a symmetrized state. The simplest case of entanglement is defined for a pair of qubits which is why we want to use this formalism to describe an arbitrary spin J. Entanglement in this case will therefore be referred to as pairwise entanglement.

We intend to show how quantum correlations between the fictitious spins 1/2 can be extracted to probe pairwise entanglement. First we introduce the notion of *concurrence* and explain how such a figure of merit is useful to quantify pairwise entanglement. Then we define the reduced two-qubit density matrix describing the quantum state of a pair of qubits extracted from the set of 2J qubits. We show that this density matrix can be obtained from the probability of light absorption by an atom. The absorption process for a transition $J \to J-1$ can be viewed as the extraction of two qubits out of the set of 2J qubits, in a state defined by the light polarization. Finally we are able to propose an experimental protocol to extract the concurrence from photon absorption measurements.

5.1 Defining entanglement

Entanglement has been extensively studied in the particular case of qubits for several reasons. On the one hand they play a central role in fundamental tests of quantum mechanics, in particular the violation of Bell inequalities [101]. On the other hand the main features of quantum technologies and metrology such as quantum parallelism or squeezing are based on entanglement as it is a phenomenon which is absent from classical physics.

5.1.1 Indirect definition based on separability

A general definition of entanglement relies on the notion of separability of a state. If one considers a system composed of two subsystems with respective Hilbert spaces $\mathcal{H}_A$ and $\mathcal{H}_B$ and given states $|\psi\rangle_A$ and $|\varphi\rangle_B$ of these two systems, then the state of the global system is described by $|\psi\rangle_A \otimes |\varphi\rangle_B$. Such a state is called a separable state. However a given state of $\mathcal{H}_A \otimes \mathcal{H}_B$ may not necessarily be separable (written as a product state) in which case it is said to be entangled. It therefore

exhibits correlations between the two subsystems, in particular the outcome of a measurement performed on $\mathcal{H}_A$ gives information about the state of $\mathcal{H}_B$.

This definition of entanglement is not really practical in the sense that it is indirect and characterizes an entangled state by the fact that it does not have a given property, the separability. It does not characterize the 'amount' of entanglement of a given state.

5.1.2 The notion of concurrence

A way to define the entanglement of a bipartite system is to compute the von Neumann entropy of either of its two parts [102] i.e. $E(\psi) = -\mathrm{Tr}\,\rho \log \rho$ where ρ is the partial trace of $|\psi\rangle\langle\psi|$ over one of the subsystems. The entropy computed this way does not depend on the choice of the subsystem that we trace over. However it is not very convenient, especially in the context of indistinguishable spins viewed as symmetrized multiple qubits states because one does not know which spin should be traced out.

A quantity called the concurrence [103] has very useful properties and can be used to quantify entanglement. While a two-qubit state is usually decomposed on the basis $\{|\uparrow\uparrow\rangle, |\downarrow\downarrow\rangle, |\uparrow\downarrow\rangle, |\downarrow\uparrow\rangle\}$, we introduce another basis, which is nothing but the Bell states with additional global phases :

$$\begin{cases} |e_1\rangle = (|\uparrow\uparrow\rangle + |\downarrow\downarrow\rangle)/\sqrt{2} \\ |e_2\rangle = i(|\uparrow\uparrow\rangle - |\downarrow\downarrow\rangle)/\sqrt{2} \\ |e_3\rangle = i(|\uparrow\downarrow\rangle + |\downarrow\uparrow\rangle)/\sqrt{2} \\ |e_4\rangle = (|\uparrow\downarrow\rangle - |\downarrow\uparrow\rangle)/\sqrt{2} \end{cases}$$

If we decompose a state $|\psi\rangle$ on this basis as $|\psi\rangle = \sum_i \alpha_i |e_i\rangle$, we can define the concurrence as

$$C(\psi) = \left| \sum_i \alpha_i^2 \right| \tag{5.1}$$

which ranges from 0 to 1.

It can be shown [103] that the concurrence is related in a monotonic way to the Von-Neumann entropy, such that it is a good figure of merit to measure the amount of entanglement in a two-qubit state.

The concurrence can also be computed directly from the two-qubit density matrix ρ_{12} and will be more useful for us. Note that the following formula is also valid in the case of mixed systems, even though we are dealing only with pure states in our case. From ρ_{12} one can construct the matrix $R \equiv \rho_{12}\,(\sigma_y \otimes \sigma_y)\,\rho_{12}^*\,(\sigma_y \otimes \sigma_y)$ where $\sigma_y \otimes \sigma_y$ is a four-by-four matrix. If we label $\lambda_1 \geq \lambda_2 \geq \lambda_3 \geq \lambda_4$ the four eigenvalues of R, it can be shown [103] that

$$C = \max(0, \sqrt{\lambda_1} - \sqrt{\lambda_2} - \sqrt{\lambda_3} - \sqrt{\lambda_4}). \tag{5.2}$$

5.2 Symmetrized two-qubit density matrix

We already saw that considering only symmetric states of a collection of $2J$ qubits led to a Hilbert space of reduced dimension $2J+1$. The same applies here for two qubits and leads to a Hilbert space of dimension 3 corresponding to the structure of a spin 1. We have to consider symmetrized two-qubit states in our study of the pairwise entanglement of a spin J because the qubits are fictitious and therefore indistinguishable.

5.2.1 Definition

The three-by-three symmetrized two-qubit density matrix ρ_{12}^{S} relates to a general four-by-four two-qubit density matrix in the following way :

$$\rho_{12} = \begin{pmatrix} a_{1,1} & a_{1,0}/\sqrt{2} & a_{1,0}/\sqrt{2} & a_{1,-1} \\ a_{0,1}/\sqrt{2} & a_{0,0}/2 & a_{0,0}/2 & a_{0,-1}/\sqrt{2} \\ a_{0,1}/\sqrt{2} & a_{0,0}/2 & a_{0,0}/2 & a_{0,-1}/\sqrt{2} \\ a_{-1,1} & a_{-1,0}/\sqrt{2} & a_{-1,0}/\sqrt{2} & a_{-1,-1} \end{pmatrix} \tag{5.3}$$

where $a = \rho_{12}^{\mathrm{S}}$ is written in the $|J=1, m=1,0,-1\rangle$ basis. ρ_{12} is expressed in the usual $|\uparrow\uparrow\rangle, |\uparrow\downarrow\rangle, |\downarrow\uparrow\rangle, |\downarrow\downarrow\rangle$ basis. This result directly comes from the fact that $|J=1, m=0\rangle = (|\uparrow\uparrow\rangle + |\downarrow\downarrow\rangle)/\sqrt{2}$.

5.2.2 Link to an arbitrary spin J

In the following we only consider symmetrized states of the system. Therefore the most convenient basis is that of the spin J for the full system, and that of the spin 1 for the symmetrized state of two qubits. To obtain the two-qubit density matrix we need to perform a partial trace on $2J-2$ qubits 'in a symmetric way' to keep only the remaining two. This is equivalent to describing the spin J as a combination of spins $J-1$ and 1 and tracing out the $J-1$ part. If we write $\rho = |\psi\rangle\langle\psi|$ the density matrix of the spin J and $|e_i\rangle$ a basis for the spin $J-1$, then

$$\begin{aligned} \rho_{12}^{\mathrm{S}} &= \sum_i \langle e_i|\, \rho\, |e_i\rangle \\ &= \sum_{m=-(J-1)}^{J-1} \langle J-1, m|\psi\rangle\, \langle\psi|J-1, m\rangle \end{aligned}$$

where $\langle J-1, m|\psi\rangle$ is the 'remaining part' corresponding to the spin 1 and is therefore a ket living in the corresponding three dimensional Hilbert space. Then we can write the different coefficients $\langle q'|\rho_{12}^{\mathrm{S}}|q\rangle$ of ρ_{12}^{S} for $q, q' = -1, 0, 1$ as

$$\langle q'|\rho_{12}^{\mathrm{S}}|q\rangle = \langle 1, q'| \sum_{m=-(J-1)}^{J-1} \langle J-1, m|\psi\rangle\, \langle\psi|J-1, m\rangle\, |1, q\rangle \tag{5.4}$$

$$= \sum_{m=-(J-1)}^{J-1} \langle J-1, m\,; 1, q'|\psi\rangle\, \langle\psi|J-1, m\,; 1, q\rangle \tag{5.5}$$

where $|J-1, m\,; 1, q\rangle$ is to be understood as a state of a spin J, for a given substate m (resp. q) of the spin $J-1$ (resp. 1).

This formula can be rewritten in a more compact way by using symmetrized states (i.e. states of a spin J) as

$$\langle q'|\rho_{12}^{\mathrm{S}}|q\rangle = \sum_{m=-(J-1)}^{J-1} c_{q,\,m}\, c_{q',\,m}\, \langle J, m+q'|\psi\rangle\, \langle\psi|J, m+q\rangle \tag{5.6}$$

where the coefficient

$$c_{q,\,m} = \left[\frac{\binom{2}{q+1}\binom{2J-2}{J+m-1}}{\binom{2J}{J+m+q}}\right]^{1/2} \tag{5.7}$$

comes from combinatorials accounting for the symmetrization of the $2J$-, $(2J-2)$- and 2-qubit vectors similarly to the explicit basis given in section 4.2.1.

5.3 Probing pairwise entanglement using atom-light interaction

We now consider an atom prepared in an electronic state $|\psi\rangle$ of angular momentum J coupled through resonant light to an excited electronic state of angular momentum $J' = J-1$. We show how the photon absorption probability is related to the symmetrized two-qubit density matrix.

5.3.1 Photon absorption probability

The states $|\psi\rangle$ and $|\psi'\rangle$ of the unperturbed atomic Hamiltonian $\hat{H}_0$ (with energies E and E') are coupled through a perturbation term. In this case the perturbation is the atom-light interaction

$$\hat{V} = -\hat{\boldsymbol{d}}\cdot\boldsymbol{E} = -\frac{1}{2}E\,\hat{\boldsymbol{d}}\cdot\boldsymbol{\epsilon}\,e^{-i\omega t} - \frac{1}{2}E^*\,\hat{\boldsymbol{d}}\cdot\boldsymbol{\epsilon}^*\,e^{i\omega t} \tag{5.8}$$

where E is the field amplitude, $\boldsymbol{\epsilon}$ the polarization vector and ω the light frequency. We can compute the probability of transfer $W_{|\psi'\rangle}(t)$ (that is, the probability to find the system in state $|\psi'\rangle$ at time t) using first order perturbation theory, assuming the coupling is turned on abruptly at $t=0$. We also assume that t remains smaller than the lifetime of the excited state and therefore neglect spontaneous emission so that

$$\begin{aligned} W_{|\psi'\rangle}(t) &= \frac{1}{\hbar^2}\left|\int_0^t \mathrm{d}t' e^{i(E'-E)t'/\hbar}\,\langle\psi'|\hat{V}(t')|\psi\rangle\right|^2 \\ &= \frac{1}{4\hbar^2}\left|E\,\langle\psi'|\hat{\boldsymbol{d}}\cdot\boldsymbol{\epsilon}|\psi\rangle\,\frac{e^{i(\omega_0-\omega)t}-1}{\omega_0-\omega} + E^*\,\langle\psi'|\hat{\boldsymbol{d}}\cdot\boldsymbol{\epsilon}^*|\psi\rangle\,\frac{e^{i(\omega_0+\omega)t}-1}{\omega_0+\omega}\right|^2, \end{aligned}$$

where $\omega_0 = (E'-E)/\hbar$. In the following we neglect the counter rotating term $\omega_0+\omega$ since we assumed resonant coupling $|\omega_0-\omega| \ll \omega_0, \omega$. By performing an expansion for small t the transfer rate therefore reduces to

$$W_{|\psi'\rangle}(t) = \frac{|E|^2t^2}{4\hbar^2}\left|\langle\psi'|\hat{\boldsymbol{d}}\cdot\boldsymbol{\epsilon}|\psi\rangle\right|^2. \tag{5.9}$$

Since there are several states $|\psi'\rangle$ coupled to the initial state $|\psi\rangle$ through the atom-light coupling, the probability of absorbing a photon after a short time t reads

$$P_{\text{abs}} = \frac{|E|^2 t^2}{4\hbar^2} \sum_{|\psi'\rangle} \left| \langle \psi' | \hat{\boldsymbol{d}} \cdot \boldsymbol{\epsilon} | \psi \rangle \right|^2 . \tag{5.10}$$

We introduce the *spherical basis* in which we are going to decompose the electric field and dipole operator. This is a natural basis for circular polarization as can be seen from its structure. From the usual cartesian basis $(\boldsymbol{e}_x, \boldsymbol{e}_y, \boldsymbol{e}_z)$ we define the three basis vectors $\boldsymbol{e}_-$, $\boldsymbol{e}_0$ and $\boldsymbol{e}_+$ as

$$\begin{aligned} \boldsymbol{e}_+ &= \frac{-1}{\sqrt{2}}(\boldsymbol{e}_x + i\boldsymbol{e}_y) \\ \boldsymbol{e}_- &= \frac{1}{\sqrt{2}}(\boldsymbol{e}_x - i\boldsymbol{e}_y) \\ \boldsymbol{e}_0 &= \boldsymbol{e}_z \end{aligned}$$

and write $\hat{\boldsymbol{d}} = \sum_{q=-1,0,1} \hat{d}_q \boldsymbol{e}_q$ and in the same way $\boldsymbol{\epsilon} = \sum_q \epsilon_q \boldsymbol{e}_q$.

The fact that $\hat{\boldsymbol{d}}$ is hermitian and the conjugation rules in the spherical basis lead to $\hat{\boldsymbol{d}} \cdot \boldsymbol{\epsilon} = \sum_q (-1)^q \hat{d}_q \epsilon_{-q}$ and $(\hat{\boldsymbol{d}} \cdot \boldsymbol{\epsilon})^\dagger = \sum_q (-1)^q \hat{d}_q (\epsilon^*)_{-q}$. The accessible states $|\psi'\rangle$ are $|J', m'\rangle$ for $m' = -(J-1), ..., (J-1)$. Then

$$\begin{aligned} P_{\text{abs}} &= \frac{|E|^2 t^2}{4\hbar^2} \sum_{|\psi'\rangle} \langle\psi| \sum_{q'} (-1)^{q'} \hat{d}_{q'} (\epsilon^*)_{-q'} |\psi'\rangle \langle\psi'| \sum_q (-1)^q \hat{d}_q \epsilon_{-q} |\psi\rangle \\ &= \frac{|E|^2 t^2}{4\hbar^2} \sum_{q,\, q',\, m'} (-1)^{q+q'} (\epsilon^*)_{-q'} \epsilon_{-q} \langle\psi| \hat{d}_{q'} |J-1, m'\rangle \langle J-1, m'| \hat{d}_q |\psi\rangle \\ &= \frac{|E|^2 t^2}{4\hbar^2} \sum_{q,\, q'} (-1)^{q+q'} (\epsilon^*)_{-q'} \epsilon_{-q} \, a_{q,q'} \end{aligned} \tag{5.11}$$

where we add the projector on the J manifold $\sum_m |J, m\rangle \langle J, m|$ acting on $|\psi\rangle$, which is nothing but the identity on this subspace, to define $a_{q,q'}$ as

$$a_{q,q'} = \sum_{m_1,\, m_2,\, m'} \langle\psi|J, m_1\rangle \langle J, m_1|\hat{d}_{q'}|J-1, m'\rangle \langle J-1, m'|\hat{d}_q|J, m_2\rangle \langle J, m_2|\psi\rangle .$$

We can make use of the Wigner-Eckart theorem to transform the expression of $a_{q,q'}$. Since $\hat{d}_q$ is a tensor operator (which we write $\hat{d}_{1,q}$ to make it more apparent), we can write its matrix elements in a reduced form using a coefficient independent from q (hence the dropped index) and Clebsch-Gordan coefficients as

$$\begin{aligned} \langle J-1, m'|\hat{d}_{1,q}|J, m_2\rangle &= \langle J-1||\boldsymbol{d}||J\rangle \langle J, m_2\,; 1, q|J-1, m'\rangle \\ &= \langle J-1||\boldsymbol{d}||J\rangle (-1)^q \sqrt{\frac{2J-1}{2J+1}} \langle J, m_2|J-1, m'\,; 1, -q\rangle \\ &= \langle J-1||\boldsymbol{d}||J\rangle (-1)^q \sqrt{\frac{2J-1}{2J+1}} \langle J-1, m'\,; 1, -q|J, m_2\rangle \end{aligned}$$

where we used the fact that the Clebsch-Gordan coefficients are real numbers, and in the same way

$$\begin{aligned}\langle J, m_1|\hat{d}_{1,q'}|J-1, m'\rangle &= \langle J-1, m'|\hat{d}_{1,q'}|J, m_1\rangle^* \\ &= \langle J-1||\boldsymbol{d}||J\rangle^* (-1)^{q'} \sqrt{\frac{2J-1}{2J+1}} \langle J, m_1|J-1, m'; 1, -q'\rangle^* \\ &= \langle J-1||\boldsymbol{d}||J\rangle^* (-1)^{q'} \sqrt{\frac{2J-1}{2J+1}} \langle J, m_1|J-1, m'; 1, -q'\rangle .\end{aligned}$$

We introduce the notation $d_{J-1,\,J} = \langle J-1||\boldsymbol{d}||J\rangle$ for simplicity and we can then write

$$\begin{aligned}a_{q,q'} = (-1)^{q+q'} \frac{2J-1}{2J+1} |d_{J-1,\,J}|^2 \sum_{m_1,\,m_2,\,m'} &\langle\psi|J, m_1\rangle \langle J, m_1|J-1, m'; 1, -q'\rangle \\ &\times \langle J-1, m'; 1, -q|J, m_2\rangle \langle J, m_2|\psi\rangle\end{aligned}$$

which, by identifying the sums over m_1 and m_2 as the identity acting on $|\psi\rangle$ reduces to

$$\begin{aligned}a_{q,q'} &= (-1)^{q+q'} \frac{2J-1}{2J+1} |d_{J-1,\,J}|^2 \sum_{m'} \langle\psi|J-1, m'; 1, -q'\rangle \langle J-1, m'; 1, -q|\psi\rangle \\ &= (-1)^{q+q'} \frac{2J-1}{2J+1} |d_{J-1,\,J}|^2 \langle -q|\rho_{12}^{\mathrm{S}}|-q'\rangle \qquad (5.12)\end{aligned}$$

where we used equation (5.5). We finally find the link between the probability to absorb a photon according to its helicity and the corresponding coefficients of the symmetrized two-qubit density matrix as

$$\begin{aligned}P_{\mathrm{abs}} &= \frac{|E|^2 t^2}{4\hbar^2} \frac{2J-1}{2J+1} |d_{J-1,\,J}|^2 \sum_{q,\,q'} (\epsilon^*)_{-q'}\, \epsilon_{-q}\, \langle -q|\rho_{12}^{\mathrm{S}}|-q'\rangle \\ &= (\Omega t)^2 \sum_{q,q'} (\epsilon^*)_{q'}\, \epsilon_q\, \langle q|\rho_{12}^{\mathrm{S}}|q'\rangle \\ &= (\Omega t)^2 \langle\epsilon^*|\rho_{12}^{\mathrm{S}}|\epsilon^*\rangle \qquad (5.13)\end{aligned}$$

where $\Omega = \dfrac{|E||d_{J-1,\,J}|}{2\hbar} \sqrt{\dfrac{2J-1}{2J+1}}$ is the coupling strength and we identified the sum over q and q' to the matrix product $\langle\epsilon^*|\rho_{12}^{\mathrm{S}}|\epsilon^*\rangle$ where the ket notation $|\epsilon\rangle$ for the polarization is a vector containing the three components ϵ_+, ϵ_0 and ϵ_-.

This result can be interpreted by considering the state $|\psi\rangle$ of a spin 1 corresponding to $|\psi\rangle\langle\psi| = \rho_{12}^{\mathrm{S}}$ such that $\langle\epsilon^*|\rho_{12}^{\mathrm{S}}|\epsilon^*\rangle = |\langle\psi|\epsilon^*\rangle|^2$. The photon is absorbed if there is a mode matching between $|\psi\rangle$ and $|\epsilon^*\rangle$.

5.3.2 A well-chosen basis for the symmetrized two-qubit density matrix

Different photon-absorption experiments should enable us to reconstruct ρ_{12}^{S}. There are 8 independent real coefficients a_i to determine writing ρ as

$$\rho = \frac{1}{3}\mathbb{1} + \frac{1}{2}\sum_{i=1}^{8} a_i M_i \qquad (5.14)$$

where the identity plus these 8 matrices form a basis of three-by-three hermitian matrices of trace one :

$$M_1 = \frac{1}{\sqrt{2}}\begin{pmatrix} 0 & 1 & 0 \\ 1 & 0 & 1 \\ 0 & 1 & 0 \end{pmatrix} \qquad M_2 = \frac{1}{\sqrt{2}}\begin{pmatrix} 0 & -i & 0 \\ i & 0 & -i \\ 0 & i & 0 \end{pmatrix} \qquad M_3 = \begin{pmatrix} 1 & 0 & 0 \\ 0 & 0 & 0 \\ 0 & 0 & -1 \end{pmatrix}$$

$$M_4 = \begin{pmatrix} 0 & 0 & 1 \\ 0 & 0 & 0 \\ 1 & 0 & 0 \end{pmatrix} \qquad M_5 = \begin{pmatrix} 0 & 0 & -i \\ 0 & 0 & 0 \\ i & 0 & 0 \end{pmatrix} \qquad M_6 = \frac{1}{\sqrt{2}}\begin{pmatrix} 0 & -i & 0 \\ i & 0 & i \\ 0 & -i & 0 \end{pmatrix}$$

$$M_7 = \frac{1}{\sqrt{2}}\begin{pmatrix} 0 & 1 & 0 \\ 1 & 0 & -1 \\ 0 & -1 & 0 \end{pmatrix} \qquad M_8 = \frac{1}{\sqrt{3}}\begin{pmatrix} 1 & 0 & 0 \\ 0 & -2 & 0 \\ 0 & 0 & 1 \end{pmatrix}$$

These matrices are similar to the Gell-Mann matrices and they also correspond to operators of a spin $L = 1$ expressed in the basis formed by the eigenstates of $\hat{\boldsymbol{L}}^2$ and $\hat{L}_z$: $|1\rangle$, $|0\rangle$, $|-1\rangle$ as

$$M_1 = \hat{L}_x, \qquad M_2 = \hat{L}_y, \qquad M_3 = \hat{L}_z,$$

$$M_4 = \hat{L}_x^2 - \hat{L}_y^2,$$

$$M_5 = \hat{L}_x\hat{L}_y + \hat{L}_y\hat{L}_x, \qquad M_6 = \hat{L}_y\hat{L}_z + \hat{L}_z\hat{L}_y, \qquad M_7 = \hat{L}_z\hat{L}_x + \hat{L}_x\hat{L}_z,$$

$$M_8 = \frac{1}{\sqrt{3}}\big(-2\,\mathbb{1} + 3\,\hat{L}_z^2\big).$$

5.4 Proposed experimental implementation

The electronic transition of dysprosium at $\lambda = 696$ nm couples the ground state $J = 8$ to an excited state $J' = J - 1$ and is therefore suited for this experiment. Its linewidth $\Gamma = 2\pi \times 15$ kHz corresponds to an excited state lifetime $\Gamma^{-1} = 10.6\,\mu$s, meaning that the resonant light pulse should remain smaller than 1 µs for the short time approximation to be valid. The coupling Ω can be more easily computed by expressing the dipole coupling $d_{J-1,\,J}$ using

$$\Gamma = \frac{\omega_0^3}{3\pi\epsilon_0\hbar c^3}|d_{J-1,\,J}|^2 \tag{5.15}$$

so that

$$\Omega^2 = \frac{3\pi\Gamma c^2}{2\omega_0^3}\,\frac{I_0}{\hbar}\,\frac{2J-1}{2J+1} \tag{5.16}$$

where we used $|E|^2/4 = I_0/(2\epsilon_0 c)$. For a waist of 50 µm and a power of 100 mW, we get $\Omega = 2\pi \times 104$ MHz. This means that even if the laser producing light at 696 nm

is not stable down to the level of Γ, the natural laser stability measured at $\sim$5 MHz is sufficient to address the transition in a reliable way thanks to power broadening.

5.4.1 Choice of light polarization

Linear polarization

From equation 5.13 and using the basis decomposition of equation 5.14, we obtain that for a linear polarization $\boldsymbol{\epsilon} = \boldsymbol{e}_{\theta,\phi}$ the probability to absorb a photon reads

$$\frac{P_{\text{abs}}(\boldsymbol{e}_{\theta,\phi})}{P_0} = \frac{1}{3} - \frac{a_8}{4\sqrt{3}} - \frac{a_4}{2}\sin^2\theta\cos(2\phi) + \frac{a_5}{2}\sin^2\theta\sin(2\phi) + \frac{a_6}{2}\sin(2\theta)\sin\phi - \frac{a_7}{2}\sin(2\theta)\cos\phi - \frac{a_8\sqrt{3}}{4}\cos(2\theta) \quad (5.17)$$

where $P_0 = (\Omega t)^2$. It allows to determine coefficients a_4 to a_8 from measurements along different directions. When defining the polarization in such a way, we assume that the light propagates along a line orthogonal to a plane containing the polarization vector. This choice is not unique. While this a priori requires the ability to send a linearly polarized laser beam on the atoms along various directions, the use of magnetic rotations mapping the z axis onto any direction (similarly to the ones described in section 3.3.1) allows us to use only one direction of propagation.

Circular polarization

In the case where $\boldsymbol{\epsilon} = \boldsymbol{e}_{\pm}$, meaning that the polarization is circular and the light is propagating along z, we get

$$\frac{P_{\text{abs}}(\boldsymbol{e}_{\pm})}{P_0} = \frac{1}{3} \mp \frac{a_3}{2} + \frac{a_8}{2\sqrt{3}} \quad (5.18)$$

so that a_3 can be extracted as

$$a_3 = \frac{P_{\text{abs}}(\boldsymbol{e}_{-}) - P_{\text{abs}}(\boldsymbol{e}_{+})}{P_0}. \quad (5.19)$$

The same is true for a_1 and a_2, choosing circularly polarized light propagating respectively along x and y. If we write $\boldsymbol{e}_{\pm,\theta,\phi}$ the polarization vector corresponding to a circularly polarized light propagating along the direction (θ, ϕ), we can write in the most general case

$$\frac{P_{\text{abs}}(\boldsymbol{e}_{-,\theta,\phi}) - P_{\text{abs}}(\boldsymbol{e}_{+,\theta,\phi})}{P_0} = \sin\theta\cos\phi\, a_1 + \sin\theta\sin\phi\, a_2 + \cos\theta\, a_3 \quad (5.20)$$

Once again the use of rotations on the Bloch sphere would enable us to use only one direction of propagation for the circularly polarized light.

5.4.2 Detection

The resonant light pulse would be followed by a time-of-flight with a typical duration of a few milliseconds. An atom which absorbs a photon acquires a velocity $v_{\text{rec}} = \hbar k/m = 3.5$ µm/ms in the direction of light propagation. Since the lifetime of

the excited state is typically 10 µs, the atom travels a negligible distance $v_{\mathrm{rec}}/\Gamma \simeq 40$ nm during this short time. Then a photon is spontaneously emitted, giving another v_{rec} kick in a random direction, resulting in a circular velocity distribution. After time-of-flight this velocity distribution leads to a ring-shaped atomic distribution plotted on figure 5.1. The propagation of scattered atoms needs to be compared with the thermal expansion of the atomic cloud at velocity $v_{\mathrm{th}} = \sqrt{k_B T/m}$. The cloud expansion needs to be smaller than the ring pattern so that they do not overlap. This yields the criterion $v_{\mathrm{th}} \leq v_{\mathrm{rec}}$, valid for $T \leq 250$ nK.

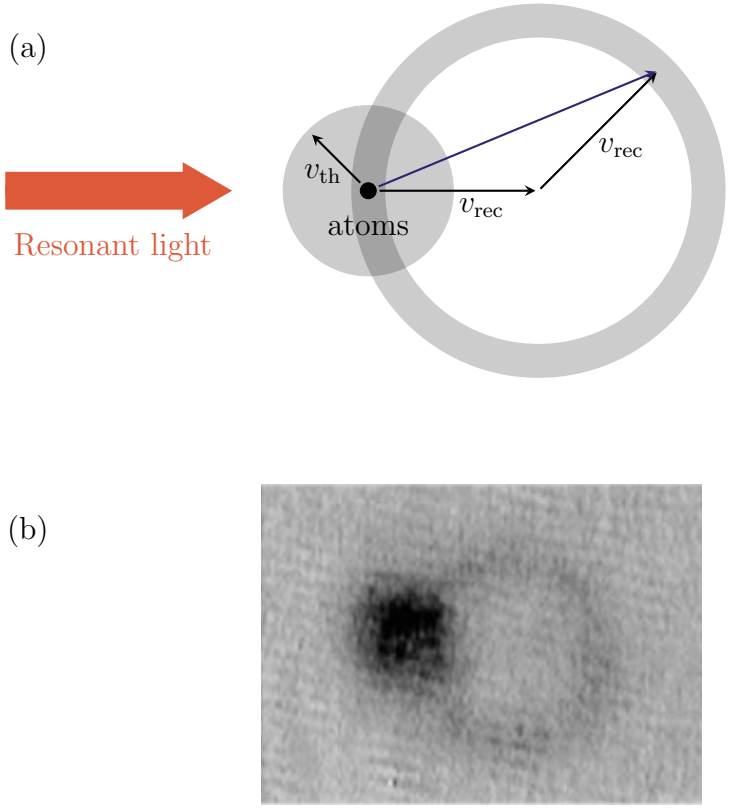

Figure 5.1 – Atomic distribution resulting from time-of-flight after photon absorption and spontaneous emission. (a) Schematic representation. The distance that an atom in the excited state travels before spontaneously emitting a photon is negligible and therefore not represented. The total velocity results from a first v_{rec} kick in the direction of the laser followed by a second v_{rec} kick in a random direction. The graph corresponds to $v_{\mathrm{th}} = 0.5\, v_{\mathrm{rec}}$ **(b) Picture** taken from [104], obtained with sodium atoms. The net displacement to the right due to the finite lifetime of the excited state is visible on the picture.

The number of atoms measured in the ring pattern after a resonant light pulse should be proportional to the total atom number and to the absorption probability

as

$$N_{\text{ring}} = P_{\text{abs}}(\boldsymbol{\epsilon}) N_{\text{tot}}. \tag{5.21}$$

Shot-to-shot fluctuations in atom number could be ignored by measuring N_{tot} and N_{ring} on each image. This leaves P_0 as the only parameter that remains to be calibrated.

5.5 Examples with different states

We briefly recall the successive steps to compute the pairwise entanglement of a state $|\psi\rangle$ of a spin J. First the three-by-three symmetrized two-qubit density matrix ρ_{12}^S is deduced from $\rho = |\psi\rangle\langle\psi|$ according to equation 5.6. Then the four-by-four matrix ρ_{12} is deduced from ρ_{12}^S using equation 5.3. Then we form the product $\rho_{12}\,(\sigma_y \otimes \sigma_y)\,\rho_{12}^*\,(\sigma_y \otimes \sigma_y)$ and the concurrence is computed from its eigenvalues according to equation 5.2.

5.5.1 Coherent state

For a coherent spin state $|\psi\rangle = |-J\rangle_z$, the symmetrized two-qubit density matrix reduces to a single coefficient

$$\rho_{12}^S = \begin{pmatrix} 0 & 0 & 0 \\ 0 & 0 & 0 \\ 0 & 0 & 1 \end{pmatrix} \tag{5.22}$$

from which the computed concurrence is $C = 0$ which is not surprising as a coherent state should not exhibit any entanglement. This corresponds to the a_i coefficients being all equal to zero except for $a_3 = -1$ and $a_8 = 1/\sqrt{3}$. Therefore the photon absorption probabilities read

$$\frac{P_{\text{abs}}(\boldsymbol{e}_{\theta,\phi})}{P_0} = \frac{1 - \cos(2\theta)}{4} \tag{5.23}$$

which cancels for $\theta = 0$ corresponding to $\boldsymbol{\epsilon} = \boldsymbol{e}_z$ and we also have

$$\frac{P_{\text{abs}}(\boldsymbol{e}_{+,z})}{P_0} = 1 \quad \text{and} \quad \frac{P_{\text{abs}}(\boldsymbol{e}_{-,z})}{P_0} = 0 \tag{5.24}$$

consistent with the absence of $m_J = -9$ or $m_J = -8$ levels in the $J = 7$ manifold as shown on figure 5.2. The specific case of the σ_+ polarization applied to the $|-8\rangle_z$ state can be used as a way to calibrate P_0. Indeed this is the only case (with the symmetric situation of σ_- polarized light sent on the state $|+8\rangle_z$) where $P_{\text{abs}} = P_0$. It corresponds to the maximum number of scattered atoms N_{ring} and can be used as a reference for other polarizations.

5.5.2 The W state

The state that has the maximum concurrence $C = 2/N = 1/J$ among symmetric states is the so-called W state $|\psi\rangle = |-J+1\rangle_z$ [105], also equal to $\big(|\uparrow\downarrow \ldots \downarrow\rangle +$

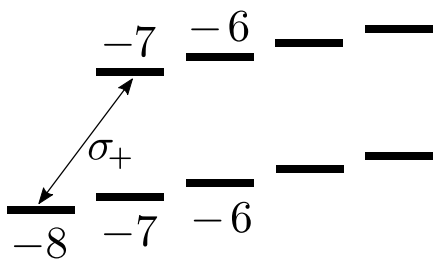

Figure 5.2 – Transition from the $J = 8$ to the $J = 7$ manifold.

$|\downarrow\uparrow ... \downarrow\rangle + ... + |\downarrow\downarrow ... \uparrow\rangle\big)/\sqrt{N}$ in the N qubits picture. The high degree of symmetry of the states considered in this chapter justifies the fact that the maximum value of the concurrence remains much smaller than one.

For the W state the reduced symmetrized density matrix is equal to

$$\rho_{12}^S = \begin{pmatrix} 0 & 0 & 0 \\ 0 & 1/8 & 0 \\ 0 & 0 & 7/8 \end{pmatrix} \tag{5.25}$$

and its concurrence is equal to 1/8. The values of the coefficients a_3 and a_8 obtained from ρ_{12}^S lead to the verification that

$$\frac{P_{\text{abs}}(\boldsymbol{e}_{-,z})}{P_0} = 0 \tag{5.26}$$

as expected from the absence of $m_J = -8$ state in the $J = 7$ manifold.

5.5.3 Cat state

For the cat state $|\psi\rangle = \big(|-J\rangle_z + |J\rangle_z\big)/\sqrt{2}$, the reduced matrix reads

$$\rho_{12}^S = \begin{pmatrix} 1 & 0 & 0 \\ 0 & 0 & 0 \\ 0 & 0 & 1 \end{pmatrix} \tag{5.27}$$

for which the concurrence is $C = 0$. This result suggests the need for carefulness when dealing with the notion of entanglement. While the cat state is said to be 'maximally-entangled', this is only true in terms of multipartite entanglement in the case where it is formed by N *real* qubits. When considering pairwise entanglement which is especially suited to our system of fictitious (and therefore indistinguishable) qubits, the cat state has a concurrence equal to zero.

The W state can be seen as the counterpart of the cat state. It has been shown in [106] that in three-qubit systems, multipartite-entangled states can be divided in two equivalence classes represented respectively by the cat state and the W state, showing their intrinsic difference. While for the cat state taking the partial trace over one of the qubits leads to a completely mixed state of the remaining two, for the W state the remaining pair is in a fully-entangled state.

A systematic numerical computation of the concurrence for the states prepared with the one-axis twisting Hamiltonian is given in [107]. On the other hand the presence of pairwise entanglement at the critical point for spin models similar to the LMGm is studied in [100, 108]. These two aspects could be realized experimentally by combining the results of this chapter with the results of chapters 3 and 4.

Chapter 6

Other projects, conclusion and outlook

The last chapter of this manuscript is dedicated to projects that extend the use of the spin degree of freedom of dysprosium by coupling it to external degrees of freedom.

The first project was realized in 2019 and I only provide a brief presentation of it as it has already been fully described in the thesis of T. Chalopin [42]. It consists in realizing an analogy of the two-dimensional Landau Hamiltonian of a charged particle in a magnetic field. This model is emblematic of quantum Hall systems exhibiting topological properties. In our case there is one dimension of space and one *synthetic dimension*, the internal (angular momentum) state playing the role of the second dimension, similarly to [109, 110]. The experimental results related to this project have been published in [111].

The second project is similar to the first one, except that there are two spatial dimensions, one of them being coupled to the atomic spin. This position-dependent internal state results in the presence of a Berry curvature playing the role of an artificial magnetic field.

6.1 Synthetic Hall system

6.1.1 Simulating the Landau Hamiltonian

Dysprosium is especially suited for the realization of artificial gauge fields, as the light-induced spin coupling may result in a coupling between the internal and external degrees of freedom, usually referred to as *spin-orbit* coupling. This requires the light field to be chosen such that its polarization and/or amplitude are position/momentum dependent. The system presented here can be considered as an extension of the light-induced spin squeezing realized in chapter 3, since it adds a spatial degree of freedom to the $2J + 1 = 17$ internal states of the ground state Zeeman manifold.

Usually the term *artificial gauge field* refers to systems that can be described by a Hamiltonian of the form

$$\hat{H} = \frac{\left(\hat{\boldsymbol{p}} - \boldsymbol{\mathcal{A}}(\hat{\boldsymbol{r}})\right)^2}{2m} \tag{6.1}$$

where $\boldsymbol{\mathcal{A}}(\hat{\boldsymbol{r}})$ is a vector potential, similarly to the Landau Hamiltonian

$$\hat{H}_{\text{Landau}} = \frac{\left(\hat{\boldsymbol{p}} - q\boldsymbol{A}(\hat{\boldsymbol{r}})\right)^2}{2m} \tag{6.2}$$

characterizing the dynamics of a charged particle in a magnetic field described by the associated vector potential $\boldsymbol{A}(\hat{\boldsymbol{r}})$. Realizing a system analogous to the Landau Hamiltonian with neutral atoms and light fields illustrates the principle of quantum simulation. Neutral atoms can be trapped, cooled and imaged relatively easily while electrons are more difficult to work with individually. Of course the difficult part is to mimic the interaction between a charged particle and a magnetic field with neutral atoms.

The scheme we use is similar to the one realized for the first time with effective two-levels atoms in [112]. Atoms are dressed by two counter-propagating Raman beams creating a momentum-dependent coupling between two internal atomic states. The Raman coupling scheme we use extends this idea to the case of dysprosium. It is based on a proposal related to the use of Raman beams to realize synthetic gauge fields with lanthanide atoms [113].

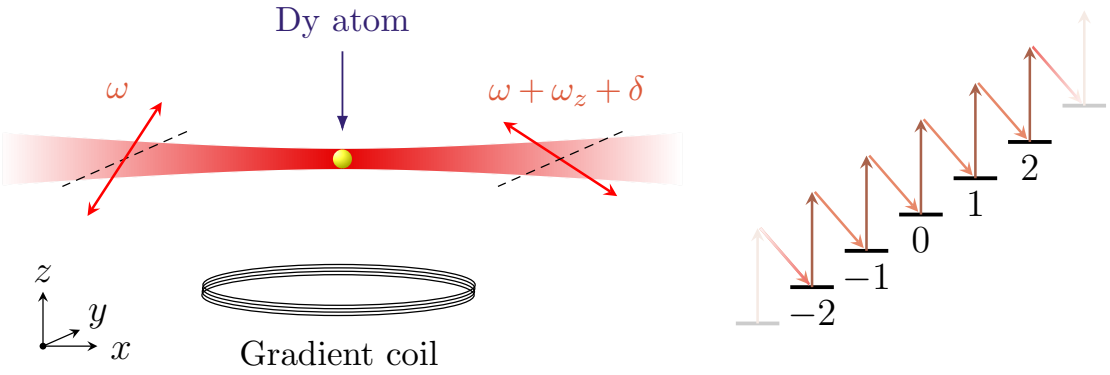

Figure 6.1 – Configuration of the Raman beams. A vertical magnetic field splits the m_J manifold and the two orthogonally polarized beams lead to Raman transfers in the entire ladder of states, with only a few represented. The detuning with the upper manifold is large (compared to the width Γ) to avoid any real excitation and consider only virtual processes.

The two Raman beams propagate along x and have linear polarizations tilted by 45 degrees with respect to the vertical quantization magnetic field $\boldsymbol{B} = B\hat{\boldsymbol{z}}$. One has frequency ω and the other $\omega + \omega_z + \delta$ as represented on figure 6.1. The sum of these two light fields results in a position-dependent light polarization as

$$\boldsymbol{\epsilon} = \frac{1}{2} e^{-i\omega_0 t}\left[e^{ikx}(\hat{\boldsymbol{y}} + \hat{\boldsymbol{z}}) + e^{-i(kx + \omega_z t + \delta t)}(\hat{\boldsymbol{y}} - \hat{\boldsymbol{z}})\right] \tag{6.3}$$

resulting for the light-shift Hamiltonian presented in equation 1.7 in

$$\hat{V} = V_0\left[\alpha^s \mathbb{1} + \alpha^v \sin(\phi)\frac{\hat{J}_x}{2J} + \alpha^t \frac{\hat{\boldsymbol{J}}^2 - 3\hat{J}_x^2 + 3\cos(\phi)(\hat{J}_y^2 - \hat{J}_z^2)}{2J(2J-1)}\right] \tag{6.4}$$

where the light coupling V_0 and phase ϕ are given by

$$V_0 = \frac{3\pi\Gamma c^2}{2\omega_0^3}\frac{\sqrt{I_1 I_2}}{\Delta} \tag{6.5}$$

$$\phi = 2kx + (\omega_z + \delta)t, \tag{6.6}$$

I_1 and I_2 being the intensities of the Raman beams. The total Hamiltonian is given by

$$\hat{H} = \frac{\hat{\boldsymbol{p}}^2}{2m} + \hbar\omega_z \hat{J}_z + \hat{V} \tag{6.7}$$

and we perform a unitary transformation corresponding to

$$|\tilde{\psi}\rangle = \hat{U}\,|\psi\rangle = \exp\left(i(\omega_z + \delta)t\hat{J}_z\right)|\psi\rangle \tag{6.8}$$

which also transforms the Hamiltonian according to

$$\tilde{H} = i\hbar\frac{d\hat{U}}{dt}\hat{U}^\dagger + \hat{U}\hat{H}\hat{U}^\dagger. \tag{6.9}$$

The point of this transformation is to isolate rapidly oscillating terms to perform the rotating wave approximation (RWA) and neglect them. The RWA only affect the light coupling term $\hat{V}$ and yields

$$\tilde{V}/V_0 = \alpha^s \mathbb{1} - i\frac{\alpha^v}{8J}(e^{2ikx}\hat{J}_- - e^{-2ikx}\hat{J}_+) + \frac{\alpha^t}{2J(2J-1)}\left(\hat{\boldsymbol{J}}^2 - \frac{3}{2}(\hat{J}_x^2 + \hat{J}_y^2)\right) \tag{6.10}$$

where the characteristic feature of Raman beams is visible : the absorption or emission of a photon is characterized by a change in internal state via the operator $\hat{J}_\pm$ and momentum kick $\pm 2\hbar k$.

Another step is necessary to obtain a form similar to the Landau Hamiltonian. The unitary transform defined by the operator

$$\hat{U} = \exp\left(2ik\hat{x}\hat{J}_z\right) \tag{6.11}$$

makes the spin-orbit coupling visible similarly to equation 6.1 as

$$\hat{U}\frac{\hat{p}_x^2}{2m}\hat{U}^\dagger = \frac{(\hat{p}_x^2 - 2\hbar k\hat{J}_z)^2}{2m}. \tag{6.12}$$

The total Hamiltonian finally reads

$$\hat{H} = \frac{(\hat{p}_x^2 - \hbar K\hat{J}_z)^2}{2m} - \hbar\Omega\left(\hat{J}_x + \frac{\hat{J}_z^2}{2J+3}\right) - \hbar\delta\hat{J}_z \tag{6.13}$$

where

$$K = 2k \quad \text{and} \quad \hbar\Omega = \frac{2J+3}{4(J+1)(2J+1)}V_0 \tag{6.14}$$

according to the exact expressions of the scalar and tensor light-shifts for the $J \to J+1$ transition. An additional position-dependent energy term (with no effect on the internal state) was neglected to obtain equation 6.13. This term can induce an attractive or repulsive potential, whose effect remains negligible on the timescale of the experiment (a few hundred µs).

The analogy with the Landau Hamiltonian can be seen by writing

$$\hat{H} = \frac{(\hat{p}_x^2 - \hbar K \hat{J}_z)^2}{2m} - \hbar\Omega \hat{J}_x + V(\hat{J}_z) \tag{6.15}$$

$$\hat{H}_{\text{Landau}} = \frac{(\hat{p}_x^2 - eB\hat{y})^2}{2m} + \frac{\hat{p}_y^2}{2m} \tag{6.16}$$

with the identifications $\hat{J}_z \leftrightarrow \hat{y}$ and $\hbar K \leftrightarrow eB$. While the Landau Hamiltonian involves two dimensions of space, ours has only one dimension of space and a synthetic dimension played by the internal state. The kinetic energy term $\hat{p}_y^2/2m$ is played by $\hat{J}_x$ which couples neighbouring m states.

The energy scale which separates the free-particle regime where the kinetic energy dominates from the strongly coupled regime is $E_{\text{rec}} = \hbar^2 K^2/(2m)$, the recoil energy associated to an elementary Raman process of photon absorption followed by stimulated emission of a photon. For $\hbar\Omega = E_{\text{rec}}$, the effect of $V(\hat{J}_z)$ is minor and even flattens the energy band plotted on figure 6.2. The strong similarity with the energy structure of the Landau Hamiltonian validates the analogy between the two systems.

For $\Omega = 0$, each parabola of the spectrum corresponds to a given m state and they are not coupled. On the other hand for $\Omega = E_{\text{rec}}$, the m state is coupled to the momentum p in the ground band through a phenomenon of spin-momentum locking. It is due to the fact that spin-hopping occurs together with the acquisition of a momentum kick from a Raman process.

6.1.2 State preparation in the ground band

We prepare states of arbitrary momentum p in the ground band in the following way. A cloud of $8(2)\times10^4$ atoms at 0.55(6) µK is released from the cODT. The initial internal state of an atom is $|-J\rangle$ similarly to the other experiments presented in the manuscript, and it has no velocity in the laboratory frame. It is more convenient to place ourselves in the moving frame associated with the detuning δ between the two Raman beams. Indeed while $\delta = 0$ results in a 'standing wave' (it is *not* a 1D trapping lattice since the polarizations are orthogonal but only a modulation of the light polarization), $\delta \neq 0$ corresponds to the nodes moving at a speed $v_{\text{latt.}} = -\delta/K$. Initially $\delta = 0$ and the light power is increased adiabatically up to $\hbar\Omega = 1.02(6)\, E_{\text{rec}}$, inducing the energy structure plotted on figure 6.2.

We perform a ramp of detuning $\dot{\delta}$ which results in an inertial force $F = -m\dot{v}_{\text{latt.}} = m\dot{\delta}/K$ so that the equation of motion $\dot{p} = F$ yields

$$p(t) = p_0 + \frac{m}{K}\delta(t) \quad \text{with} \quad p_0 = -8\hbar K. \tag{6.17}$$

This allows us to prepare a state of given p by ramping the detuning δ up to a final

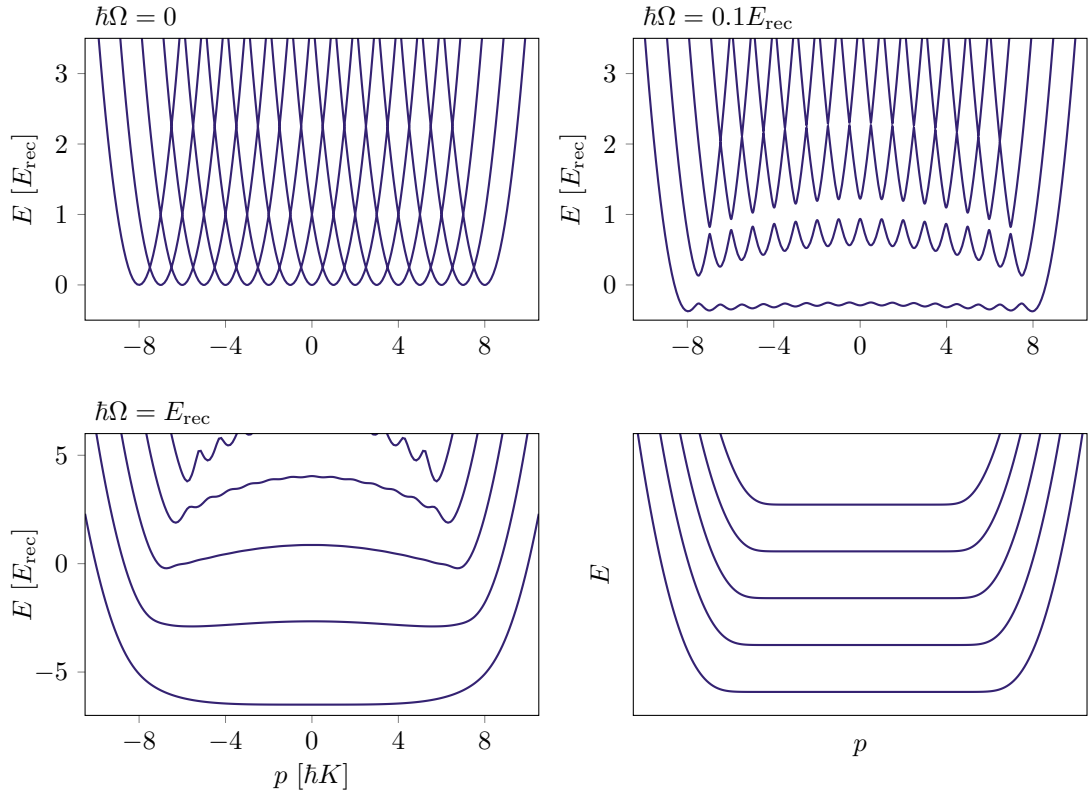

Figure 6.2 – Energy spectrum of the Hamiltonian. The eigen energies calculated numerically for $\hbar\Omega = 0$, $0.1\,E_{\mathrm{rec}}$ and $1\,E_{\mathrm{rec}}$ are plotted as a function of p. In the absence of Raman couplings ($\Omega = 0$), the spectrum corresponds to the kinetic energy of a free particle. The fact that there are $2J + 1 = 17$ parabolas centered on integer multiples of $\hbar K$ from -8 to 8 is artificial since there is no spin-coupling in this case. It starts being relevant as Ω increases, as the coupling progressively opens a gap, leading to a flat ground band for $\hbar\Omega = E_{\mathrm{rec}}$. **(Bottom right)** Energy spectrum of the Landau Hamiltonian in a ribbon geometry : infinite along x (with associated momentum p) and finite along y, to respect the analogy with our finite synthetic dimension. The analogy between the two systems is valid at least for the two lowest bands which are quite flat.

value

$$\delta = 2\left(\frac{p}{\hbar K} + J\right)\frac{E_{\mathrm{rec}}}{\hbar}. \tag{6.18}$$

Both the internal state of an atom and its velocity in the lab frame can be measured by a time-of-flight measurement as shown on figure 6.3.

A magnetic field gradient induces a m-dependent space separation identically to the other projects presented so far, and the velocity in the laboratory frame induces a separation in the orthogonal direction. These two displacements can be imaged simultaneously by absorption imaging and the fact that the imaged clouds are aligned illustrates the phenomenon of spin-momentum locking. This allows us to recover the velocity in the moving frame as a function of p across the ground

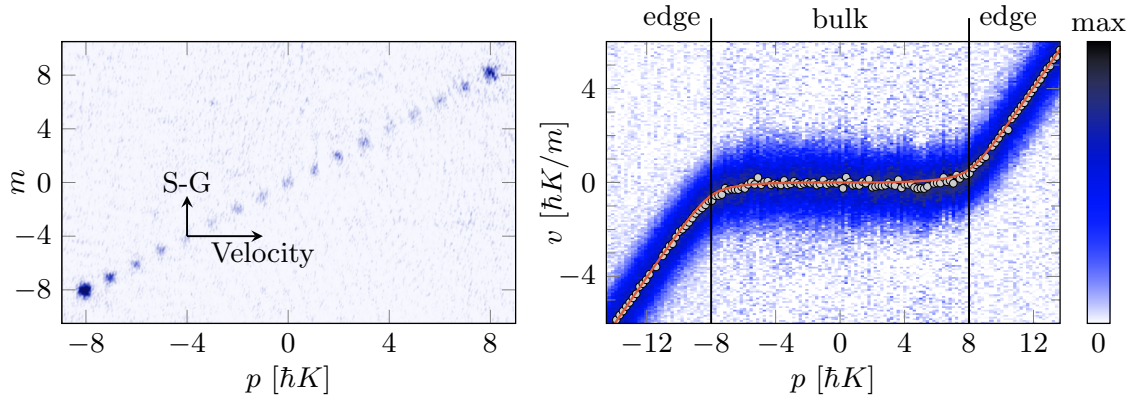

Figure 6.3 – (Left) Detection of both the velocity and internal m state. During a time-of-flight of a few ms, the velocity in the laboratory frame and the Stern-Gerlach magnetic field gradient split the atomic cloud in two orthogonal directions. This image was obtained by superimposing the single shot pictures corresponding to the preparation of all accessible p-states in the ground band. **(Right) Velocity distribution in the moving frame across the ground band**. The region of zero velocity corresponds to the bulk, as opposed to the edges, corresponding to the edges of the synthetic dimension. Grey dots correspond to the average velocity $\langle \hat{v} \rangle$ while the solid red line is the value expected from the derivative of the ground band dispersion $\partial_p E_0$.

band, plotted on figure 6.3.

It shows distinctive behaviours in regions that can be defined as the bulk and two edges. In the bulk the velocity is close to zero, which is consistent with the value expected for a flat band $\langle \hat{v} \rangle = \partial E_0 / \partial p = 0$. The velocity can be defined as the derivative of the operator $\hat{x}$ with respect to time in the Heisenberg picture as

$$\hat{v} = \frac{i}{\hbar}\left[\hat{H}, \hat{x}\right] = \frac{1}{m}\left(\hat{p} - \hbar K \hat{J}_z\right) \tag{6.19}$$

It means that the spin-momentum locking occurs only in the bulk, while on the edges the velocity varies linearly with p, the internal state being either $|-J\rangle$ (for $p < -8\hbar K$) or $|+J\rangle$ (for $p > 8\hbar K$).

6.1.3 Cyclotron orbits and chiral edge states

The state preparation scheme exhibits topological behaviour, as the inertial force in the real dimension induces transport (change of internal state) in the (orthogonal) synthetic dimension. Another topological feature of this system is visible when probing the gap between the ground and the first excited band. The detuning is ramped to prepare a given p-state in the ground band and then abruptly increased by a value of $2E_{\mathrm{rec}}/\hbar$. This quench shifts the value of p by one unit of $\hbar K$ according to equation 6.18. This non-adiabatic transfer induces a superposition of a ground and excited states of identical momentum $p' = p + \hbar K$, leading to oscillations of both velocity and magnetization at frequency $\omega_c = (E_1 - E_0)(p')/\hbar$, proportional to the energy gap at momentum p'. By integrating the measured velocity oscillations

with respect to time, we obtain cyclotron orbits in the bulk and skipping orbits on the edges, a key feature of topological systems. They are plotted on figure 6.4, where the transition from bulk behaviour to edge behaviour is clearly visible. The orbits are closed in the bulk, whereas on the edges the trajectory is ballistic, with two opposite directions corresponding to opposite chirality. They are characterized by skipping orbits, which 'bounce' on the edge of the system (since there is no accessible $m = \pm 9$ state).

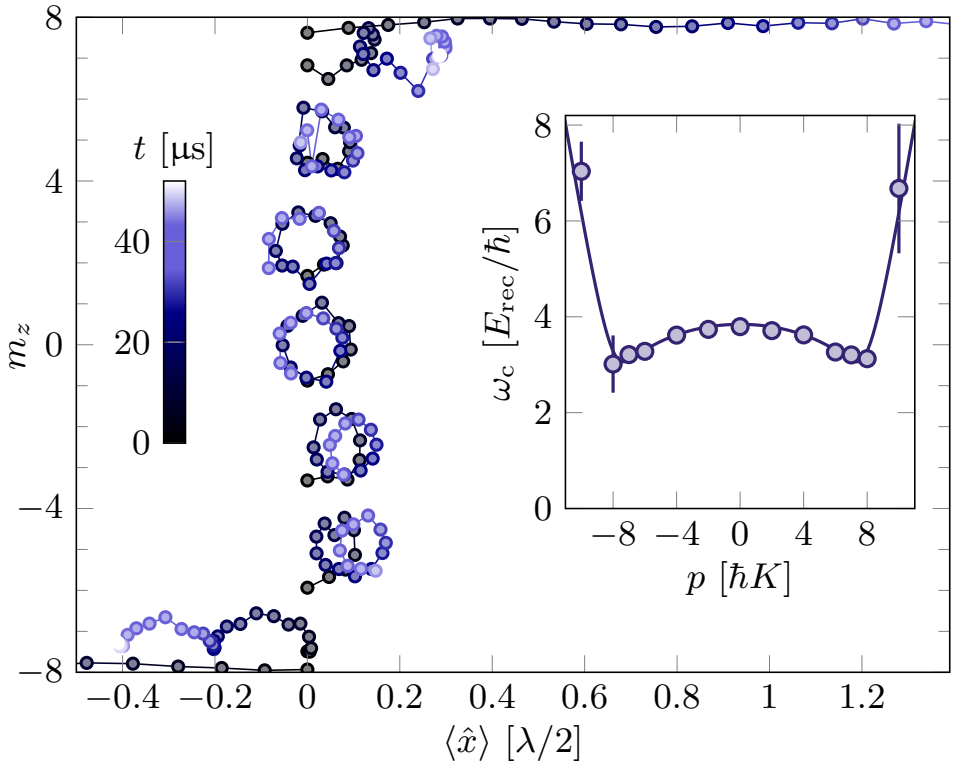

Figure 6.4 – Cyclotron and skipping orbits. Trajectories in the (x, m_z) plane measured after a detuning quench, for different initial m_z. Note that while the m states are discrete, the average magnetization m_z varies in a continuous way. The position $\langle \hat{x} \rangle$ is not measured directly but inferred from integration of the velocity and is initially zero for all trajectories. **(Inset) Cyclotron frequencies** measured for the different orbits. The result is consistent with the fact that the first excited band is not perfectly flat as shown on figure 6.2.

This system already exhibits topological features, yet one may ask what would happen if interactions between atoms were present. So far they have always been neglected as the mean-field interaction energy scale gn remains much smaller than $k_B T$ for thermal gases, where $g = 4\pi\hbar^2 a/m$ and a is the scattering length. The problem with lowering the temperature and going to the BEC regime in this case is that the different m states are all spatially overlapped and only one dimension of space is accessible. It means that there can potentially be contact interactions between all couples of m states, whereas the only scattering length whose value has been measured is $a_{-8,-8} = a_{\mathrm{bg}}$.

In the second project, the system is similar with the additional constraint that the synthetic dimension (i.e. the internal state) is mapped onto a real spatial dimension. Therefore different m states are spatially separated which leaves only a reduced amount of coefficients $a_{m,m'}$ to consider, their values being expected to be positive and of the same order of magnitude as a_{bg}. Going to the BEC regime is necessary to see the effect of the interactions. In particular the nucleation of vortices is usually expected for a BEC in presence of a gauge field.

6.2 Artificial gauge field with two spatial dimensions

The following laser configuration is inspired from a proposal [114] suggesting the use of two laser beams to engineer an artificial gauge field thanks to space-dependent light shifts. It is currently developed and has not been realized on the experiment yet. It consists in sending two counter-propagating beams of identical power on the atoms with a position offset d as represented on figure 6.5. The waist w, identical for the two beams, is comparable with d so that it creates a region where the ground state of the light-shift operator varies monotonically.

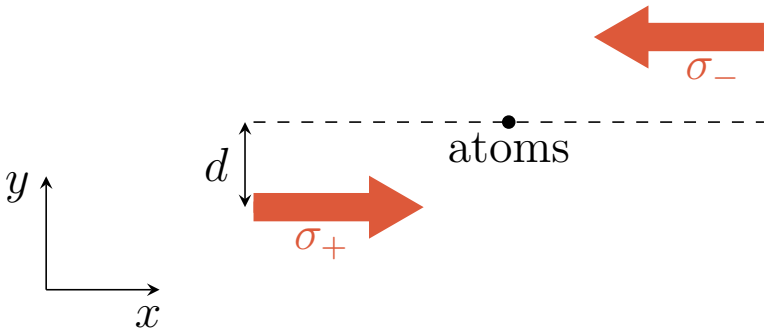

Figure 6.5 – Laser configuration.

The expression of the light shift operator can be computed similarly to the previous project. We neglect the variation of the waist in the axial direction as the Rayleigh length is supposed to be much larger than the length scale of the system. The contributions of the two laser beams are therefore

$$\boldsymbol{E}_1 = E_0 \exp\left(-(y+d)^2/w^2\right) e^{i(kx-\omega_0 t)} \boldsymbol{e}_+$$
$$\boldsymbol{E}_2 = E_0 \exp\left(-(y-d)^2/w^2\right) e^{-i(kx+\omega_0 t)} \boldsymbol{e}_-$$

so that the total electric field is

$$\boldsymbol{E} = \underbrace{2E_0 e^{-(y^2+d^2)/w^2} e^{-i\omega_0 t} \cosh(2yd/w^2)}_{\tilde{E}_0(y)} \underbrace{\left(e^{ikx}\cos\theta(y)\,\boldsymbol{e}_+ + e^{-ikx}\sin\theta(y)\,\boldsymbol{e}_-\right)}_{\boldsymbol{\epsilon}(y)} \quad (6.20)$$

where $\theta(y)$ is a parameter defined as $\tan\theta(y) = \exp(y/y_0)$ with $y_0 = w^2/(4d)$ so that θ varies roughly between 0 and $\pi/2$. The light shift operator is then deduced using equation 1.7. We do not give its full expression as it is not necessary to understand

the main features of this system. The light used here is close to the resonance at 833 nm corresponding to a $J \to J$ transition. This ensures that the state $|-J\rangle_z$ (resp. $|+J\rangle_z$) is not coupled to an excited state via σ_- (resp. σ_+) polarized light. These states are said to be *dark* states, since they cannot absorb light and then spontaneously emit photons (which would make them appear bright).

In fact the local y-dependent ground state is always a dark state and varies continuously from $|J\rangle_z$ for $\theta = 0$ ($y/y_0 \gg 1$, y negative) to $|-J\rangle_z$ for $\theta = \pi/2$ ($y/y_0 \gg 1$, y positive) through the y-dependent mixing of the two opposite circular polarizations as represented on figure 6.6.

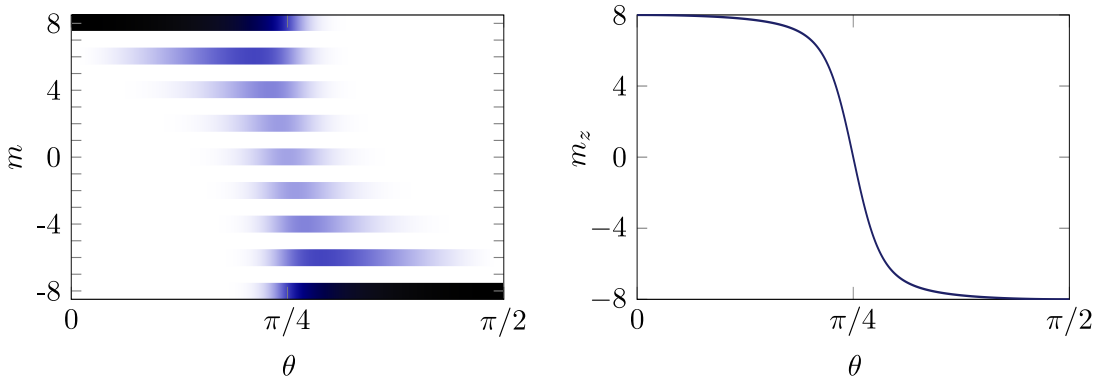

Figure 6.6 – Spin populations of the position-dependent ground state. The populations along z as a function of θ are plotted on the left and the corresponding magnetization on the right. These are the result of numerical simulations.

The situation is therefore similar to the previous project except that now the internal degree of freedom is locked to the position y. This kind of locking behaviour between the internal state and the position is usually associated to the apparition of a quantity called the *Berry connection*. It comes from the fact that the eigenstates of the Hamiltonian depend on the position through the parameter θ. If we describe the adiabatic evolution of a state $|\psi(t)\rangle$ in the basis formed by the eigenstates $|\psi_n\rangle$ (with energy E_n) of the Hamiltonian as

$$|\psi(t)\rangle = \sum_n c_n(t)\,|\psi_n(\theta(t))\rangle\,, \tag{6.21}$$

the Schrödinger equation leads in first order approximation to

$$i\hbar\dot{c}_n(t) = \left(E_n - i\hbar\frac{\partial\theta}{\partial t}\sum_i \langle\psi_n|\partial_i\psi_n\rangle\right)c_n(t). \tag{6.22}$$

The Berry connection $\mathcal{A} = i\hbar\,\langle\psi_n|\nabla\psi_n\rangle$, whose components along the three spatial directions are involved in the previous equation, is a vector potential corresponding to an artificial magnetic field $\mathcal{B} = \nabla \times \mathcal{A}$. In the case of our system, it yields

$$\mathcal{B} = \hbar k\frac{\partial m_z}{\partial y}\boldsymbol{e}_z \tag{6.23}$$

where $m_z = \langle \hat{J}_z \rangle$. It can be cast in a dimensionless way as $\mathcal{B}(y) = (\hbar k/y_0)B(y/y_0)$ where a numerical computation of B in the strong-coupling limit is plotted on figure 6.7. The fact that $\mathcal{B}$ can be written in such a way, independently of the laser power, shows a key feature of dark states. The effects at play are purely geometrical and based on the structure of the $J \to J$ transition. The advantage is that the laser power can be increased without being constrained by the photon scattering rate.

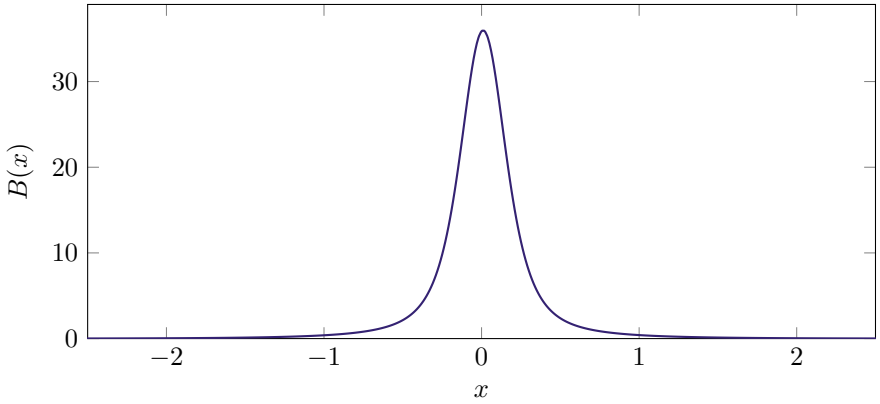

Figure 6.7 – Artificial magnetic field profile.

Preliminary numerical simulations of the Gross-Pitaevskii equation for a Bose-Einstein condensate in presence of this artificial magnetic field are promising and show the apparition of vortices. They were performed with equal scattering length for all m states since we have no information on them. Since the vortex size is proportional to the healing length $\xi = 1/\sqrt{8\pi an}$, which depends on the atomic density n and the scattering length a, it could provide an estimation of the values of the different scattering lengths for even m. Indeed only states with even m are populated in this system as can be seen on figure 6.6.

6.3 Conclusion

In this manuscript we have presented the realization of various types of physical systems using ultracold atoms of dysprosium. The large spin and specific light-shifts in the electronic ground state are especially suited for the realization of spin squeezing and spin-orbit coupling leading to artificial gauge fields. Moreover, the use of $J \to J'$ transitions with $J' = 7$ and 8 will allow us to probe novel interesting systems. Furthermore several tools that are commonly used in the context of ultracold gases such as optical lattices or digital micromirror devices (DMD), able to engineer arbitrary potentials, could in the future enrich the experimental setup. They have not been implemented yet, since dysprosium already exhibits striking features in relatively simple configurations.

The main direction taken by the group is the study of topological many-body systems. They constitute good candidates in the cold atoms field for the realization of sought-after exotic phases of matter. For example a system exhibiting topological superfluidity could be realized by applying spin-orbit coupling to a degenerate gas of fermionic dysprosium. A first step in this direction was realized in the group of

B. Lev [115]. This would require working at very low magnetic field to suppress dipolar relaxation, for which we consider implementing magnetic shielding around the glass cell in the future.

Part IV

Appendices

Appendix A

Full expression of the atomic polarizabilities

We provide the full expression of the scalar, vector and tensor polarizabilities involved in the light shift operator related to a $J \to J'$ transition

$$\hat{V}_{JJ'} = -\frac{|E|^2}{4}\left[\alpha^s_{JJ'}\mathbb{1} - i\alpha^v_{JJ'}\frac{(\boldsymbol{u}^* \times \boldsymbol{u})\cdot\hat{\boldsymbol{J}}}{2J} + \alpha^t_{JJ'}\frac{3[(\boldsymbol{u}^*\cdot\hat{\boldsymbol{J}})(\boldsymbol{u}\cdot\hat{\boldsymbol{J}}) + (\boldsymbol{u}\cdot\hat{\boldsymbol{J}})(\boldsymbol{u}^*\cdot\hat{\boldsymbol{J}})] - 2\hat{\boldsymbol{J}}^2}{2J(2J-1)}\right]. \quad \text{(A.1)}$$

They read

$$\alpha^s_{JJ'} = -\frac{1}{\sqrt{3(2J+1)}}\,\alpha^{(0)}_{JJ'}(\omega) \quad \text{(A.2)}$$

$$\alpha^v_{JJ'} = \sqrt{\frac{2J}{(J+1)(2J+1)}}\,\alpha^{(1)}_{JJ'}(\omega) \quad \text{(A.3)}$$

$$\alpha^t_{JJ'} = \sqrt{\frac{2J(2J-1)}{3(J+1)(2J+1)(2J+3)}}\,\alpha^{(2)}_{JJ'}(\omega) \quad \text{(A.4)}$$

where

$$\alpha^{(k)}_{JJ'}(\omega) = (-1)^{J+J'+k}\sqrt{2k+1}\begin{Bmatrix} 1 & k & 1 \\ J & J' & J \end{Bmatrix}|\langle J'||\boldsymbol{d}||J\rangle|^2 \times \frac{1}{\hbar}\mathrm{Re}\left[\frac{1}{\omega_{J'} - \omega_J - \omega - i\gamma_{JJ'}/2} + \frac{(-1)^k}{\omega_{J'} - \omega_J + \omega + i\gamma_{JJ'}/2}\right]. \quad \text{(A.5)}$$

The curly-brackets term is a Wigner-6j symbol and $\langle J'||\boldsymbol{d}||J\rangle$ is the *reduced matrix element* of the dipole operator introduced in the context of the Wigner-Eckart theorem, used in chapter 5. The fact that the Wigner-6j symbol vanishes for $J = 1/2$ and $k = 2$ explains why there is no tensor light-shift for the ground state of alkali atoms.

Appendix B

Computing the purity from spin populations

We present here the derivation of equation 3.30 used to compute the purity from the measured spin projection probabilities $\Pi_m(\hat{\mathbf{n}})$. According to spin tomography theory, the density matrix of a quantum spin can be reconstructed from integration of the probabilities $\Pi_m(\hat{\mathbf{n}})$ over the Bloch sphere, as [116]

$$\rho = \sum_{m=-J}^{J} \int_{S^2} \frac{\mathrm{d}\hat{\mathbf{n}}}{4\pi} \Pi_m(\hat{\mathbf{n}}) \hat{D}(m, \hat{\mathbf{n}}) \tag{B.1}$$

where S^2 is the unit sphere and the expression for the operator $\hat{D}$ is

$$\hat{D}(m, \hat{\mathbf{n}}) = \frac{2J+1}{\pi} \int_0^{2\pi} \mathrm{d}\gamma \, \sin^2 \frac{\gamma}{2} \, \mathrm{e}^{i\gamma(m - \hat{\mathbf{J}}\cdot\hat{\mathbf{n}})}. \tag{B.2}$$

The purity can then be written as [85]

$$\mathrm{Tr}\left[\rho^2\right] = \sum_{m=-J}^{J} \int_{S^2} \frac{\mathrm{d}\hat{\mathbf{n}}}{4\pi} \Pi_m(\hat{\mathbf{n}}) \, \mathrm{Tr}\left[\rho \, \mathrm{D}(m, \hat{\mathbf{n}})\right] \tag{B.3}$$

$$= (2J+1) \sum_{m=-J}^{J} \int_{S^2} \frac{\mathrm{d}\hat{\mathbf{n}}}{4\pi} \Pi_m(\hat{\mathbf{n}}) \left[\Pi_m(\hat{\mathbf{n}}) - \Pi_{m+1}(\hat{\mathbf{n}})\right], \tag{B.4}$$

with the convention $\Pi_{J+1}(\hat{\mathbf{n}}) = 0$.

Appendix C

Expression of the Wigner function in terms of spin populations

From equation 4.15, we derive the expression given in equation 4.19. We decompose a state $|\psi\rangle$ as $\sum_m c_m |m\rangle_z$. It is sufficient to prove the result for the particular case $\theta = 0$, $\phi = 0$, since it is always possible to perform a basis change to be in this situation.

The density matrix is

$$\rho = \sum_{m_1,\, m_2} c^*_{m_1} c_{m_2} |m_2\rangle \langle m_1| \tag{C.1}$$

so that the coefficients of its decomposition in the multipole basis are

$$\rho_{kq} = \mathrm{Tr}[\rho \hat{T}^\dagger_{k,q}] \tag{C.2}$$

$$= \sum_{m_1,\, m_2} c^*_{m_1} c_{m_2} (-1)^{J-m_2} \sqrt{2k+1} \begin{pmatrix} J & k & J \\ -m_2 & q & m_1 \end{pmatrix}. \tag{C.3}$$

Then we have

$$Y^q_k(0,0) = \sqrt{\frac{2k+1}{4\pi}}\, \delta_{q,\,0} \tag{C.4}$$

so that

$$W(0,0) = \sum_{k=0}^{2J} \sum_{q=-k}^{k} \rho_{kq} Y^q_k(0,0) \tag{C.5}$$

$$= \sum_{k=0}^{2J} \rho_{k0} \sqrt{\frac{2k+1}{4\pi}} \tag{C.6}$$

$$= \sum_{k=0}^{2J} \sum_{m_1,\, m_2} c^*_{m_1} c_{m_2} (-1)^{J-m_2} \frac{2k+1}{\sqrt{4\pi}} \begin{pmatrix} J & k & J \\ -m_2 & 0 & m_1 \end{pmatrix}. \tag{C.7}$$

Finally the selection rule of the Wigner-3j symbols states that it is zero unless $m_1 = m_2$, so that

$$W(0,0) = \sum_m |c_m|^2 (-1)^{J-m} \sum_{k=0}^{2J} \frac{2k+1}{\sqrt{4\pi}} \begin{pmatrix} J & k & J \\ -m & 0 & m \end{pmatrix} \tag{C.8}$$

Note that if we had labeled as $''z''$ the direction (θ, ϕ) and chosen this direction as the quantization axis for the basis to decompose $|\psi\rangle$ in, the previous derivation would have been identical. We can then write

$$W(\theta,\phi) = \sum_m \Pi_m(\theta,\phi)(-1)^{J-m} \sum_{k=0}^{2J} \frac{2k+1}{\sqrt{4\pi}} \begin{pmatrix} J & J & k \\ m & -m & 0 \end{pmatrix} \tag{C.9}$$

$$= \sum_m (-1)^{J-m} a_m \Pi_m(\theta,\phi) \tag{C.10}$$

where we also applied an even permutation leaving the Wigner-3j symbol invariant.

Bibliography

[1]M. Born and P. Jordan, "Zur Quantenmechanik", Z. Physik **34**, 858–888 (1925) (cited on page 2).

[2]M. Planck, "Uber das gesetz der energieverteilung im normalspectrum", (1901) (cited on page 2).

[3]J. P. Gordon, H. J. Zeiger, and C. H. Townes, "The maser—new type of microwave amplifier, frequency standard, and spectrometer", Phys. Rev. **99**, 1264–1274 (1955) (cited on page 2).

[4]M. H. Anderson, J. R. Ensher, M. R. Matthews, C. E. Wieman, and E. A. Cornell, "Observation of bose-einstein condensation in a dilute atomic vapor", Science **269**, 198–201 (1995) (cited on page 2).

[5]K. B. Davis, M. .-O. Mewes, M. R. Andrews, N. J. van Druten, D. S. Durfee, D. M. Kurn, and W. Ketterle, "Bose-einstein condensation in a gas of sodium atoms", Phys. Rev. Lett. **75**, 3969–3973 (1995) (cited on page 2).

[6]T. Bothwell, D. Kedar, E. Oelker, J. M. Robinson, S. L. Bromley, W. L. Tew, J. Ye, and C. J. Kennedy, "JILA SrI optical lattice clock with uncertainty of 2.0 x10ˆ{-18}", Metrologia **56**, 065004 (2019) (cited on page 2).

[7]R. P. Feynman, "Simulating physics with computers", (1982) (cited on page 2).

[8]I. Bloch, J. Dalibard, and S. Nascimbène, "Quantum simulations with ultracold quantum gases", Nature Phys **8**, 267–276 (2012) (cited on page 2).

[9]T. Bourdel, L. Khaykovich, J. Cubizolles, J. Zhang, F. Chevy, M. Teichmann, L. Tarruell, S. J. J. M. F. Kokkelmans, and C. Salomon, "Experimental study of the BEC-BCS crossover region in lithium 6", Phys. Rev. Lett. **93**, 050401 (2004) (cited on page 2).

[10]G. B. Partridge, K. E. Strecker, R. I. Kamar, M. W. Jack, and R. G. Hulet, "Molecular probe of pairing in the BEC-BCS crossover", Phys. Rev. Lett. **95**, Publisher: American Physical Society, 020404 (2005) (cited on page 2).

[11]I. Affleck and J. B. Marston, "Large-n limit of the heisenberg-hubbard model: implications for high-tc superconductors", Phys. Rev. B **37**, 3774–3777 (1988) (cited on page 2).

[12]A. Mazurenko, C. S. Chiu, G. Ji, M. F. Parsons, M. Kanász-Nagy, R. Schmidt, F. Grusdt, E. Demler, D. Greif, and M. Greiner, "A cold-atom fermi–hubbard antiferromagnet", Nature **545**, 462–466 (2017) (cited on page 2).

[13]F. Gerbier and J. Dalibard, "Gauge fields for ultracold atoms in optical superlattices", New J. Phys. **12**, 033007 (2010) (cited on page 2).

[14]N. Goldman, J. C. Budich, and P. Zoller, "Topological quantum matter with ultracold gases in optical lattices", Nature Phys **12**, 639–645 (2016) (cited on page 3).

[15]A. J. Berglund, J. L. Hanssen, and J. J. McClelland, "Narrow-line magneto-optical cooling and trapping of strongly magnetic atoms", Phys. Rev. Lett. **100**, 113002 (2008) (cited on page 3).

[16]S. H. Youn, M. Lu, U. Ray, and B. L. Lev, "Dysprosium magneto-optical traps", Phys. Rev. A **82**, 043425 (2010) (cited on page 3).

[17]T. Maier, H. Kadau, M. Schmitt, A. Griesmaier, and T. Pfau, "Narrow-line magneto-optical trap for dysprosium atoms", Opt. Lett. **39**, 3138 (2014) (cited on pages 3, 7).

[18]E. Lucioni, G. Masella, A. Fregosi, C. Gabbanini, S. Gozzini, A. Fioretti, L. Del Bino, J. Catani, G. Modugno, and M. Inguscio, "A new setup for experiments with ultracold dysprosium atoms", Eur. Phys. J. Spec. Top. **226**, 2775–2780 (2017) (cited on page 3).

[19]C. Ravensbergen, V. Corre, E. Soave, M. Kreyer, E. Kirilov, and R. Grimm, "Production of a degenerate fermi-fermi mixture of dysprosium and potassium atoms", Physical Review A, 12 (2018) (cited on pages 3, 31).

[20]A. Trautmann, P. Ilzhöfer, G. Durastante, C. Politi, M. Sohmen, M. J. Mark, and F. Ferlaino, "Dipolar quantum mixtures of erbium and dysprosium atoms", Physical Review Letters, 6 (2018) (cited on page 3).

[21]D. Dreon, L. A. Sidorenkov, C. Bouazza, W. Maineult, J. Dalibard, and S. Nascimbene, "Optical cooling and trapping of highly magnetic atoms: the benefits of a spontaneous spin polarization", J. Phys. B: At. Mol. Opt. Phys. **50**, 065005 (2017) (cited on pages 3, 14).

[22]Y. Tang, W. Kao, K.-Y. Li, and B. L. Lev, "Tuning the dipole-dipole interaction in a quantum gas with a rotating magnetic field", Phys. Rev. Lett. **120**, 230401 (2018) (cited on page 3).

[23]H. Kadau, M. Schmitt, M. Wenzel, C. Wink, T. Maier, I. Ferrier-Barbut, and T. Pfau, "Observing the rosensweig instability of a quantum ferrofluid", Nature **530**, 194–197 (2016) (cited on page 3).

[24]C. R. Cabrera, L. Tanzi, J. Sanz, B. Naylor, P. Thomas, P. Cheiney, and L. Tarruell, "Quantum liquid droplets in a mixture of bose-einstein condensates", Science **359**, 301–304 (2018) (cited on page 3).

[25]L. Chomaz, R. M. W. van Bijnen, D. Petter, G. Faraoni, S. Baier, J. H. Becher, M. J. Mark, F. Wächtler, L. Santos, and F. Ferlaino, "Observation of roton mode population in a dipolar quantum gas", Nature Phys **14**, 442–446 (2018) (cited on page 3).

[26]L. Chomaz, D. Petter, P. Ilzhöfer, G. Natale, A. Trautmann, C. Politi, G. Durastante, R. M. W. van Bijnen, A. Patscheider, M. Sohmen, M. J. Mark, and F. Ferlaino, "Long-lived and transient supersolid behaviors in dipolar quantum gases", Phys. Rev. X **9**, 021012 (2019) (cited on page 3).

[27]F. Böttcher, J.-N. Schmidt, M. Wenzel, J. Hertkorn, M. Guo, T. Langen, and T. Pfau, "Transient supersolid properties in an array of dipolar quantum droplets", Phys. Rev. X **9**, 011051 (2019) (cited on page 3).

[28]L. Tanzi, E. Lucioni, F. Famà, J. Catani, A. Fioretti, C. Gabbanini, R. N. Bisset, L. Santos, and G. Modugno, "Observation of a dipolar quantum gas with metastable supersolid properties", Phys. Rev. Lett. **122**, 130405 (2019) (cited on page 3).

[29]D. Drung, C. Assmann, J. Beyer, A. Kirste, M. Peters, F. Ruede, and T. Schurig, "Highly sensitive and easy-to-use SQUID sensors", IEEE Trans. Appl. Supercond. **17**, 699–704 (2007) (cited on page 3).

[30]I. K. Kominis, T. W. Kornack, J. C. Allred, and M. V. Romalis, "A subfemtotesla multichannel atomic magnetometer", Nature **422**, 596–599 (2003) (cited on page 3).

[31]T. Chalopin, C. Bouazza, A. Evrard, V. Makhalov, D. Dreon, J. Dalibard, L. A. Sidorenkov, and S. Nascimbene, "Quantum-enhanced sensing using non-classical spin states of a highly magnetic atom", Nat Commun **9**, 1–8 (2018) (cited on pages 7, 37, 60).

[32]Y. Tang, N. Q. Burdick, K. Baumann, and B. L. Lev, "Bose-einstein condensation of 162dy and 160dy", New J. Phys. **17**, 045006 (2015) (cited on page 7).

[33]F. Böttcher, M. Wenzel, J.-N. Schmidt, M. Guo, T. Langen, I. Ferrier-Barbut, T. Pfau, R. Bombín, J. Sánchez-Baena, J. Boronat, and F. Mazzanti, "Dilute dipolar quantum droplets beyond the extended gross-pitaevskii equation", Phys. Rev. Research **1**, Publisher: American Physical Society, 033088 (2019) (cited on page 7).

[34]I. Ferrier-Barbut, M. Wenzel, F. Böttcher, T. Langen, M. Isoard, S. Stringari, and T. Pfau, "Scissors mode of dipolar quantum droplets of dysprosium atoms", Phys. Rev. Lett. **120**, 160402 (2018) (cited on page 7).

[35]J. Stuhler, A. Griesmaier, T. Koch, M. Fattori, T. Pfau, S. Giovanazzi, P. Pedri, and L. Santos, "Observation of dipole-dipole interaction in a degenerate quantum gas", Phys. Rev. Lett. **95**, 150406 (2005) (cited on page 8).

[36]G. A. Smith, S. Chaudhury, A. Silberfarb, I. H. Deutsch, and P. S. Jessen, "Continuous weak measurement and nonlinear dynamics in a cold spin ensemble", Phys. Rev. Lett. **93**, 163602 (2004) (cited on page 9).

[37]M. Kitagawa and M. Ueda, "Squeezed spin states", Phys. Rev. A **47**, 5138–5143 (1993) (cited on pages 9, 44, 65).

[38]D. Dreon, "Designing and building an ultracold dysprosium experiment : a new framework for light-spin interaction", PhD thesis (PSL Research University, July 12, 2017) (cited on pages 9, 11).

[39]F. L. Kien, P. Schneeweiss, and A. Rauschenbeutel, "Dynamical polarizability of atoms in arbitrary light fields: general theory and application to cesium", Eur. Phys. J. D **67**, 92 (2013) (cited on page 9).

[40]A. Kramida, Y. Ralchenko, and J. Reader, "Nist atomic spectra database (ver. 5.2)", National Institute of Standards and Technology, Gaithersburg, MD, 10.18434/T4W30F (2013) (cited on page 10).

[41]H. Li, J.-F. Wyart, O. Dulieu, S. Nascimbène, and M. Lepers, "Optical trapping of ultracold dysprosium atoms: transition probabilities, dynamic dipole polarizabilities and van der waals c6 coefficients", J. Phys. B: At. Mol. Opt. Phys. **50**, 014005 (2017) (cited on page 10).

[42]T. Chalopin, "Quantum-enhanced sensing and synthetic landau levels with ultracold dysprosium atoms", PhD thesis (Sorbonne Université, Dec. 12, 2019) (cited on pages 11, 89).

[43]M. Greiner, I. Bloch, T. W. Hänsch, and T. Esslinger, "Magnetic transport of trapped cold atoms over a large distance", Phys. Rev. A **63**, 031401 (2001) (cited on page 15).

[44]J. Léonard, M. Lee, A. Morales, T. M. Karg, T. Esslinger, and T. Donner, "Optical transport and manipulation of an ultracold atomic cloud using focus-tunable lenses", New J. Phys. **16**, 093028 (2014) (cited on page 15).

[45]C. Bouazza, "Ultracold dysprosium gas in optical dipole traps : control of interactions between highly magnetic atoms", PhD thesis (PSL Research University, May 4, 2018) (cited on page 15).

[46]K. Helmerson, A. Martin, and D. E. Pritchard, "Laser cooling of magnetically trapped neutral atoms", J. Opt. Soc. Am. B **9**, 1988 (1992) (cited on page 16).

[47]T. Ido, Y. Isoya, and H. Katori, "Optical-dipole trapping of sr atoms at a high phase-space density", Phys. Rev. A **61**, 061403 (2000) (cited on page 16).

[48]T. Walker, D. Sesko, and C. Wieman, "Collective behavior of optically trapped neutral atoms", Physical Review Letters **64**, 5 (1990) (cited on page 17).

[49]M. Chalony, A. Kastberg, B. Klappauf, and D. Wilkowski, "Doppler cooling to the quantum limit", Phys. Rev. Lett. **107**, 243002 (2011) (cited on page 17).

[50]T. Chalopin, V. Makhalov, C. Bouazza, A. Evrard, A. Barker, M. Lepers, J.-F. Wyart, O. Dulieu, J. Dalibard, R. Lopes, and S. Nascimbene, "Anisotropic light-shift and magic-polarization of the intercombination line of dysprosium atoms in a far-detuned dipole trap", Phys. Rev. A **98**, 040502 (2018) (cited on page 17).

[51]H. Wu, E. Arimondo, and C. J. Foot, "Dynamics of evaporative cooling for bose-einstein condensation", Phys. Rev. A **56**, 560–569 (1997) (cited on page 19).

[52]Y. Shin, M. Saba, T. A. Pasquini, W. Ketterle, D. E. Pritchard, and A. E. Leanhardt, "Atom interferometry with bose-einstein condensates in a double-well potential", Phys. Rev. Lett. **92**, 050405 (2004) (cited on page 23).

[53]S. Baier, *An optical dipole trap for erbium with tunable geometry, master's thesis, university of innsbruck* (2012) (cited on page 23).

[54]J. Walraven, "Atomic hydrogen: the quantum gas", Phys. World **8**, 37–42 (1995) (cited on page 23).

[55]S. Stellmer, B. Pasquiou, R. Grimm, and F. Schreck, "Laser cooling to quantum degeneracy", Phys. Rev. Lett. **110**, Publisher: American Physical Society, 263003 (2013) (cited on page 23).

[56]M. D. Barrett, J. A. Sauer, and M. S. Chapman, "All-optical formation of an atomic bose-einstein condensate", Phys. Rev. Lett. **87**, 010404 (2001) (cited on page 23).

[57]R. Grimm, M. Weidemüller, and Y. B. Ovchinnikov, "Optical dipole traps for neutral atoms", in *Advances in atomic, molecular, and optical physics*, Vol. 42 (Elsevier, 2000), pp. 95–170 (cited on page 23).

[58]R. Onofrio, D. S. Durfee, C. Raman, M. Köhl, C. E. Kuklewicz, and W. Ketterle, "Surface excitations of a bose-einstein condensate", Phys. Rev. Lett. **84**, 810–813 (2000) (cited on page 25).

[59]T. Lahaye, C. Menotti, L. Santos, M. Lewenstein, and T. Pfau, "The physics of dipolar bosonic quantum gases", Rep. Prog. Phys. **72**, 126401 (2009) (cited on page 31).

[60]E. A. Donley, N. R. Claussen, S. L. Cornish, J. L. Roberts, E. A. Cornell, and C. E. Wieman, "Dynamics of collapsing and exploding bose–einstein condensates", Nature **412**, 295–299 (2001) (cited on page 31).

[61]C. Eberlein, S. Giovanazzi, and D. H. J. O'Dell, "Exact solution of the thomas-fermi equation for a trapped bose-einstein condensate with dipole-dipole interactions", Phys. Rev. A **71**, 033618 (2005) (cited on page 31).

[62]S. Hensler, J. Werner, A. Griesmaier, P. Schmidt, A. Görlitz, T. Pfau, S. Giovanazzi, and K. Rzażewski, "Dipolar relaxation in an ultra-cold gas of magnetically trapped chromium atoms", Appl. Phys. B **77**, 765–772 (2003) (cited on page 33).

[63]C. Cohen-Tannoudji, "Atomes ultrafroids - piègeage non dissipatif et refroidissement évaporatif, cinquième cours", Nov. 12, 1996 (cited on page 33).

[64]J. Dalibard, "Atomes ultra-froids, notes de cours" (cited on page 34).

[65]K. M. O'Hara, M. E. Gehm, S. R. Granade, and J. E. Thomas, "Scaling laws for evaporative cooling in time-dependent optical traps", Phys. Rev. A **64**, 051403 (2001) (cited on page 34).

[66]S. Chaudhury, S. Merkel, T. Herr, A. Silberfarb, I. H. Deutsch, and P. S. Jessen, "Quantum control of the hyperfine spin of a cs atom ensemble", Phys. Rev. Lett. **99**, 163002 (2007) (cited on pages 37, 47).

[67]R. E. Slusher, L. W. Hollberg, B. Yurke, J. C. Mertz, and J. F. Valley, "Observation of squeezed states generated by four-wave mixing in an optical cavity", Phys. Rev. Lett. **55**, 2409–2412 (1985) (cited on page 37).

[68]J. Aasi, "Enhancing the sensitivity of the LIGO gravitational wave detector by using squeezed states of light", Nature Photon **7**, 613–619 (2013) (cited on page 37).

[69]M. H. Schleier-Smith, I. D. Leroux, and V. Vuletić, "Squeezing the collective spin of a dilute atomic ensemble by cavity feedback", Phys. Rev. A **81**, 021804 (2010) (cited on pages 37, 46, 69).

[70]M. F. Riedel, P. Böhi, Y. Li, T. W. Hänsch, A. Sinatra, and P. Treutlein, "Atom-chip-based generation of entanglement for quantum metrology", Nature **464**, 1170–1173 (2010) (cited on page 37).

[71]V. Meyer, M. A. Rowe, D. Kielpinski, C. A. Sackett, W. M. Itano, C. Monroe, and D. J. Wineland, "Experimental demonstration of entanglement-enhanced rotation angle estimation using trapped ions", Phys. Rev. Lett. **86**, 5870–5873 (2001) (cited on page 37).

[72]A. Omran, H. Levine, A. Keesling, G. Semeghini, T. T. Wang, S. Ebadi, H. Bernien, A. S. Zibrov, H. Pichler, S. Choi, J. Cui, M. Rossignolo, P. Rembold, S. Montangero, T. Calarco, M. Endres, M. Greiner, V. Vuletić, and M. D. Lukin, "Generation and manipulation of schrödinger cat states in rydberg atom arrays", Science **365**, 570–574 (2019) (cited on page 38).

[73]M. D. Frye, S. L. Cornish, and J. M. Hutson, "Prospects of forming high-spin polar molecules from ultracold atoms", arXiv:1910.09641 (2020) (cited on pages 38, 72).

[74]F. T. Arecchi, E. Courtens, R. Gilmore, and H. Thomas, "Atomic coherent states in quantum optics", Phys. Rev. A **6**, 2211–2237 (1972) (cited on page 39).

[75]J. P. Dowling, G. S. Agarwal, and W. P. Schleich, "Wigner distribution of a general angular-momentum state: applications to a collection of two-level atoms", Phys. Rev. A **49**, 4101–4109 (1994) (cited on pages 40, 66).

[76]B. Yurke, S. L. McCall, and J. R. Klauder, "SU(2) and SU(1,1) interferometers", Phys. Rev. A **33**, 4033–4054 (1986) (cited on page 42).

[77]D. M. Greenberger, M. A. Horne, A. Shimony, and A. Zeilinger, "Bell's theorem without inequalities", American Journal of Physics **58**, 1131–1143 (1990) (cited on page 45).

[78]B. C. Sanders, "Quantum dynamics of the nonlinear rotator and the effects of continual spin measurement", Phys. Rev. A **40**, 2417–2427 (1989) (cited on page 45).

[79]D. J. Wineland, J. J. Bollinger, W. M. Itano, F. L. Moore, and D. J. Heinzen, "Spin squeezing and reduced quantum noise in spectroscopy", Phys. Rev. A **46**, R6797–R6800 (1992) (cited on page 45).

[80]M. Takeuchi, S. Ichihara, T. Takano, M. Kumakura, T. Yabuzaki, and Y. Takahashi, "Spin squeezing via one-axis twisting with coherent light", Phys. Rev. Lett. **94**, 023003 (2005) (cited on page 46).

[81]E. Davis, G. Bentsen, and M. Schleier-Smith, "Approaching the heisenberg limit without single-particle detection", Phys. Rev. Lett. **116**, 053601 (2016) (cited on page 46).

[82]H. Strobel, W. Muessel, D. Linnemann, T. Zibold, D. B. Hume, L. Pezzè, A. Smerzi, and M. K. Oberthaler, "Fisher information and entanglement of non-gaussian spin states", Science **345**, 424–427 (2014) (cited on pages 46, 63).

[83]J. J. . Bollinger, W. M. Itano, D. J. Wineland, and D. J. Heinzen, "Optimal frequency measurements with maximally correlated states", Phys. Rev. A **54**, R4649–R4652 (1996) (cited on pages 47, 60).

[84]A. Evrard, V. Makhalov, T. Chalopin, L. A. Sidorenkov, J. Dalibard, R. Lopes, and S. Nascimbene, "Enhanced magnetic sensitivity with non-gaussian quantum fluctuations", Phys. Rev. Lett. **122**, 173601 (2019) (cited on page 52).

[85]S. N. Filippov and V. I. Man'ko, "Purity of spin states in terms of tomograms", J Russ Laser Res **34**, 14–21 (2013) (cited on pages 54, 102).

[86]S. P. Nolan, S. S. Szigeti, and S. A. Haine, "Optimal and robust quantum metrology using interaction-based readouts", Phys. Rev. Lett. **119**, 193601 (2017) (cited on pages 58, 63, 65).

[87]L. Pezze' and A. Smerzi, "Entanglement, non-linear dynamics, and the heisenberg limit", Phys. Rev. Lett. **102**, 100401 (2009) (cited on page 59).

[88]M. Gessner, A. Smerzi, and L. Pezzè, "Metrological nonlinear squeezing parameter", Phys. Rev. Lett. **122**, 090503 (2019) (cited on pages 59, 63).

[89]V. Giovannetti, S. Lloyd, and L. Maccone, "Quantum metrology", Phys. Rev. Lett. **96**, 010401 (2006) (cited on page 60).

[90]W. K. Wootters, "Statistical distance and hilbert space", Phys. Rev. D **23**, 357–362 (1981) (cited on page 63).

[91]S. L. Braunstein and C. M. Caves, "Statistical distance and the geometry of quantum states", Phys. Rev. Lett. **72**, 3439–3443 (1994) (cited on page 63).

[92]A. Kenfack and K. Zyczkowski, "Negativity of the wigner function as an indicator of nonclassicality", J. Opt. B: Quantum Semiclass. Opt. **6**, 396–404 (2004) (cited on page 66).

[93]G. S. Agarwal, "Relation between atomic coherent-state representation, state multipoles, and generalized phase-space distributions", Phys. Rev. A **24**, 2889–2896 (1981) (cited on page 67).

[94]E. Majorana, "Atomi orientati in campo magnetico variabile", Nuovo Cim **9**, 43–50 (1932) (cited on page 70).

[95]T. Monz, P. Schindler, J. T. Barreiro, M. Chwalla, D. Nigg, W. A. Coish, M. Harlander, W. Hänsel, M. Hennrich, and R. Blatt, "14-qubit entanglement: creation and coherence", Phys. Rev. Lett. **106**, 130506 (2011) (cited on page 71).

[96]V. Makhalov, T. Satoor, A. Evrard, T. Chalopin, R. Lopes, and S. Nascimbene, "Probing quantum criticality and symmetry breaking at the microscopic level", Phys. Rev. Lett. **123**, 120601 (2019) (cited on page 72).

[97]D. Ulam-Orgikh and M. Kitagawa, "Spin squeezing and decoherence limit in ramsey spectroscopy", Phys. Rev. A **64**, 052106 (2001) (cited on page 73).

[98]S. Sachdev, *Quantum phase transitions*, 2nd ed. (Cambridge University Press, Cambridge, 2011) (cited on page 73).

[99]N. Killoran, M. Cramer, and M. B. Plenio, "Extracting entanglement from identical particles", Phys. Rev. Lett. **112**, 150501 (2014) (cited on page 74).

[100]J. Vidal, "Concurrence in collective models", Phys. Rev. A **73**, 062318 (2006) (cited on pages 74, 88).

[101]M. A. Rowe, D. Kielpinski, V. Meyer, C. A. Sackett, W. M. Itano, C. Monroe, and D. J. Wineland, "Experimental violation of a bell's inequality with efficient detection", Nature **409**, Number: 6822 Publisher: Nature Publishing Group, 791–794 (2001) (cited on page 78).

[102]C. H. Bennett, H. J. Bernstein, S. Popescu, and B. Schumacher, "Concentrating partial entanglement by local operations", Phys. Rev. A **53**, 2046–2052 (1996) (cited on page 79).

[103]S. Hill and W. K. Wootters, "Entanglement of a pair of quantum bits", Phys. Rev. Lett. **78**, 5022–5025 (1997) (cited on page 79).

[104]M. Kozuma, L. Deng, E. W. Hagley, J. Wen, R. Lutwak, K. Helmerson, S. L. Rolston, and W. D. Phillips, "Coherent splitting of bose-einstein condensed atoms with optically induced bragg diffraction", Phys. Rev. Lett. **82**, 871–875 (1999) (cited on page 86).

[105]M. Koashi, V. Buzek, and N. Imoto, "Entangled webs: tight bound for symmetric sharing of entanglement", Phys. Rev. A **62**, 050302 (2000) (cited on page 87).

[106]W. Dür, G. Vidal, and J. I. Cirac, "Three qubits can be entangled in two inequivalent ways", Phys. Rev. A **62**, 062314 (2000) (cited on page 88).

[107]X. Wang and B. C. Sanders, "Spin squeezing and pairwise entanglement for symmetric multiqubit states", Phys. Rev. A **68**, 012101 (2003) (cited on page 88).

[108]X. Wang and K. Molmer, "Pairwise entanglement in symmetric multi-qubit systems", The European Physical Journal D - Atomic, Molecular and Optical Physics **18**, 385–391 (2002) (cited on page 88).

[109]M. Mancini, G. Pagano, G. Cappellini, L. Livi, M. Rider, J. Catani, C. Sias, P. Zoller, M. Inguscio, M. Dalmonte, and L. Fallani, "Observation of chiral edge states with neutral fermions in synthetic hall ribbons", Science **349**, 1510–1513 (2015) (cited on page 89).

[110]B. K. Stuhl, H. I. Lu, L. M. Aycock, D. Genkina, and I. B. Spielman, "Visualizing edge states with an atomic bose gas in the quantum hall regime", Science **349**, 1514–1518 (2015) (cited on page 89).

[111]T. Chalopin, T. Satoor, A. Evrard, V. Makhalov, J. Dalibard, R. Lopes, and S. Nascimbene, "Probing chiral edge dynamics and bulk topology of a synthetic hall system", Nature Phys, 10.1038/s41567-020-0942-5 (2020) (cited on page 89).

[112]Y.-J. Lin, K. Jiménez-García, and I. B. Spielman, "Spin–orbit-coupled bose–einstein condensates", Nature **471**, 83–86 (2011) (cited on page 90).

[113]X. Cui, B. Lian, T.-L. Ho, B. L. Lev, and H. Zhai, "Synthetic gauge field with highly magnetic lanthanide atoms", Phys. Rev. A **88**, 011601 (2013) (cited on page 90).

[114]N. Goldman, G. Juzeliunas, P. Ohberg, and I. B. Spielman, "Light-induced gauge fields for ultracold atoms", Rep. Prog. Phys. **77**, 126401 (2014) (cited on page 96).

[115]N. Q. Burdick, Y. Tang, and B. L. Lev, "Long-lived spin-orbit-coupled degenerate dipolar fermi gas", Phys. Rev. X **6**, Publisher: American Physical Society, 031022 (2016) (cited on page 99).

[116]G. M. D'Ariano, L. Maccone, and M. Paini, "Spin tomography", J. Opt. B: Quantum Semiclass. Opt. **5**, 77–84 (2003) (cited on page 102).

RÉSUMÉ

Ce manuscrit de thèse est consacré à des expériences réalisées à partir de gaz d'atomes de dysprosium ultrafroids. Cet élément possède des propriétés particulières comme un grand moment angulaire J=8 ou bien un déplacement lumineux tensoriel significatif à proximité de résonance. Le dispositif expérimental est présenté dans son ensemble, du piégeage magnéto-optique au refroidissement par évaporation. La modulation spatiale permettant de contrôler la forme d'un piège optique est détaillée, ainsi que le rôle du déplacement lumineux tensoriel dans l'étape de refroidissement Doppler dans un piège optique.

La seconde partie est dédiée à l'utilisation du déplacement lumineux tensoriel dans la préparation d'états comprimés et 'surcomprimés' ainsi que des états chats de Schrödinger. La sensibilité magnétique de ces états est mesurée à l'aide de séquences de Ramsey et permet de calculer le gain métrologique. La fonction de Husimi est reconstruite expérimentalement à partir de mesures de population dans différentes directions, ce qui permet aussi de déterminer la pureté des différents états préparés.

Les états comprimés ont une sensibilité accrue, mais les états surcomprimés montrent une forte diminution du contraste des oscillations de Ramsey. L'utilisation de la distance de Hellinger permet de quantifier la différence entre deux états proches et ainsi donner une nouvelle définition du gain métrologique. La limite de Cramér-Rao est alors atteinte et la sensibilité des états surcomprimés est supérieure à celle des états comprimés. Enfin un système de 16 spins 1/2 indistinguables en interaction est réalisé. Dans une troisième partie nous présentons la mesure de l'intrication de paire pour les états d'un spin J à l'aide de probabilités d'absorption de photons, qui n'a pas été réalisée expérimentalement.

En conclusion sont présentés deux projets où des degrés de libertés externes sont ajoutés à la dynamique des degrés de liberté internes. Dans le premier cas il s'agit d'un système analogue à l'Hamiltonien de Landau pour une particule chargée dans un champ magnétique, avec une dimension d'espace et une dimension synthétique. Dans le second cas, deux dimensions d'espace sont utilisées et la présence d'un déplacement lumineux dépendant de la position réalise un champ magnétique artificiel.

MOTS CLÉS

Dysprosium, états comprimés de spin, gain métrologique, distance de Hellinger

ABSTRACT

This thesis manuscript presents experiments realized with ultracold atomic gases of dysprosium. This element has specific properties such as a large spin J=8 and tunable light-spin couplings originating from significant tensor light-shift contributions close to resonance. An overview of the experimental setup is given, from magneto-optical trapping to evaporative cooling. In particular we present the role of the tensor light-shift in the in-trap Doppler cooling process. Details on the use of spatial modulation to tune the shape of an optical dipole trap are also given.

In the second part we describe the preparation of squeezed and 'oversqueezed' spin states as well as Schrödinger cat states using light-induced spin couplings. The magnetic sensitivity of these states is characterized using Ramsey spectroscopy. The Husimi function is reconstructed from population measurements along various directions, also allowing us to compute the purity of the prepared states.

While squeezed states show an increased metrological gain, oversqueezed states exhibit a strong Ramsey oscillations contrast reduction. The Hellinger distance is used to extend the notion of metrological gain and the sensitivity measured in this case saturates the Cramér-Rao bound. Finally a system of 16 indistinguishable interacting spins 1/2 is realized. In the third part we present the measurement of pairwise entanglement from photon absorption measurements, which was not realized experimentally.

Finally we present two projects where spatial degrees of freedom are added to the dynamics of internal levels. The first one consists in the realization of a system analogous to the Landau Hamiltonian of a charged particle in a magnetic field, with one spatial dimension and one synthetic dimension. The second project uses two spatial dimensions and exhibits an artificial magnetic field originating from position-dependent light-shifts.

KEYWORDS

Dysprosium, spin squeezing, oversqueezed states, metrological gain, Hellinger distance